ABSTRACT

Title of Document: TOWARDS UNDERSTANDING KEY PROCESSES AFFECTING HEAT AND SALINITY BALANCE IN THE GLOBAL OCEAN

Anthony Santorelli, Doctor of Philosophy, 2011

Directed By: Dr. James Carton, Department of Atmospheric and Oceanic Science

Ocean heat content is compared among nine analyses of global ocean temperature during 1960–2002. Two are independent of numerical modeling, and the rest rely on data assimilation, which utilizes an ocean general circulation model and observations to create an analysis. Most analyses show gradual warming of the global ocean with an ensemble trend of 0.77×10^8 J m^{-2} (10 yr)$^{-1}$ (=0.24 W m^{-2}) as the result of rapid warming in the early 1970s and again beginning around 1990. Three explanations for this decadal variability are proposed and tested: the effect of three major volcanic eruptions, the uncorrelated contribution of heat content variations in individual ocean basins, and the effect of time-dependent bias in the set of historical observations. It was found that the second hypothesis contributed significantly to heat content variability.

Uncertainties in latent and sensible heat fluxes are examined through a comparison between two flux estimates that differ in methodology and data used: the French Research Institute for Exploitation of the Sea (IFREMER) and the Woods Hole Oceanographic Institution's Objectively Analyzed air-sea Fluxes (WHOI OAFlux). The focus is on the Atlantic during 1996-2005. The variables that enter the bulk formulae for fluxes (wind speed, sea surface and air temperature, and specific humidity) are also analyzed. The estimates are also compared to three buoy experiments, using the method of Bourras (2006) to determine uncertainty compared to buoy data. Specific air humidity and air temperature contribute the most to biases of IFREMER fluxes. Modified flux estimates with the IFREMER approach using 10 m specific humidity and air temperature from Jackson et al. (2009) show improvement in test cases at *PIRATA* buoys.

Finally, results from an eddy-resolving numerical simulation are examined to quantify advective and diffusive contributions to the salt balance in the upper 100m of the subtropical oceans. Advection is important, especially horizontal, while time-mean diffusive processes and salt storage are several orders of magnitude less, but could still be important seasonally in areas of maximum surface salinity.

TOWARDS UNDERSTANDING KEY PROCESSES AFFECTING HEAT AND SALINITY BALANCE IN THE GLOBAL OCEAN

By

Anthony Santorelli

Dissertation submitted to the Faculty of the Graduate School of the

University of Maryland, College Park, in partial fulfillment

of the requirements for the degree of

Doctor of Philosophy

2011

Advisory Committee:

Professor James Carton, Chair

Professor Rachel T. Pinker

Professor Robert Hudson

Dr. Semyon Grodsky

Professor Karen Prestegaard, Dean's Representative

Dedication

To my parents, Angela and Tony, my girlfriend, Allison, and the rest of my family and friends for constant support and love through all of my academic endeavors. To Mrs. Maria Krauland, my elementary school science teacher, and Ms. Marlene Zucker, my elementary school principal, for inspiring me to pursue a career in atmospheric science.

Acknowledgements

I would like to thank my family and friends for their support and love as I have worked towards the completion of my dissertation. I also want to thank my committee, led by Professors James Carton and Rachel Pinker. Their support and feedback on my work have been instrumental to its completion. I am also grateful to the National Science Foundation, which has supported my graduate training. I also thank the numerous collaborators that I have had the privilege to work with: Drs. Abderrahim Bentamy, Frank Bryan, William Drennan, Benjamin Giese, Semyon Grodsky, Kristina Katsaros and Alberto Mestas-Nuñez.

Table of Contents

List of Tables

List of Figures

Chapter 1: Introduction

1.1 Heat and salinity

The global ocean covers 70% of the Earth's surface with depths of up to four kilometers. The physical properties of the ocean play a major role in the climate system. One of the major variables that dictate the sea state is temperature. The ocean's specific heat capacity, or the amount of heat energy that has to be transferred to the water to increase the temperature of one kilogram of the substance by one degree Celsius, is several times greater than that of land or the air. Thus, the ocean has a large thermal inertia, or ability to take in heat energy with a lagged response. In addition to temperature, another important state variable for the ocean is salinity, measured in units of practical salinity (psu, salt content of seawater based upon electrical conductivity of a sample relative to a reference standard of sea water) or in an absolute sense (mass of salt per mass of seawater). The ocean contains salts that have dissolved from rocks and sediments below its floor as well as from solid and gaseous materials that escaped from Earth's crusts through volcanic vents. The ocean maintains its saltiness through evaporation of water from the sea surface into the atmosphere, leaving behind the salt.

The average vertical profile of temperature and salinity in the ocean can be described in three zones from the sea surface to the ocean bottom: the mixed layer (upper 20-200m of the ocean), which contains uniform properties of temperature and salinity due to turbulent mixing, wind-driven currents and/or convection, the thermocline/halocline, or a zone of rapid change in temperature/salinity that can extend to

1km depth, and deep water, where both temperature and salinity exhibit very small changes with depth.

Heat is a form of energy, so it must be conserved in the ocean; it can be stored (ocean heat content), transported by advective (via motion by currents) or diffusive (from regions of higher to lower concentration) processes or transferred between the ocean and the atmosphere in either direction as flux. Ocean heat content is the vertical integral of ocean temperature to a prescribed depth, commonly ranging from 300-700m depth to account for the effects of the thermocline as well as the availability of observations at those depths. Ocean heat content is the dominant component of the Earth's heat balance, and, over the last 40 years, has been the main source of changes in global heat content (Rossby, 1959; Levitus et al., 2000, 2001). Averaged over the global ocean and over the Atlantic, Pacific and Indian oceans individually, annual ocean heat content in the upper 700 meters of the ocean (0/700m layer) has exhibited an upward trend over the last four decades (Levitus et al., 2009). This increase in ocean heat content has resulted in sea level rise due to thermosteric expansion of seawater; Antonov et al. (2005) found that, for 1955-2003, the thermal expansion of the 0/700m layer contributed approximately 0.33 mm/year to global sea level rise, which comprises almost 20% of the total sea level rise trend of 1.7mm/yr estimated using tide gauge measurements (Douglas, 2001; Peltier, 2001).

In addition to being stored, heat can also be transported within the ocean. The trade winds blow across the ocean, and wind stress along the sea surface in conjunction with the Coriolis and pressure gradient forces create ocean currents, which bring warm water from the Tropics poleward (i.e. the Gulf Stream in the Atlantic and the Kuroshio

Current in the Pacific), and bring cooler waters towards the Tropics (i.e. the California Current). This prevents the equatorial regions from getting hotter and the Poles from getting colder, maintaining global energy balance. Ocean currents account for around 40% of global energy transport annually in the Northern Hemisphere (the rest due to atmospheric circulation), with a peak of over 3 peta Watts yr^{-1} at 20°N and dominance over atmospheric transport in the 0°-30° latitudinal belt (Vonder Haar and Oort, 1973).

Heat can also be vertically exchanged as a net surface heat flux between the sea surface and atmosphere. There is a surplus of energy at the Equator and a deficit at the Poles, but, on a global scale, the amount of energy input into the ocean equals the amount of energy output into the atmosphere. Any imbalance of this reflects changes currently taking place in Earth's climate system. This variable serves as a forcing that drives climate models that predict future climate change. Net heat flux at the sea surface has radiative components, including incoming shortwave radiation from the sun and outgoing infrared radiation emitted from the sea surface, as well as turbulent components, including latent and sensible heat fluxes that occur due to vertical gradients between air and sea surface moisture and heat, respectively.

Figure 1.1a-b contains the annual-mean global maps of net shortwave (solar) and net longwave (thermal) radiation from the National Oceanography Centre Southampton Flux Dataset v2.0 (NOCS v2.0; Berry and Kent, 2009), which is based on volunteer ship data from version 2.4 of the International Comprehensive Ocean-Atmosphere Data Set (ICOADS; Woodruff et al., 1998; Worley et al., 2005). Note that a negative sign convention here indicates a flux from the ocean to the atmosphere (this is the opposite case for the study discussed in Chapter 3). Net solar heating is positive everywhere, but

3

the amount is dependent on the angle of incidence of the radiation as well as cloud cover. Naturally, the most solar radiation (> 200 W m^{-2}) occurs within 30° latitude of the Equator since there is a high amount of incident radiation. But, within ± 10° latitude of the Equator, clouds associated with the Intertropical Convergence Zone (ITCZ) reflect some of this radiation back to space. Net infrared radiation is negative everywhere, with the largest heat losses in areas of little or no cloud cover, such as near the subtropical latitudes (~30°).

Latent heat and sensible heat fluxes occur when the ocean surface and the overlying air differ in terms of moisture and temperature, respectively. Therefore, properties of the weather systems that propagate over the western boundary currents are coupled with the currents' properties. One example of this coupling is hurricane intensification, as ocean-to-atmosphere heat fluxes on the order of thousands of watts per meter squared are released when a hurricane moves over warm tropical waters, cooling the upper ocean but warming the atmosphere and producing enhanced convection (e.g. Shay et al., 2000; Cione and Uhlhorn, 2003). Figure 1.1c-d contains the annual-mean global maps of latent and sensible heat flux from the NOCS v2.0 dataset. Latent heat flux is on the order of 10^2 watts per meter squared (Wm^{-2}), while sensible heat flux is mainly on the order of 10^0-10^1 Wm^{-2}. The peak annual-mean ocean-to-atmosphere latent heat flux occurs in the Tropics (15°S-15°N) due to evaporation of water off the sea surface because of the trade winds, and in the Gulf Stream region (30°-45°N, 40°-75°W) due to wintertime cold-air outbreaks in North America that blow over the warm Gulf Stream waters; the humidity gradient is increased since the cold air is so dry. These outbreaks also explain the peak of sensible heat flux in the same region.
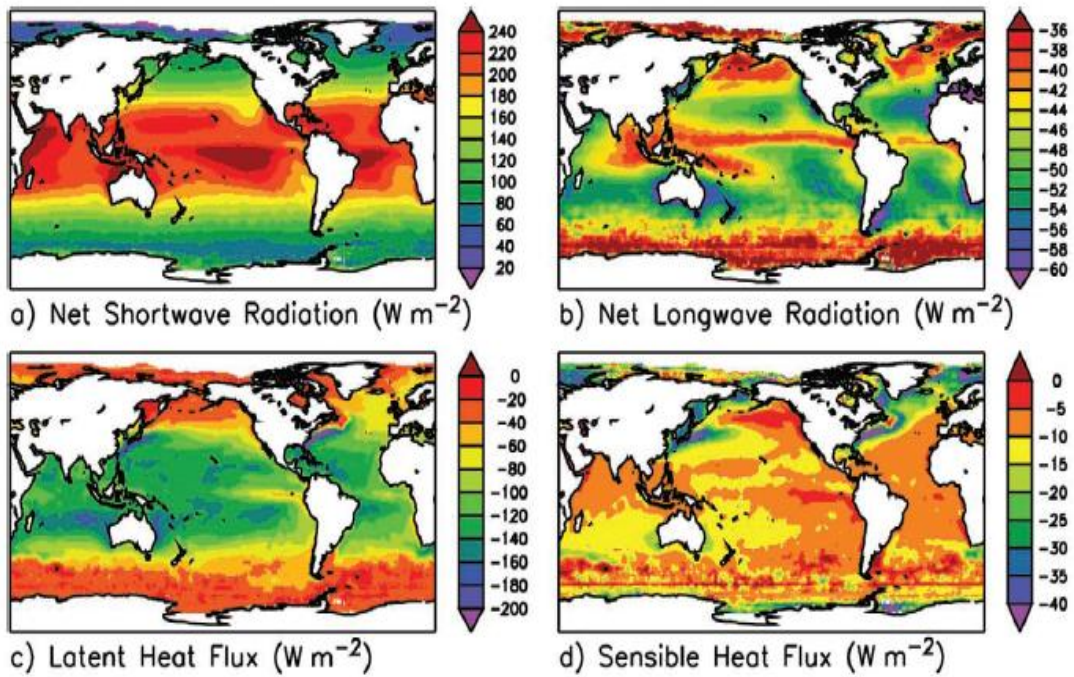
Figure 1.1.   Annual-mean a) net shortwave, b) net longwave, c) latent heat and d) sensible heat flux in the global ocean from the National Oceanography Centre Southampton Flux Dataset v2.0 (NOCS v2.0; Berry and Kent, 2009). A negative sign indicates a flux from the ocean to the atmosphere. Units W m^{-2}.

Latent heat flux can also be defined as the ocean-to-atmosphere flux of heat associated with evaporation of water at the sea surface. Along with other factors, such as river runoff and ground water flow, the difference between evaporation and precipitation (E-P) is vital in the assessment of the global water cycle, especially over the oceans; ~80% of global evaporation and precipitation occur over the ocean (Schmitt, 1995). This underscores the role the ocean has in the water cycle, given that it is by far the largest reservoir of water on our planet (volume of 1.4×10^9 km^3; Schmitt, 2008).

Ocean salinity is linked with E-P; higher amounts of salinity occur when evaporation exceeds precipitation, and vice versa. Figure 1.2a and b show annual-mean E-P (cm yr^{-1}) and surface salinity (psu), respectively (Schmitt, 2008). Evaporation is highest in the subtropical latitudes due to the subsidence associated with high pressure cells, resulting in dry air diverging from the centers of the highs, which feed the trade winds that evaporate water vapor from the sea surface and carry it towards the equator. In these regions, E>>P, with a maximum of 200 cm yr^{-1}. At the Equator, rising air at the ITCZ causes this water vapor to condense to form clouds and precipitation, which is greater than evaporation there and results in a negative E-P (<-100 cm yr^{-1}). Another area where P>E is poleward of the subtropical highs, where midlatitude storm tracks provide ample precipitation during all seasons.

Surface salinity in Figure 1.2b follows the patterns of E-P; higher surface salinity exists in subtropical latitudes due to high evaporation (maximum of ~38 psu in the Atlantic, ~36 psu in the Pacific), and lower salinity occurs in areas of higher precipitation, such as in the ITCZ and midlatitudes (~32-34 psu), as well as areas of runoff of freshwater into the ocean, such as near the Amazon River. The Atlantic has

higher salinities than those of the Pacific due to the Atlantic basin being narrower,

allowing for dry, continental air to have a stronger influence through higher evaporation

rates. Also, due to the arrangement of continents, moisture is transported readily to the

Pacific across the Central American isthmus, but not from the Indian Ocean to the

Atlantic.
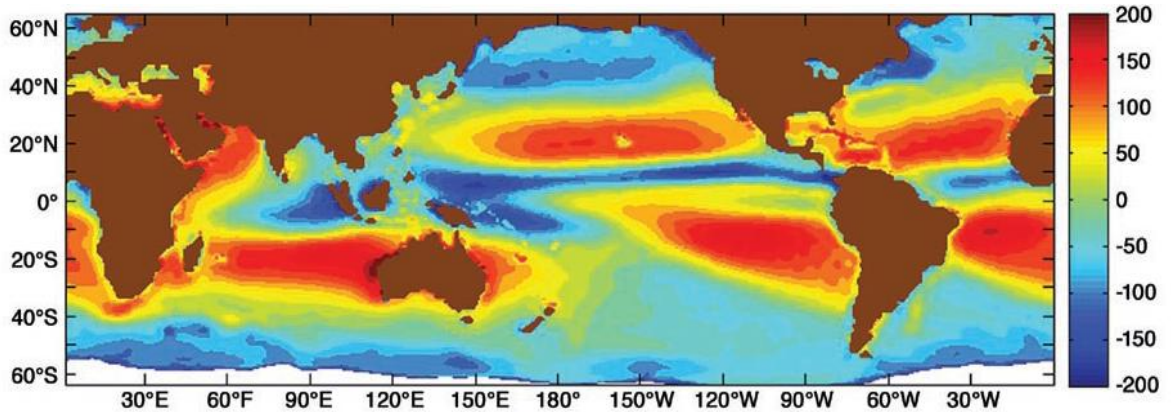
(a)
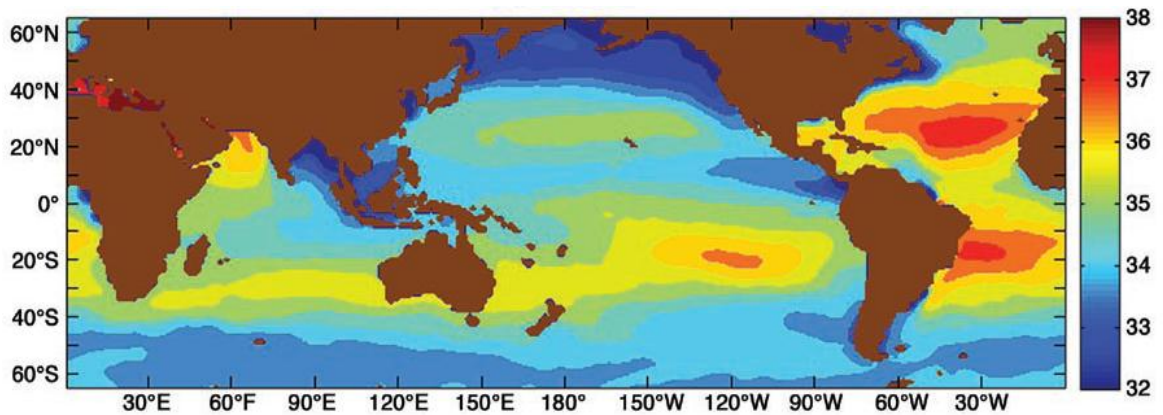
(b)

Figure 1.2.   (a) Annual-mean evaporation minus precipitation based on the evaporation climatology of Yu and Weller (2007) and satellite-based precipitation estimates from the Global Precipitation Climatology Program (GPCP, available at: http://precip.gsfc. nasa.gov). Units are cm yr^{-1}. (b) Average surface salinity of the world ocean, contoured from the World Ocean Database of the National Oceanographic Data Center

(http://www.nodc.noaa.gov/OCs/SELECT/dbsearch/ dbsearch.html). Units are psu. Figure taken from Schmitt (2008).

Salinity in the upper ocean is not only an important indicator of the intensity of water exchange between the ocean and atmosphere but also has an impact on the ocean's mass distribution, mixing rates and interior circulation (Schmitt, 2008). In regions of high evaporation, sea surface salinity as well as ocean surface density will increase. This will create dense water near the surface with less dense water below, resulting in increased deep convective mixing. The opposite occurs in areas of high precipitation, which provides an input of freshwater to the ocean, decreasing surface salinity, and, in turn, water density.

Furthermore, the following equation relates buoyancy flux (F_S), to surface freshwater forcing, or the product of freshwater flux and sea surface salinity $[S(E - P)]$:

$$\beta F_s = \frac{\beta S \rho_o (E-P)}{\rho_s (1-S)} \approx \beta S(E - P) \tag{1.1}$$

where ρ_o is the density of pure water and ρ_s is the density of seawater, and $\beta = \frac{1}{\rho} \frac{\partial \rho}{\partial s}$ is the haline contraction coefficient.

Salt and heat each greatly influence the climate system through oceanic circulation, both on small and large spatial scales. One example is eddies. At a given point, physical properties of the ocean fluctuate rapidly due to the motion of eddies, or areas of rotating fluid that are mesoscale in size, O($\sim 10^2$ km) in diameter, with lifetimes ranging from a month up to year. Eddies form due to the balance of horizontal pressure gradient arising from differences in water density and the Coriolis force, an apparent

force that arises due to the rotation of the Earth. Eddies pinch off of fast-moving currents, such and the Gulf Stream in the Atlantic Ocean, enclosing specific physical properties (i.e. temperature and salinity) and transferring them to other areas of the ocean. Eddies fall into two categories: cyclonic (or cold-core), exhibiting counter clockwise rotation in the Northern Hemisphere, cooler and lower in height in the middle by tens of centimeters, and anticyclonic (or warm-core), with clockwise rotation in the Northern Hemisphere, cooler and higher in height in the middle by tens of centimeters.

In addition to smaller-scale influence, surface heat and freshwater fluxes create density gradients that, along with winds, drive a large-scale ocean circulation known as the thermohaline circulation. Surface currents, such as the Gulf Stream, bring warm, salty waters poleward from the subtropics in the Northern Hemisphere. As they cool, the water becomes denser to the point where it sinks at high latitudes, creating the North Atlantic Deep Water mass. Most of this water upwells in the Southern Ocean. Analogous to what happens in the Northern Hemisphere, warm water travels from the Tropics in the Southern Hemisphere to Antarctica, becoming colder and denser as it moves poleward, then sinks, forming deep water known as Antarctic Bottom Water. This water mass is transported north to the Atlantic. The thermohaline circulation balances the distributions of warm, salty waters and cold, fresh waters, and, if changed, would cause abrupt and major changes to the climate of Earth.

1.2 Heat and salinity budget equations

The processes described above are represented quantitatively in the oceanic heat and salinity budget equations. Applying the methodology of Stevenson and Niiler (1983)

and Moisan and Niiler (1998), the budget for either heat or salt for an ocean layer of fixed

depth H can be expressed as

$$\int_{-H}^{0} \frac{\partial X}{\partial t} dz = -\int_{-H}^{0} \nabla \cdot \overrightarrow{UX} \, dz + Q_{\,o} - K \left. \frac{\partial X}{\partial z} \right|_{z=-H} + \int_{-H}^{0} (HDiff) dz \qquad (1.2)$$

$$\underbrace{}_{A} \quad \underbrace{}_{B} \underbrace{}_{C} \underbrace{}_{D} \quad \underbrace{}_{E}$$

where X can represent either temperature or salinity averaged over a given time interval,

$\overrightarrow{UX}$ is the three-dimensional transport of X $[(UX)\vec{\imath} + (VX)\vec{\jmath} + (WX)\vec{k}]$ where

U, V and W are zonal, meridional and vertical velocities, and K represents the vertical

turbulent exchange coefficient. The lettered terms in (1.2) indicate: (A) tendency, or the

rate of storage of heat/salt over time, (B) heat/salt advection expressed as transport

convergence (under the assumption that the ocean is an incompressible fluid and that

mass divergence is zero, or, mass is conserved; also note that the product of velocity and

temperature/salt is averaged over time in this term) integrated over a depth of -H, (C)

surface flux/forcing (see definitions for heat/salt flux in the previous section), (D) vertical

heat/salt diffusion at z=-H and (E) horizontal heat/salt diffusion. Regarding heat, Chapter

2 of the dissertation focuses on (A), and Chapter 3 focuses on components of (C). As for

salt, all terms in the budget are addressed in Chapter 4.

1.3 Motivation and objectives

Accuracy of oceanic heat and freshwater flux estimates must be high for correct

observation and modeling of climatic phenomena. Recent total heat flux estimates (i.e.

Berry and Kent, 2009) still do not achieve a realistic heat balance over the ocean, failing

11

to reach the necessary accuracy of 10 Wm^{-2} stated in previous works (Bretherton et al, 1982). As for freshwater fluxes, recent estimates of the annual cycle of evaporation and precipitation derived from satellites and reanalyses, or datasets that blend models and observations through data assimilation, neither satisfy the total moisture cycle, with imbalances between global precipitation and evaporation estimates of up to 5% (Schlosser and Houser, 2007), nor provide consistent analyses to verify climate model projections of hydrological change (Trenberth et al., 2007). Therefore, there is much work to be done to improve the accuracy of net surface heat and freshwater fluxes over the global ocean. Having a better understanding of key processes in the heat and salinity budgets will aid in achieving this goal.

The studies presented in this dissertation improve understanding of processes that govern heat and salinity balance in the ocean. In Chapter 2, nine analyses of global 0/700m temperature and heat content during the 43-year period of warming, 1960-2002, are compared in order to compare spatial and temporal patterns and trends as well as propose possible explanations for variations that are observed. In Chapter 3, uncertainties in estimates of turbulent heat fluxes are determined through a spatial and temporal comparison of two flux datasets, along with their respective parameters (sea surface and air temperature, wind speed, and specific humidity), that differ in data used as well as estimation methodology to each other as well as to ground truth from several field programs for the period of 1996-2005. Test cases where new satellite atmospheric specific humidity and air temperature data have been used to modify one of the turbulent flux computations are also performed. In Chapter 4, processes regulating the seasonal and intraseasonal contribution of processes to the salt balance in the upper 100m of the

subtropical oceans are examined using an eddy-resolving general circulation ocean-only model (version 2 of the Parallel Ocean Program model). Chapter 5 provides a summary of the studies as well as further conclusions and recommendations.

1.4 Statement of originality

Each of the following chapters contains a project that constitutes a paper suitable for journal publication. Chapter 2 contains work that was published in the *Journal of Climate* in 2008. Chapter 3 contains work that is in press in the *Journal of Geophysical Research-Oceans*. Chapter 4 contains work that will be submitted to *Journal of Physical Oceanography*.

Chapter 2: Global decadal upper ocean heat content as viewed in nine analyses

2.1 Abstract

This chapter examines nine analyses of global ocean 0-/700-m temperature and heat content during the 43-yr period of warming, 1960–2002. Among the analyses are two that are independent of any numerical model, six that rely on sequential data assimilation, including an ocean general circulation model, and one that uses four-dimensional variational data assimilation (4DVAR), including an ocean general circulation model and its adjoint. Most analyses show gradual warming of the global ocean with an ensemble trend of 0.77×10^8 J m^{-2} (10 yr)$^{-1}$ (=0.24 W m^{-2}) as the result of rapid warming in the early 1970s and again beginning around 1990. One proposed explanation for these variations is the effect of volcanic eruptions in 1963 and 1982. Examination of this hypothesis suggests that while there is an oceanic signal, it is insufficient to explain the observed heat content variations.

A second potential cause of decadal variations in global heat content is the uncorrelated contribution of heat content variations in individual ocean basins. The subtropical North Atlantic is warming at twice the global average, with accelerated warming in the 1960s and again beginning in the late 1980s and extending through the end of the record. The Barents Sea region of the Arctic Ocean and the Gulf of Mexico have also warmed, while the western subpolar North Atlantic has cooled. Heat content variability in the North Pacific differs significantly from the North Atlantic. There the spatial and temporal patterns are consistent with the decadal variability previously

identified through observational and modeling studies examining SST and surface winds. In the Southern Hemisphere large heat content anomalies are evident, and while there is substantial disagreement among analyses on average the band of latitudes at 30°–60°S contribute significantly to the global warming trend. Thus, the uncorrelated contributions of heat content variations in the individual basins are a major contributor to global heat content variations.

A third potential contributor to global heat content variations is the effect of time-dependent bias in the set of historical observations. This last possibility is examined by comparing the analyses to the unbiased salinity–temperature–depth dataset and finding a very substantial warm bias in all analyses in the 1970s relative to the latter decades. This warm bias may well explain the rapid increase in analysis heat content in the early 1970s, but not the more recent increase, which began in the early 1990s.

Finally, this chapter provides information about the similarities and differences between analyses that are independent of a model and those that use sequential assimilation and 4DVAR. The comparisons provide considerable encouragement for the use of the sequential analyses for climate research despite the presence of erroneous variability (also present in the no-model analyses) resulting from instrument bias. The strengths and weaknesses of each analysis need to be considered for a given application.

2.2 Introduction

This is an examination of the temperature in the upper 700 m of the global ocean during the 43-yr period of 1960–2002 as represented in nine gridded historical analyses.

Despite the limited and nonstationary character of historical temperature sampling and problems with instrument bias, a number of studies now show a gradual warming of the global oceans (e.g., Levitus et al., 2000, 2005; Carton et al., 2005; Ishii et al., 2006). The analyses used in these studies also show that the multidecadal trend is modified by rapid fluctuations in the warming rate with increases occurring in the early 1970s and again beginning in the 1990s (Fig. 2.1). These fluctuations have been interpreted as being either an artifact—the result of inadequacies of the data or analysis method (Gregory et al., 2004; AchutaRao et al., 2006; Gouretski and Koltermann, 2007)—or real, for example, the result of volcanic eruptions (Ramaswamy et al., 2001; Church et al., 2005; Delworth et al., 2005), variations in solar emissions (White et al., 2003), or natural variability of the climate system (Miller and Schneider, 2000; Lozier et al., 2008). Here decadal heat content variability is explored as it appears in a suite of nine historical analyses.

In individual ocean basins the character of decadal variability differs significantly from the global average. Observational and modeling studies in the North Pacific show decadal variability dominated by a cooling of subtropical SST in the central basin and in the Kuroshio–Oyashio Extension region, and warming in the east from the tropics to midlatitudes in the winter months beginning in 1976/77 (Mantua et al., 1997; Miller and Schneider, 2000). These changes are followed by a reduction of heat in the waters of the western subtropical gyre north of 30°N associated with changes in the wind patterns, advection, and surface heat flux (Miller et al., 1998; Miller and Schneider, 2000). Along the equator in the Pacific, Zhang et al. (1997) and Luo and Yamagata (2001) document a complex pattern of warm anomalies west of 160°E between 1965 and 1980 followed by a period of generally cool anomalies, while farther east warm anomalies are present during

the late 1970s and again through the 1990s. These and subsequent papers link the appearance of subtropical and tropical heat anomalies through subduction, or the transfer of fluid from the mixed layer into the stratified thermocline, and advective processes.

The North Atlantic, in contrast, shows rapid steady warming in the subtropics and midlatitudes and some cooling at subpolar latitudes, but with a basin-average rise of heat content according to Levitus et al. (2005) of 2×10^8 J m^{-2} (10 yr)$^{-1}$. This basin-average warming must reflect a net downward surface heat flux of 0.7 W m^{-2}. However, the decadal redistribution of heat within the basin has been ascribed to other processes. Dickson et al. (2000) examine cooling in the southern Labrador Sea and conclude that it results partly from decadal increases in convection and changes in freshwater input associated with winter storms. Studies farther east suggest that these changes in the Labrador Sea have acted to cool the broader subpolar gyre (Read and Gould, 1992). Lozier et al. (2008) relate both the subpolar cooling and subtropical warming to changes in surface transports associated with changes of the North Atlantic Oscillation and associated shifts in the winter storm tracks. Farther north observational studies have reported a gradual warming of the Eurasian portion of the Arctic Ocean. Grotefendt et al. (1998) show the warming trend in the Barents Sea through the mid-1990s to be the result of a combination of local warming and heat advection resulting from a poleward extension of warm Atlantic Water. This warming trend apparently reversed in the late 1990s (Gunn and Muench, 2001).

In the Southern Hemisphere decadal variations in heat content are undersampled. For example, of the 1.1 million temperature profiles collected in the 1960s, only 78 000

were collected south of 30°S [based on data described in Boyer et al. (2006)]. Alory et al. (2007) avoid this limitation by examining the much better-sampled SST dataset together with coupled model output and suggest that some of the most rapid increase of upper-ocean heat content during the past five decades has occurred in the South Indian Ocean. This suggestion is consistent with Willis et al. (2004) who detect substantial warming in the southern midlatitudes during recent years (1993–2002).

In addition to undersampling, two additional limitations of the historical observational dataset complicate the determination of decadal heat content variability. The first is the presence of changing observation bias resulting from the evolution of the observing system. The primary temperature dataset consists of 7.9 million vertical profiles. Prior to the early 1970s the majority were collected with a device called a mechanical bathythermograph (MBT), while between the 1970s and the early 2000s (the end of our period of interest) the majority were increasingly collected with the expendable bathythermograph (XBT; Boyer et al., 2006). The XBTs obtain their depth observations from the timing of the instrument fall rate. The equation converting fall time to depth that was used prior to the 1990s is known to underestimate depth by a few percent (Hanawa et al., 1995; Ingleby and Huddleston, 2007). However, there are ongoing debates regarding the efficacy of the fall-rate corrections in current use, thus leaving open the possibility that the increase in the rate of warming in the early 1970s noted in Fig. 2.1 may result from observation bias (AchutaRao et al., 2006).

A second limitation of the historical temperature dataset is its changing vertical sampling. MBTs measure temperature above 280 m, while XBTs generally extend to

either 400 or 700 m. Thus, of the 1.1 million profiles collected during the 1960s when MBTs were the primary instrument, only 100 000 extended to 500 m (Boyer et al., 2006). The impact of this shallow observation sampling on global heat content estimates has been considered recently by AchutaRao et al. (2006) and Gouretski and Koltermann (2007). Gouretski and Koltermann, for example, use spatial variability to estimate an uncertainty of at least 8×10^{22} J in global heat content in the upper 3000 m of the global ocean.

Another explanation for the presence of decadal variations in global heat content is that they are real and the result of volcanic aerosols injected into the stratosphere. Modeling studies suggest a reduction of global ocean heat content of $\sim 1 \times 10^{8}$ J m^{-2} for recent major eruptions beginning in the year following the eruption (Delworth et al., 2005; Church et al., 2005). However, in addition to their effect on global heat content it can be anticipated that distinct latitudinal responses to different eruptions. Mount Agung, which erupted in 1963, distributed much of its aerosols into the Southern Hemisphere (Hansen et al., 2005), and El Chichón, which erupted in 1982, distributed its stratospheric aerosols into the Northern Hemisphere, while Mount Pinatubo, which is located nearly as far north as El Chichón, distributed the aerosols from its 1991 eruption roughly symmetrically about the equator.

In this study, 0/700-m heat content computed from nine separate analyses of the historical temperature record is compared. The methodologies used in the nine analyses vary, but can roughly be divided into three approaches. The first is the "no model" analyses, which use temperature observations to update a first guess provided by

climatological monthly estimates of temperature. The second is the sequential data assimilation analyses, which march forward in time from a previous analysis using a numerical simulation of the evolving temperature and other variables produced by an ocean general circulation model. The simulation provides the first guess of the state of the ocean (temperature, salinity, etc.) at the next analysis time, while corrections are made to this first guess based on observations of variables such as temperature, salinity, or sea level. The third approach is four-dimensional variational data assimilation (4DVAR), which in this implementation uses the initial conditions and surface forcing as control variables to be modified in order to be consistent with the observations as well as a numerical representation of the equations of motion through iterative solution of a giant optimization problem [see Kalnay (2003) for a more detailed description of these three methodologies]. Comparison among these analyses allows us to address the question raised by Gregory et al. (2004) and AchutaRao et al. (2006) regarding the impact of the analysis methodology on the determination of decadal heat content in the global ocean.

2.3 Methods and data

Here the datasets and methodologies used in constructing the nine analyses are briefly reviewed (summarized in Table 2.1). The sources of the subsurface temperature and salinity datasets are one or another version of the National Oceanic and Atmospheric Administration's (NOAA's) *World Ocean Database* (*WOD*). The release in 1998, *WOD98*, contains a total of 5.3 million profiles, including 2.1 million MBTs (Boyer et al., 2006, see their Table 1.2). *WOD98*, together with recent updates from the Global Temperature–Salinity Profile Program (GTSPP; Wilson, 1998), forms the subsurface

20

temperature dataset used in the Global Ocean Data Assimilation System (GODAS). By the *WOD01* release (Conkright et al., 2002), which is used in Centre Européen de Recherche et de Formation Avancée en Calcul Scientifique [CERFACS; i.e., the European Centre for Research and Advanced Training in Scientific Computation; see Davey (2005)], Istituto Nazionale di Geofisica e Vulcanologia (INGV; see Davey, 2005), Ishii et al.'s (2006) analysis (hereafter ISHII), Levitus et al.'s (2005) analysis (hereafter LEVITUS), and the U.K. Forecasting Ocean Assimilation Model (U.K. FOAM; see Bell, 2000; Bell et al., 2004), the number of profile observations had grown by one-third to 7.0 million, with the number of MBTs increasing by 14%. Most of these analyses have also included recent data from GTSPP. The most recent release, *WOD05*, used in the Simple Ocean Data Assimilation (SODA; Carton and Giese, 2008), has seen an additional 16% increase to 7.9 million profiles, while the number of MBTs increases by an additional few percent along with improvements in quality control.

As mentioned in Section 2.2, XBT data are known to contain a warm bias resulting from inaccurate modeling of the instrument fall rate. ISHII, Geophysical Fluid Dynamics Laboratory (GFDL; Sun et al., 2007), GODAS (Behringer, 2005), INGV, LEVITUS, SODA, and U.K. FOAM all include a correction to this fall-rate equation provided by Hanawa et al. (1995). Three analyses—CERFACS, INGV, and U.K. FOAM—are part of the Enhanced Ocean Data Assimilation and Climate Prediction (ENACT) program (Davey, 2005) and use a common dataset that includes some additional bias corrections (Thadathil et al., 2002). For XBT profiles collected after 1996 there is some confusion in the observational record regarding which XBTs have had a fall-rate correction applied and which have not (see Levitus et al., 2005 for a discussion).

Analyses, such as GFDL, that show rapid warming after 1996 may possibly be suffering from a lack of universal fall-rate correction during this recent period (A. Rosati, 2007, personal communication).

In addition to the profile data two remotely sensed datasets enter many of the analyses. The first is satellite altimeter sea level, which is available continuously since 1991 from a succession of satellites. CERFACS, Global Estimation of Circulation and Climate Experiment (GECCO; Köhl and Stammer, 2008), GODAS, INGV, and U.K. FOAM all include these data. The second is satellite SST, which is available nearly continuously since 1981. For CERFACS, GECCO, GFDL, GODAS, and INGV these data enter indirectly through the use of a gridded SST product. SODA assimilates the nighttime SST observations directly. In addition to these datasets the analyses based on sequential data assimilation and 4DVAR use surface meteorological forcing provided by the 40-yr European Centre for Medium-Range Weather Forecasts (ECMWF) Re-Analysis (ERA-40; Uppala et al., 2005), the National Centers for Environmental Prediction–National Center for Atmospheric Research (NCEP–NCAR) Global Reanalysis 1 (NCEP-1) or NCEP/Department of Energy (DOE) Global Reanalysis 2 (NCEP-2; see Kalnay et al., 1996; Kanamitsu et al., 2002), or the Met Office operational product. Each meteorological product contains biases that must be considered when interpreting the analyses (e.g., Hines et al., 2000).

Next, the methodologies used to construct the analyses are described. The two no-model analyses, ISHII and LEVITUS, begin with a first guess of the climatological monthly upper-ocean temperature based on climatologies produced by the

NOAA/National Oceanographic Data Center (see Levitus et al., 2005; Ishii et al., 2006). For each analysis the differences between the observations and the first guess are mapped onto the analysis levels. LEVITUS uses the technique of Cressman (1959) and Barnes (1964) with a homogeneous decorrelation scale of 555 km to objectively map the differences between the temperature observations and the climatology onto a uniform grid. ISHII uses an alternative three-dimensional variational data assimilation (3DVAR) scheme to carry out this objective mapping with a somewhat smaller decorrelation scale in midlatitudes (300 km) that elongates in the zonal direction by a factor of 3 at equatorial latitudes.

The following six analyses are examined: CERFACS, GFDL, GODAS, INGV, SODA, and U.K. FOAM, which use sequential data assimilation. In sequential data assimilation an ocean general circulation model provides a first guess, while a version of optimal interpolation or 3DVAR is used to provide corrections to that first guess based on a set of empirically determined error covariances (see Kalnay, 2003).

The three ENACT assimilation analyses are CERFACS, INGV, and U.K. FOAM. CERFACS and INGV use an ocean model based on Océan Parallélisé (OPA) version 8.2 (Madec et al., 1998) numerics with $2° \times 2°$ horizontal resolution in the midlatitudes, decreasing to $2° \times 0.5°$ in the deep tropics and 3DVAR assimilation. ERA-40 surface winds and climatological fluxes are used by both. CERFACS uses an assimilation algorithm based on 3DVAR, while INGV uses the mathematically similar optimal interpolation (Davey, 2005). U.K. FOAM uses a different ocean model evolved from Cox (1984), with $1° \times 1° \times 33$ level resolution and 16 levels in the upper 700 m. Surface

forcing is provided by the Met Office numerical weather prediction winds and fluxes, along with climatological river discharge. The data assimilation is the timely optimal interpolation scheme of Bell (2000). In addition to the ENACT subsurface data, the analysis assimilates satellite altimetry using a modified version of the algorithm of Cooper and Haines (1996).

The GODAS analysis of Behringer (2005) uses an ocean model based on GFDL Modular Ocean Model (MOM) version 3 numerics with $1° \times 1°$ horizontal resolution in midlatitudes, decreasing to $1° \times 1/3°$ resolution in the deep tropics. The Arctic Ocean is not included in this grid. Surface forcing is provided by the NCEP-2 winds and fluxes. This analysis is the shortest considered here, spanning the period of 1979–2005. A related analysis produced by GFDL uses MOM version 4 numerics (Griffies et al., 2003) with a similar grid, but includes a complete Arctic Ocean. Winds, heat, and freshwater flux are provided by the NCEP–NCAR reanalysis (Kalnay et al., 1996). The assimilation is also a version of 3DVAR, but one that differs in detail from that used for GODAS.

The last of the sequential analyses is the Simple Ocean Data Assimilation, version 2.1, which uses a model based on the Parallel Ocean Program version 2.1 numerics with global average $0.25° \times 0.25°$ resolution ($0.25° \times 0.4°$ resolution in the tropics) and a complete Arctic Ocean. This analysis is driven by ERA-40 winds through 2001, with an extension beyond 2001 using satellite scatterometer winds.

Finally, the GECCO 4DVAR analysis is based on the forward and adjoint versions of the Massachusetts Institute of Technology (MIT) ocean circulation model (Marshall et al., 1997) with $2° \times 2°$ horizontal resolution, with initial flux estimates

24

provided by the NCEP–NCAR reanalysis. Climatological temperature and salinity were among the constraints. Among the control variables are the initial conditions and atmospheric fluxes (Stammer et al., 2004).

Each analysis output is reduced to monthly averaged temperature (except LEVITUS, which is only available as an annual average) for whatever portion of our period of interest (1960–2002) is covered by the analysis (see Table 2.1). Heat content is then computed by integrating the temperature vertically 0/700 m using linear interpolation, while anomalies are computed relative to the 25-yr period of 1966–95. For the GODAS analysis, which does not span the full base period, anomalies are computed relative to the 1979–95 average.

To explore the potential contribution of volcanic aerosols to decadal variability of heat content the difference in analysis heat content for 4-yr periods after and before the three major eruptions in 1963, 1982, and 1991 is compared. Because there is a limited number of eruptions to examine one concern is that the apparent response of the ocean will be affected by unrelated climate variability, particularly ENSO. In this comparison the impact of ENSO is mitigated by first carrying out a regression of the heat content analyses against the Southern Oscillation index. The part of the heat content variability that is correlated with this index at zero time lag is removed prior to computing the 4-yr differences. The impact of a linear trend in heat content is also removed prior to computing the 4-yr differences.

To aid in identification of heat content changes directly resulting from volcanic aerosols the 4-yr differences computed from the analyses are compared to similar

difference calculations performed on output from GFDL's Climate Model version 2.1(CM2.1) global coupled model (Delworth et al., 2005). To filter out the effects of random weather and climate variations from these coupled model differences the availability of multiple simulations allows for an examination of an average of five ensemble members.

Finally, as discussed in Section 2.2, there is serious concern that components of the observing system are biased and that bias in the observing system may lead to time-dependent bias within the analyses. To identify such bias within the analyses the analyses are compared to what is believed to be an unbiased dataset, the *WOD05* historical salinity–temperature–depth and conductivity–temperature–depth (CTD) dataset for the following three decades: 1970–99. This dataset contains 38,000 profiles in the North Atlantic and North Pacific. For each profile vertical integration is used to produce an estimate of heat content and then linearly interpolate the monthly heat content estimates from the analyses to the same geographic location to produce a set of analysis-minus-CTD observation differences. These differences are then composited into 10-yr averages. The interpretation of these statistics is discussed by Hollingsworth and Lonnberg (1989). No attempt is made to compute analysis-minus-CTD observation differences for LEVITUS because this analysis is only available as an annual average.

2.4 Results

In most analyses global average heat content has two periods of rapid growth—in the late-1960s through early 1970s and again beginning in the early 1990s, separated by quiescent or cooling periods in the early to middle 1960s and in the 1980s (Fig. 2.1). The

scatter among the individual analyses generally lies within $\pm 1 \times 10^8$ J m^{-2}. Because of the general similarity of the no-model and sequential analyses, an ensemble average is defined based on these eight analyses. The amplitude of the decadal anomalies is $1-2 \times 10^8$ J m^{-2} (a 1×10^8 J m^{-2} change in 5 yr implies a net heating of 0.63 W m^{-2}), while the multidecadal trend of the ensemble is 0.76×10^8 J m^{-2} (10 yr)$^{-1}$ or 0.24 W m^{-2}.

Note that caution must be taken in interpreting this trend since the uncertainty of ocean-atmosphere surface heat flux (on the order of tens of W m^{-2}) far exceeds this quantity. Also note that there can be significant errors that arise due to issues with reanalyses due to biases in either the observations, the models used or the forcing applied to the model. But, it is evident that most reanalyses exhibit the same direction in the trend as well as in decadal variability and agree not only with each other but with the two non-model analyses. The major exception is the GECCO 4DVAR analysis, which cools until the mid-1970s and then begins a multidecadal period of warming. Two of the analyses—U.K. FOAM and GFDL—show significant additional warming beginning in the mid-1990s.

The spatial distribution of the linear trend for each analysis is presented in Fig. 2.2. Several regions show rapid warming. These include the western half of the subtropical and midlatitude North Atlantic, the South Atlantic, the subtropical North and South Pacific, and the northern parts of the Indian Ocean, as well as the Indian Ocean south of 30°S. Interestingly, there is a cooling trend in the Kuroshio–Oyashio Extension region of the North Pacific in most analyses except GECCO. Several analyses have cooling trends in the central and western equatorial Pacific, including INGV, ISHII,

LEVITUS, and notably GECCO. Weak cooling is also evident in most analyses just south of the equator in the Indian Ocean.

Next, the impact of the three major eruptions are considered: Mount Agung in 1963, El Chichón in 1982, and Mount Pinatubo in 1991. For each eruption the 4-yr heat content average following the eruption minus the 4-yr average up to and including the year of the eruption (Fig. 2.3), reveals a complex and varied pattern of change. Only five of the nine analyses extend back to 1960, prior to Mount Agung. Of these, the no-model analyses show only weak anomalies in its aftermath, while the data assimilation analyses show cooling north and south of the equator in the equatorial Pacific, with a suggestion of warming in the North Pacific and North Atlantic. The coupled model results interestingly show an antisymmetric response in the tropical Pacific with cooling north of the equator and warming south of the equator.

For El Chichón all nine analyses are available (Fig. 2.3) and the analyses as well as the coupled model are consistent in showing cooling on and/or just south of the equator in the tropical Pacific. Some cooling is also evident in many of the analyses in the southwestern tropical Indian Ocean. In the North Pacific many of the analyses show cooling in the Kuroshio–Oyashio Extension region. This cooling, which is not evident in the coupled model, may be an aspect of North Pacific climate variability unrelated to aerosol forcing. For Mount Pinatubo most analyses show general warming except in the western equatorial Pacific (Fig. 2.3).

Next, the decade-by-decade heat content anomalies in each analysis are considered (Fig. 2.4). To develop an understanding of the potential biases within the

analyses corresponding decadal estimates of heat-content-analysis-minus-CTD observation differences are also examined (Fig. 2.5). These analysis-minus-CTD observation comparisons are limited to the Northern Hemisphere and to the three decades 1970–99 in order to ensure sufficient data coverage.

Examination of the heat content anomalies in Fig. 2.4 shows the North Atlantic to be warming rapidly in nearly all analyses similar to the behavior described in Levitus et al. (2000). In the 1960s most analyses are anomalously cool in the western tropics, subtropics, and midlatitudes by up to 6×10^8 J m^{-2} with anomalously warm temperatures in the eastern subtropics and subpolar regions. The main exception is GECCO, which is warm in the central and eastern subtropics, and along with INGV is anomalously cool throughout the tropics. In the 1970s and 1980s heat content anomalies are generally weak again, with the exception of GECCO, where the warm subtropics and cool midlatitude and tropical anomalies persist throughout the 1970s. However, the GECCO anomalies are superimposed on a mean state that is warmer than the CTD observations throughout much of the Atlantic so the analysis-minus-CTD observation differences are positive (Fig. 2.5).

By the 1990s the western subtropics to midlatitudes in most analyses have warmed (Fig. 2.4). In the tropics INGV has rather a strong warm anomaly (warmer than the CTDs, see Fig. 2.5), while GODAS has cool anomalies in the west. At subpolar latitudes many analyses show cool anomalies in the 1990s concentrated in the west and extending into the Labrador Sea, consistent with independent observations, as discussed in Section 2.2. Interestingly, half of the analyses show the cooling in the 1990s to be

concentrated not at the latitude of the Labrador Sea, but farther south off Newfoundland. In most analyses the warming in the 1990s is concentrated in the upper 350 m, as noted by Levitus et al. (2000). Interestingly three analyses, CERFACS, INGV, and U.K. FOAM, also show significant warming extending to thermocline depths of 700 m, while two analyses, GECCO and GFDL, show the warming to be concentrated in the upper 200 m (Fig. 2.6).

All seven analyses that include a full Arctic Ocean (see Table 2.1) have cool heat content anomalies in the Eurasian sector in the 1960s and warm anomalies in the 1990s (not shown). The strongest warm anomalies, exceeding 6×10^8 J m^{-2}, appear in GFDL and SODA. In other analyses the warming in the 1990s is primarily confined to the Greenland and Barents Seas where the warming has been previously documented, as discussed in Section 2.2.

The Caribbean Sea and Gulf of Mexico, which is coarsely resolved in most analyses, is cool in half the analyses in the 1960s (CERFACS, INGV, ISHII, and LEVITUS) and warm in the rest (Fig. 2.4). By the 1970s most analyses show cool anomalies, although examination of the analysis-minus-CTD observation differences show that these cool anomalies are still too warm compared to the observations (Fig. 2.5). By the 1990s the cool anomalies have been replaced by warm anomalies in all analyses except GECCO. However, in all analyses the warm anomalies in the Gulf of Mexico in the 1990s are too warm relative to the CTDs.

Next considered is the decadal heat content of the other well-sampled basin, the North Pacific (Fig. 2.5). While the North Atlantic is dominated by long-term warming,

the North Pacific shows a modest warming trend, but with strong decadal heat content variability. Many analyses (with the exceptions being GFDL and GECCO) have cool heat content anomalies in the 1960s, particularly in the northern tropics, while all show neutral or warm heat content anomalies along the equator. Basin-average heat content in most analyses increases to a peak in 1980, and then cools in the Kuroshio–Oyashio Extension region until the late 1980s. In the 1990s the midlatitude ocean begins to warm again in most analyses while the western tropics cool and the eastern tropics warm.

Two analyses, GECCO and GFDL, behave somewhat differently in the North Pacific. GECCO is warm in the 1960s with the heat concentrated in the tropics, cool in the 1970s, and finally warm in the late 1980s and 1990s in the midlatitudes. GFDL is also very warm in the 1960s in the tropics, but by 1970 it resembles the other analyses. INGV and the no-model analyses have weaker anomalies, but patterns similar to CERFACS, SODA, and U.K. FOAM. Examination of the analysis-minus-CTD observation differences shows all analyses to be biased warm throughout the 1970s–90s, with the most pronounced bias evident in GECCO (Fig. 2.5).

The changes in the North Pacific heat content bear resemblance to the observed decadal variability of winter SST in the North Pacific (Pacific Decadal Oscillation; Mantua et al.,1997). Until the late 1970s SSTs were cool in the northwest basin and warm in the eastern tropics and along the west coast of North America. In the late 1970s until 1999 this pattern of SST reversed. Examination of the leading empirical orthogonal eigenfunction of heat content anomalies (computed for 20°–60°N, analogous to the definition of the PDO index) shows positive values along the eastern side of the basin and

northwestern tropics in many of the analyses and negative values throughout the interior

subtropics in most analyses (Fig. 2.7), which are similar in structure to the PDO. The

explained variance of the leading mode ranges from a low of 7% for the highest-

resolution analysis (SODA) to 17% and 19% for U.K. FOAM and INGV. The principal

component time series of most analyses also show considerable similarity to the PDO

index (Fig. 2.7). The exception is GECCO for which neither the first nor second

empirical eigenfunction resemble the Pacific decadal oscillation pattern.

Next, the poorly sampled South Atlantic and South Pacific Ocean are considered.

The no-model analyses, LEVITUS and ISHII, have only weak 3×10^8 J m^{-2} warm

anomalies in the southwestern Pacific and Atlantic in the late 1960s and early 1970s, and

then begin to cool (Fig. 2.8). Many of the sequential analyses (CERFACS, INGV,

SODA, and U.K. FOAM) show patterns with similar spatial structures to the no-model

analyses, but with larger 3–6×10^8 J m^{-2} amplitudes and with some evidence of warming

in the southern midlatitude oceans by the 1990s. GECCO also shows anomalies that

resemble the no-model analyses, but with even larger amplitudes, in excess of 15×10^8 J

m^{-2}, and with some other differences such as the presence of warm anomalies in the

subtropical South Atlantic in the 1960s.

In the Indian Ocean the no-model analyses also show weak anomalies with cool

anomalies in the southern subtropical west and in the Arabian Sea in the 1960s and warm

anomalies south of 30°S in the 1990s (coinciding with the observed strong warming of

SSTs discussed in Section 2.2; see Fig. 2.9). The sequential analyses show much stronger

heat content anomalies, but with patterns generally resembling the no-model analyses.

The most pronounced differences among the sequential analyses occur south of 30°S where CERFACS, SODA, and U.K. FOAM show strong warming, while GFDL shows no anomalies and GODAS shows warm and cool anomalies. Along the equator most of the sequential analyses show weak equatorial cooling, but SODA shows a very pronounced equatorial cool anomaly in the eastern half of the basin in the 1990s as a result of intense upwelling along the eastern equator in 1994 and 1997 (Grodsky et al., 2001). GECCO, alternatively, shows dramatic basin-scale warming north of 30°S except in the Arabian Sea, and cooling between 30° and 60°S.

2.5 Summary

Examination of the nine analyses of ocean heat content shows that the global ocean 0/700 m has been warming at a rate of 0.76×10^8 J m^{-2} (10 yr)$^{-1}$ (=0.24 W m^{-2}) during 1960–2002, confirming the results of studies with individual analyses (e.g., Levitus et al., 2000, 2005; Carton et al., 2005; Ishii et al., 2006). Many uncertainties surround these individual estimates because of inadequacies in the historical observation network and the instruments, the techniques used to construct gridded analyses, and even the applicability of estimating a linear trend from the global data. By comparing the analyses to each other and to the historical observation set this paper the intention was to shed light on these uncertainties and the presence of natural climate variability and to improve understanding of the utility of the analyses for decadal climate research.

The analyses considered include two no-model analyses—ISHII and LEVITUS—in which a first guess of the climatological monthly cycle of upper-ocean temperature is updated based on historical ocean profile observations. Six analyses based on sequential

data assimilation are considered—CERFACS, GFDL, GODAS, INGV, SODA, and U.K. FOAM—in which an ocean general circulation model provides a first guess that is updated based on the ocean observations. Finally, one analysis based on a 4DVAR algorithm is considered—GECCO—in which a forward model and its adjoint are used to adjust initial conditions and surface forcing based on misfits to the ocean observations.

The analyses differ in choice of initial conditions, surface forcing, model physics, and resolution, and to a lesser extent which observations are used. Also, the analyses are affected by the different purposes for which they were created. Two of the analyses, GFDL and GODAS, were created to provide initial conditions for seasonal forecasts and thus have been designed to provide their best results in the upper levels of the tropics. Both of these have spurious anomalies in the first few years of the analysis period, and GODAS has very large anomalies in the Southern Ocean. Many of the analyses have $1° \times 1°$ horizontal resolution and thus do not resolve the ocean mesoscale. However, several have enhanced tropical resolution to resolve the intense tropical current systems and one, SODA, has global eddy-permitting resolution in order to resolve features of the midlatitude and subpolar circulation. Seven of nine analyses (CERFACS, SODA, GFDL, INGV, ISHII, LEVITUS, and U.K. FOAM) include the Arctic Ocean. Five of nine analyses (CERFACS, GECCO, GODAS, INGV, and U.K. FOAM) assimilate satellite altimeter sea level observations as well as the historical profile dataset. Of these, GODAS and GECCO show large changes in the late 1980s to early 1990s, which may be related to the introduction of altimeter sea level data.

Despite these differences, the analyses do have many common features. Most analyses show the following two periods of rapid heating: first in the early 1970s and again beginning in the late 1980s. One possible explanation for these periods of rapid warming is that they occur following cool periods associated with the major tropical volcanic eruptions of Mount Agung in 1963 and El Chichón in 1982 (Ramaswamy et al., 2001; Church et al., 2005). Indeed, coupled modeling results reported in Delworth et al. (2005) show reductions in ocean heat content of $1-2 \times 10^8$ J m^{-2} lasting for a few years resulting from the impact of volcanic aerosols (less in response to Mount Agung). The spatial pattern of the heat content anomalies produced by their coupled model does indicate the possibility of a cooling of ocean heat content in the equatorial Pacific. However, the aerosol effect is unlikely to explain the nearly decadal pattern of heat content anomalies that appear in the global time series. It is noted, for example, that the analysis heat content estimates do not seem to reflect an impact from the Mount Pinatubo eruption of 1991.

A second possible explanation for these periods of rapid warming is that it is the result of combining the "natural" variability of the climate system operating fairly independently in different basins. Basin-average heat content time series for the North Atlantic (Fig. 2.10a), for example, shows a rapid, fairly constant increase at a rate of 1.7 $\times 10^8$ J m^{-2} (10 yr)$^{-1}$ [Levitus et al. (2005) finds a similar nearly linear trend of 2.2×10^8 J m^{-2} (10 yr)$^{-1}$ for the full Atlantic basin]. The horizontal and vertical structure of the anomalies are similar for the no-model and sequential analyses, with most of the heating occurring in the subtropics and midlatitudes and weak cooling in and south of the Labrador Sea. Much of this additional heat is confined to the upper 400 m. Two regions

of particular interest, the Eurasian sector of the Arctic Ocean and the Gulf of Mexico, likewise show significant warming in the 1990s. In the North Pacific most of the basin-average time series (Fig. 2.10b) show strong decadal variability, that is, warm in the mid-1970s to early 1980s and again beginning in the early 1990s. This North Pacific variability is very similar to that examined in previous studies, such as Mantua et al. (1997) and Zhang et al. (1997).

Heat content anomalies in the Southern Hemisphere in many of the analyses are large and thus are very important contributors to the global average, but are not well documented previously. Although the analyses show many differences, they also show some common features. In contrast to their Northern Hemisphere counterparts, Southern Hemisphere anomalies extend zonally across ocean basins. The 1960s are characterized by warm anomalies in the 0°–10°S and 30°–40°S latitude bands, with cool anomalies in between. By the 1990s much of the Southern Hemisphere has warmed in most analyses, with the most pronounced warming occurring in the Atlantic and Indian sectors. Among the analyses the no-model analyses (ISHII and LEVITUS) and INGV show only weak anomalies. GECCO and GODAS have more vigorous anomalies, with GECCO showing strong warming and GODAS showing strong cooling in recent decades.

A third possible explanation for the periods of rapid global warming is that they are artificial, resulting from changes in geographic coverage and the introduction of an uncorrected warm bias resulting from the introduction of the XBTs in the 1970s. The warm bias, which varies by batch and type of XBT, would affect all analyses, but not the coupled models, which do not show such periods of rapid warming (Gregory et al., 2004;

Delworth et al., 2005). This explanation is explored by comparing the analyses to the unbiased CTD observation dataset during three decades of 1970–99 in the relatively well-sampled North Atlantic and North Pacific. This analysis-minus-CTD observation comparison, shown geographically in Fig. 2.5 and with time in Fig. 2.11, reveals a warm bias that is most pronounced in the 1970s and appears to diminish by the 1990s. The change in bias from the 1970s through the 1990s is more pronounced in the North Pacific and likely contributes to the warmth of the 1970s relative to the multidecadal trend, but does not explain the rapid rise in global heat content beginning in the 1990s and continuing to the present (see Fig. 2.11). These results confirm the results of Gouretski (2008, personal communication) and Wijffels et al. (2008), who directly compare XBT and CTD observations.

Analysis, reference	Time span	Data	Surface fluxes	Model, resolution	Analysis procedure
CERFACS, Davey (2005)	1962–2001	*WOD01*, GTSPP, altimeter sea level	ERA-40 winds, climatological fluxes	ORCA2 version OPA 2° × 2°–1/2° 16 levels	Sequential
GECCO, Köhl and Stammer (2008)	1950–99	MBTs, XBTs, hydrography, Argo profiles, near-surface drifters, Reynolds and Tropical Rainfall Measuring Mission Microwave Imager SST, altimeter sea level	NCEP–NCAR-1 reanalysis winds, fluxes	MIT GCM 1° × 1° 12 levels	4DVAR
GFDL, Sun et al. (2007)	1955–99	MBTs, XBTs, hydrography	NCEP–NCAR-1 reanalysis winds, fluxes	MOM 4 1° × 1°–1/3° 32 levels	Sequential
GODAS, Behringer (2005)	1979–2005	*WOD98*, GTSPP, moored temperature, Argo, altimeter sea level	NCEP NCEP-2 winds, fluxes	MOM 3 1° × 1°–1/3° 29 levels	Sequential
INGV, Bellucci et al. (2007)	1962–2001	*WOD01*, GTSPP, altimeter sea level	ERA-40 winds, climatological fluxes	OPA 1° × 1° 16 levels	Sequential
ISHII, Ishii et al. (2006)	1945–2005	*WOD01*, GTSPP	None	None 1° × 1° 16 levels	Objective analysis
LEVITUS, Levitus et al. (2005)	1955–2003	*WOD01*, GTSPP	None	None 1° × 1° 16 levels	Objective analysis
SODA, Carton and Giese (2008)	1958–2005	*WOD05*, GTSPP, in situ and Advanced Very High Resolution Radiometer SST	ERA-40 and Quick Scatterometer winds, Global Precipitation Climatology Project rain, bulk heat flux	POP 2.1 1/4° × 1/4° 21 levels	Sequential
U.K. FOAM, Bell (2000) and Bell et al. (2004)	1962–98	*WOD01*, GTSPP, altimeter sea level	Met Office NWP suite	GloSea 1° × 1° 16 levels	Sequential

Table 2.1.   Analyses considered in this study. Two no-model analyses are included (ISHII and LEVITUS). Six are based on sequential data assimilation filters and an ocean general circulation model (CERFACS, GFDL, GODAS, INGV, SODA, and U.K. FOAM). A ninth, GECCO, uses 4DVAR data assimilation smoother and both a forward and an adjoint ocean general circulation model. The vertical resolution given below only includes the number of levels between the surface and 700 m; U.K. FOAM has been shortened from 2004 to 1998 because of some problems at the end of the analysis period.
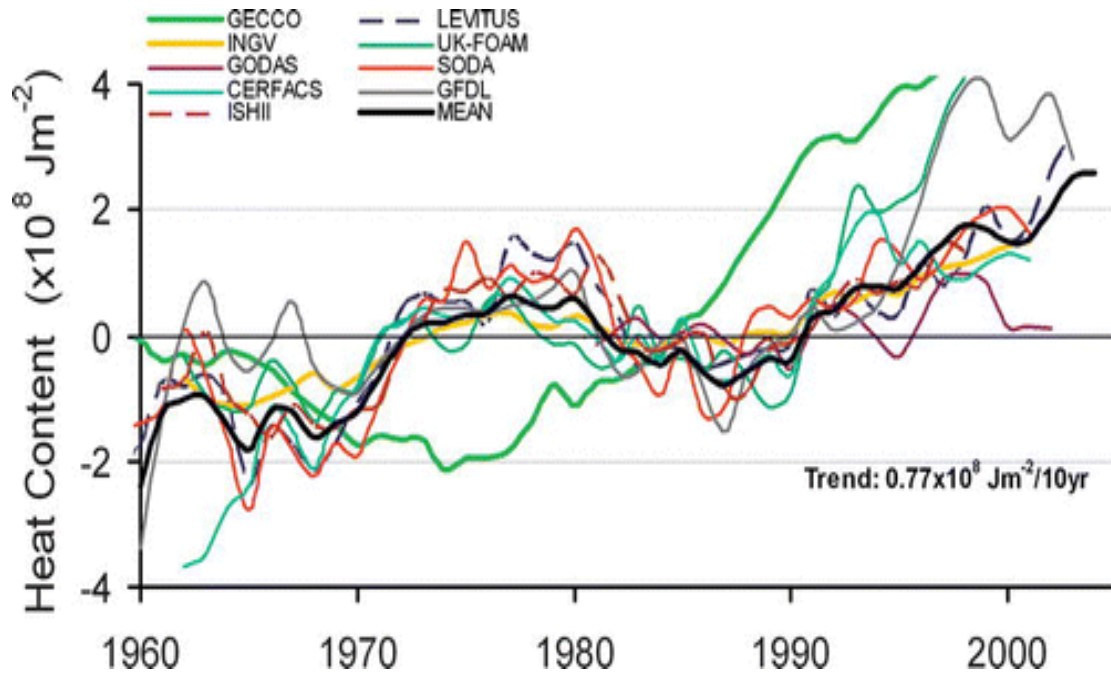
Figure 2.1.　Global average heat content anomalies from the individual 30-yr record means (1966–95), integrated at 0/700 m and temporally smoothed with a 1-yr running filter. Bold black curve shows the ensemble average of the nine no-model and sequential analyses. The linear trend of the ensemble average is 0.77×10^8 J m^{-2} (10 yr)$^{-1}$ or 0.24 W m^{-2}, while trends of individual analyses range from 0.68 to 0.98×10^8 J m^{-2} (10 yr)$^{-1}$ (0.21–0.31 W m^{-2}). Global integrated heat content can be obtained from the global average by multiplying by the surface area of the World Ocean, excluding shelves, with 3.4×10^{14} m^2.
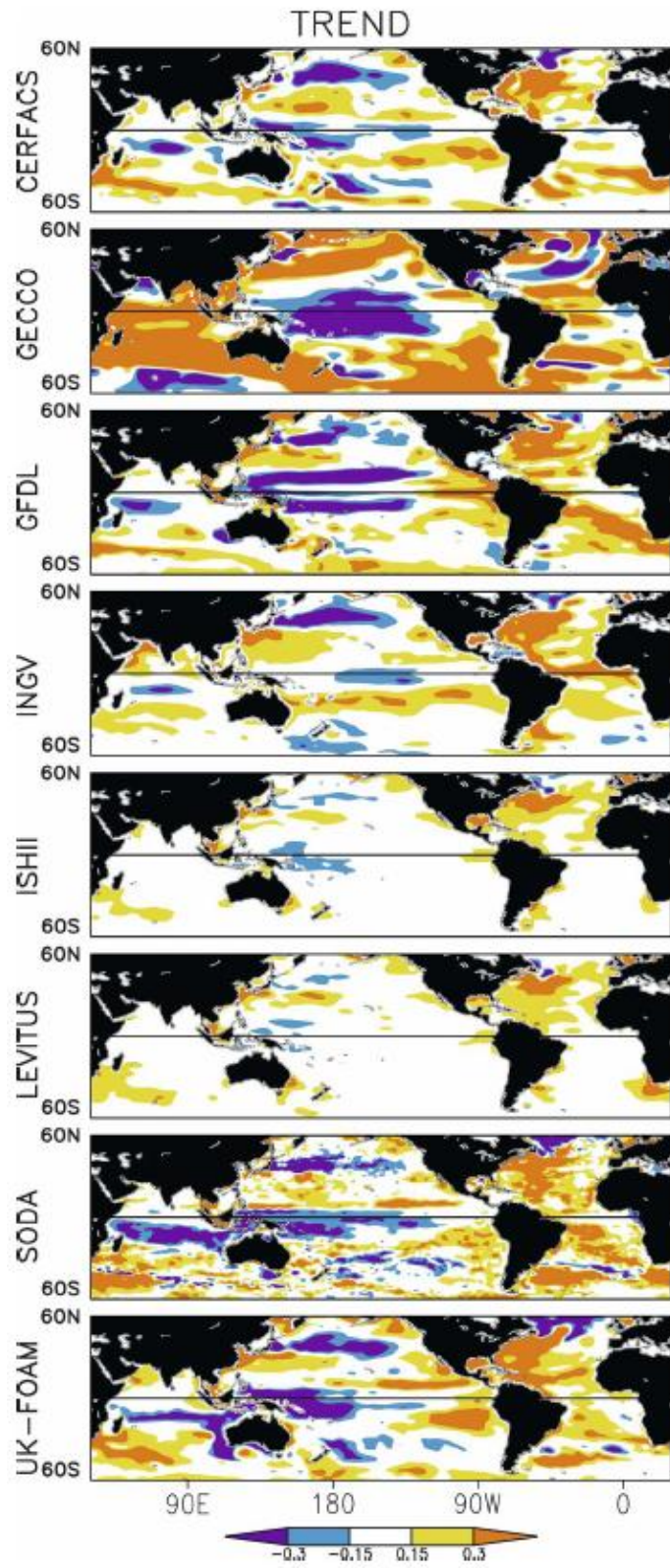
Figure 2.2. Multidecadal linear trend of 0-/700-m ocean heat content variability corresponding to Fig. 2.1. Values exceeding $\pm 0.15 \times 10^8$ J m^{-2} (10 yr)$^{-1}$ are shaded.
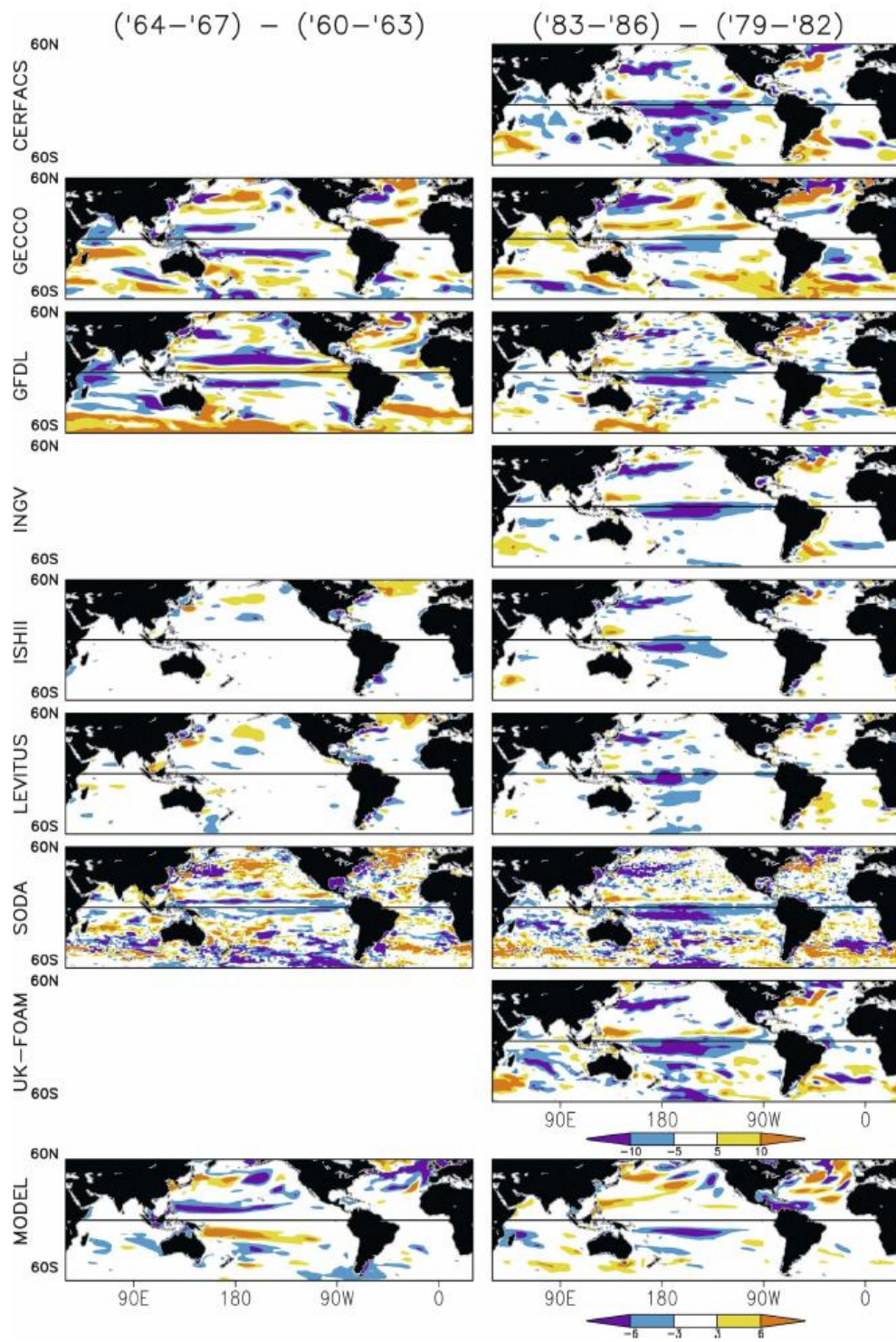
Figure 2.3.   Change in 4-yr average heat content spanning the eruptions of Mount

Agung (1963), El Chichón (1982), and Mount Pinatubo (1991). Prior to computing the

heat content change a regression analysis is used to remove the effects of ENSO and a

linear warming trend (see Fig. 2.2). Eight analyses extending back to at least 1962 are

shown in the upper panels. Changes exceeding $\pm 5 \times 10^8$ J m^{-2} are shaded. Lowest panels

show the change in heat content from a five-member ensemble of the GFDL coupled

simulation CM2.1 with complete aerosol forcing. Changes exceeding $\pm 3 \times 10^8$ J m^{-2} are

shaded.

('92–'95) – ('88–'91)
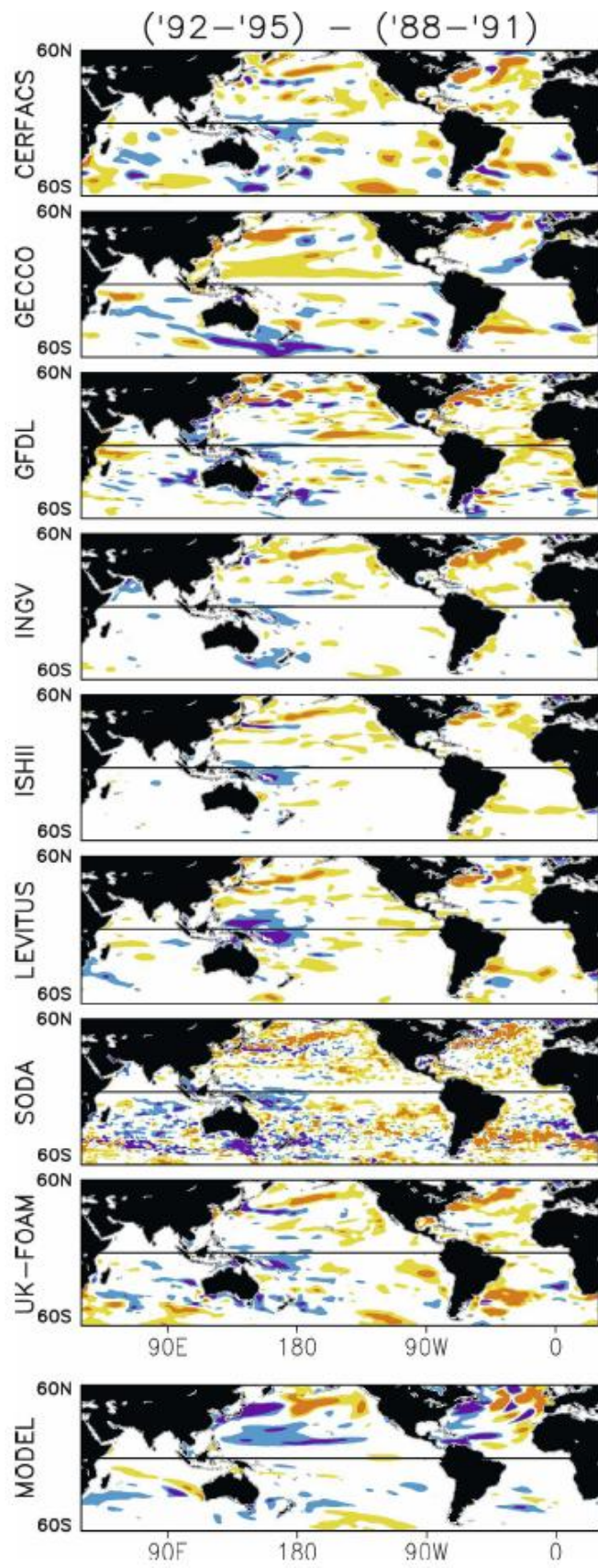
Figure 2.3 (continued).
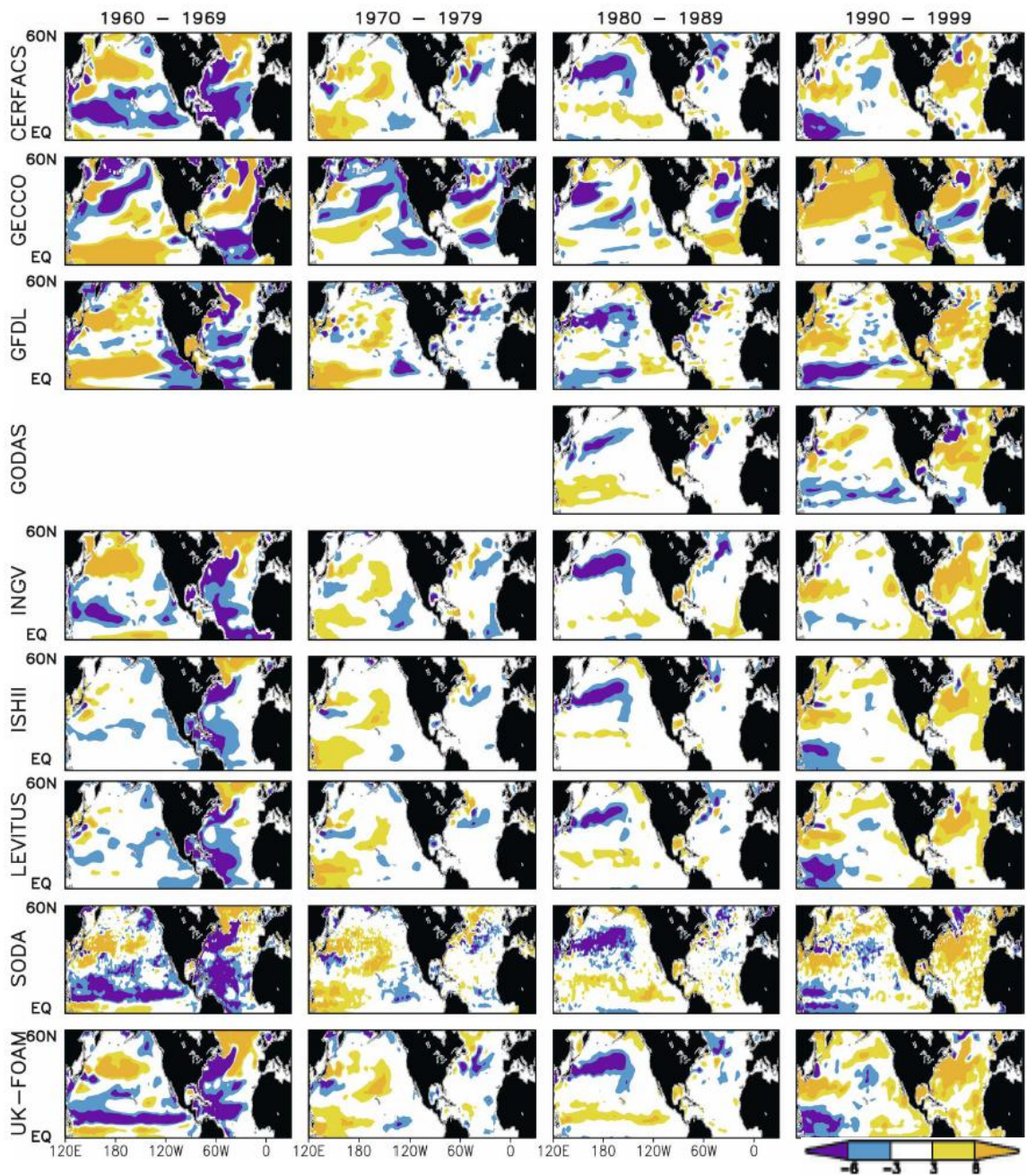
Figure 2.4.   North Pacific and Atlantic heat content anomalies relative to the 30-yr record means averaged by decade: 1960–69, 1970–79, 1980–89, and 1990–99. Anomalies exceeding $\pm 3 \times 10^8$ J m^{-2} are shaded.
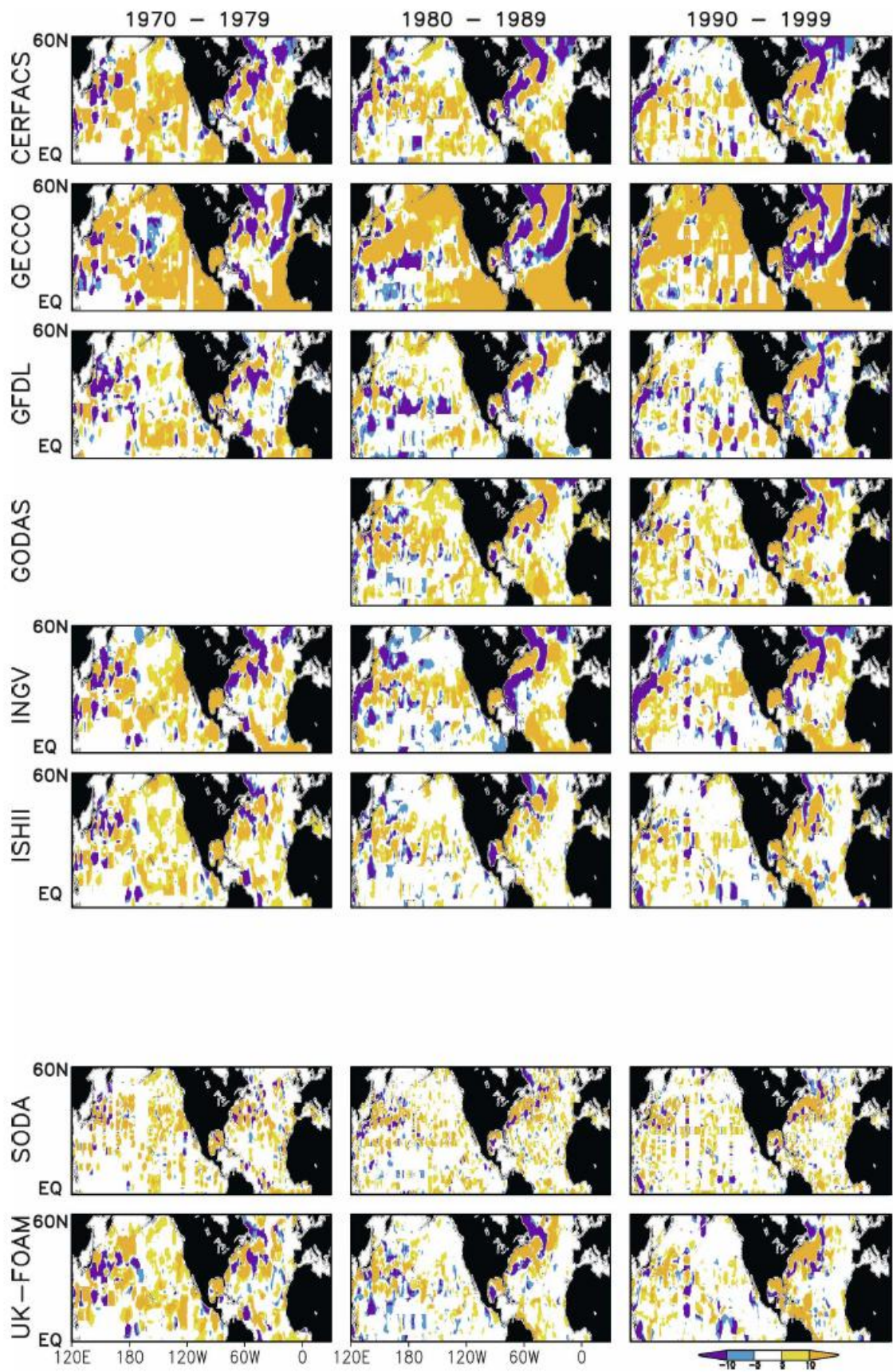
Figure 2.5. Heat-content-analysis-minus-CTD observation monthly differences averaged by decade corresponding to Fig. 3 for the last three decades: 1970–79, 1980–89, and 1990–99 (no climatology is removed from either dataset). Differences exceeding ±5 × 10^8 J m^{-2} are shaded. Differences for LEVITUS are not shown because this analysis is only available as an annual average.
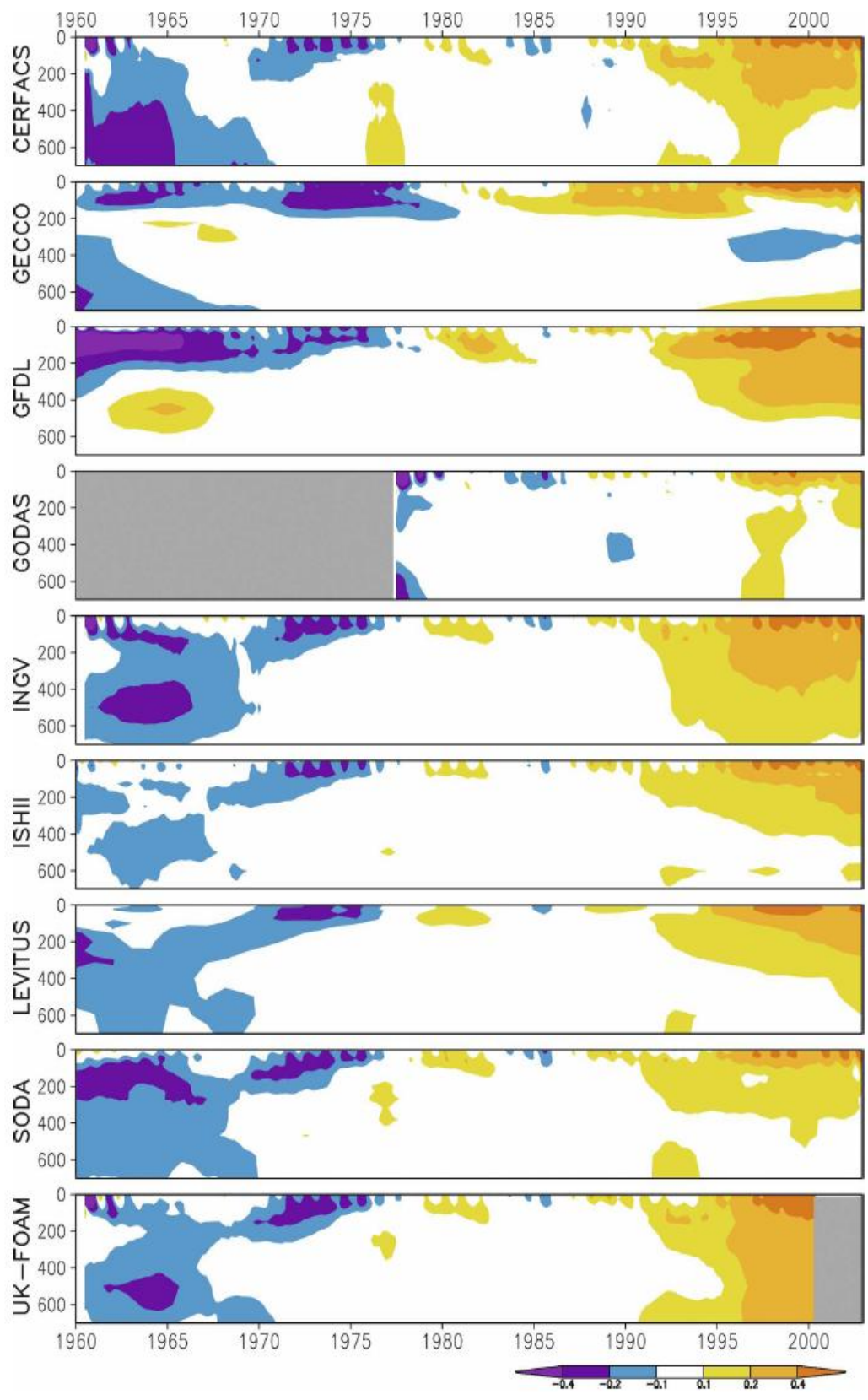
Figure 2.6.   North Atlantic (0°–60°N, 80°–0°W) temperature anomalies relative to the

30-yr record means (1966–95), plotted with depth and time. Anomalies exceeding ±0.1°C

are shaded.
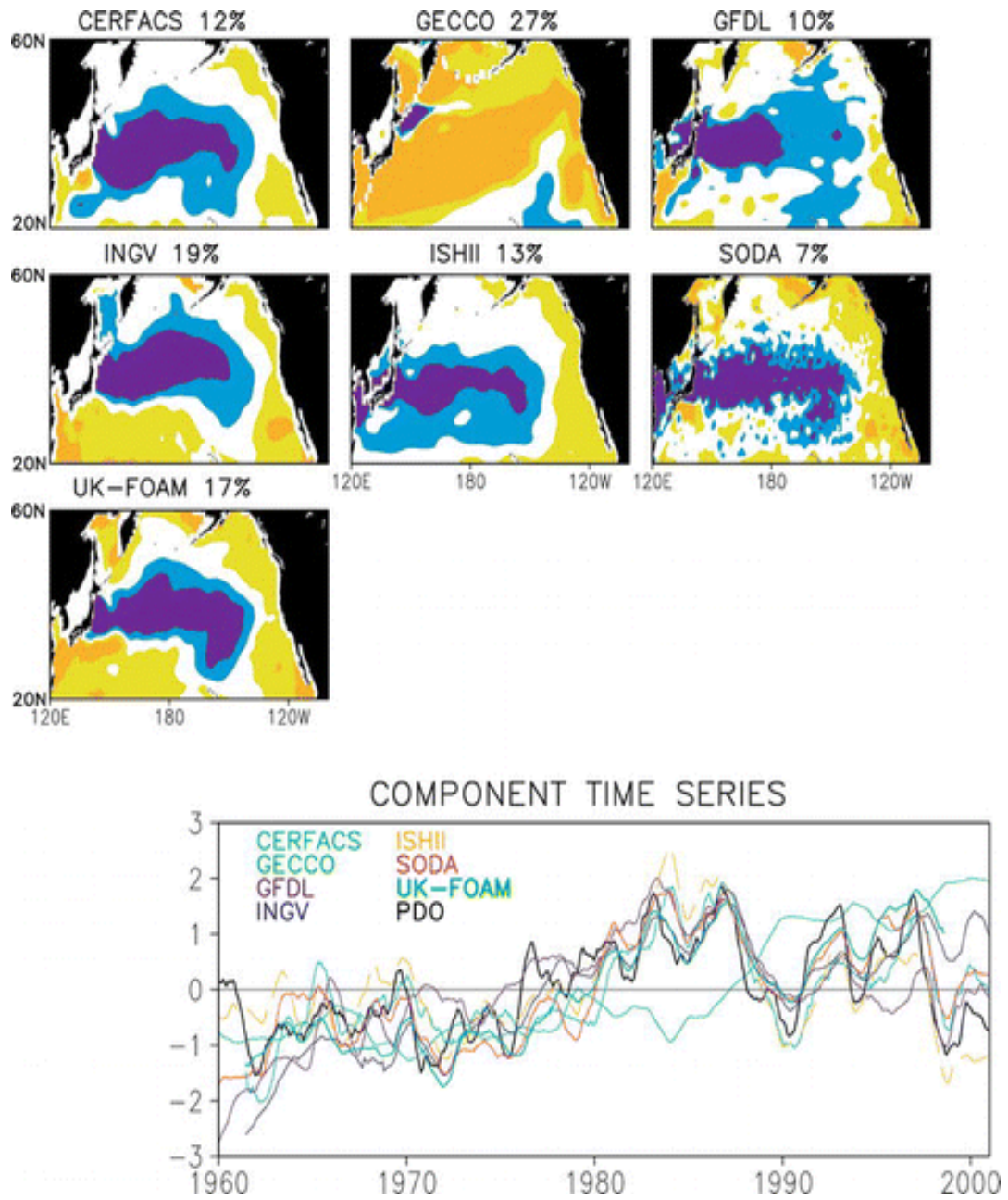
Figure 2.7. First empirical orthogonal eigenfunction of monthly heat content anomaly

in the 20°–60°N latitude band (GODAS and LEVITUS not shown). Colors are plotted at

± 1 and $\pm 3 \times 10^8$ J m^{-2}. Explained variance is shown on the title line. Lower panel shows

the corresponding component time series annually averaged along with the Pacific

Decadal Oscillation index of Mantua et al. (1997) in black.
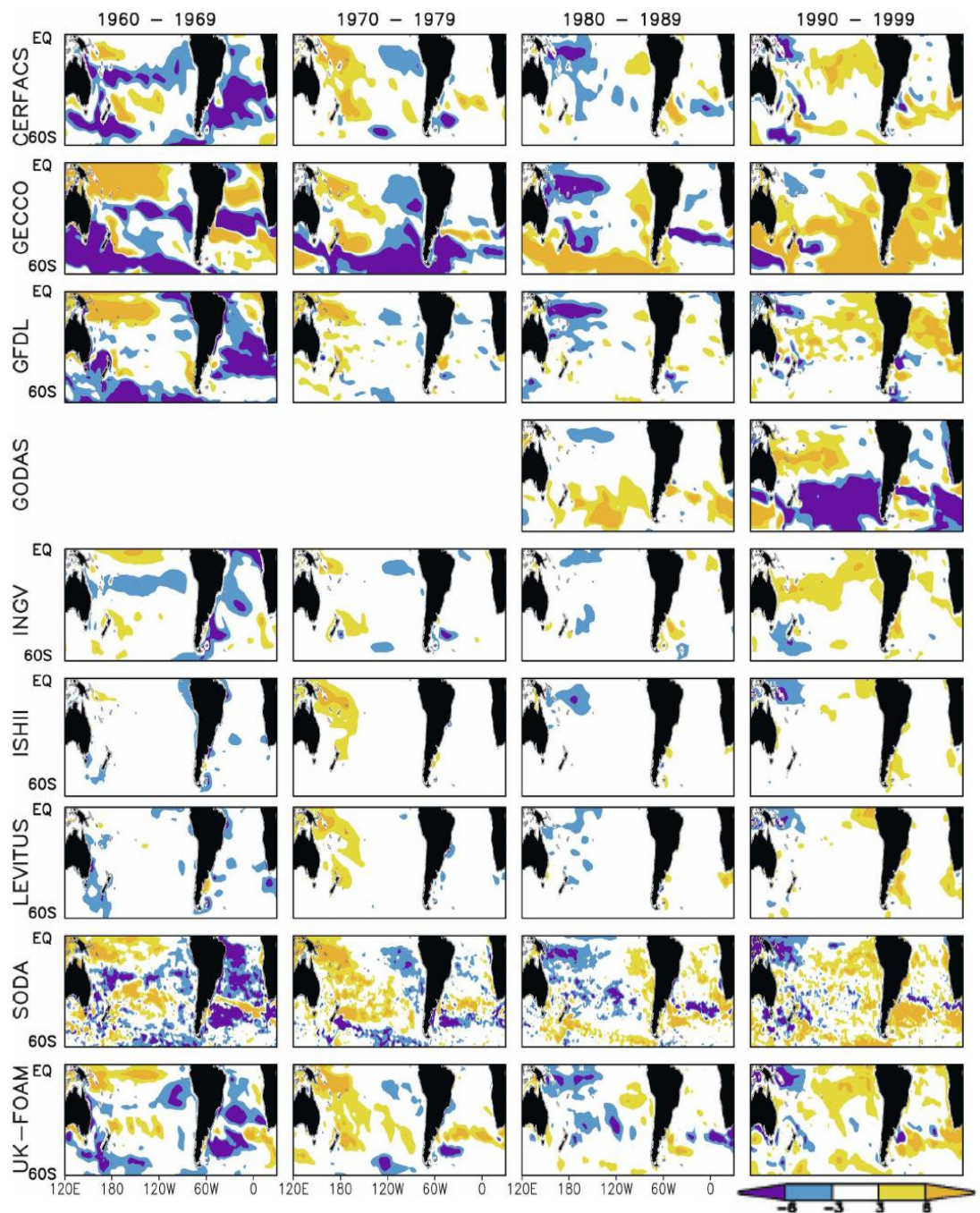
Figure 2.8.   Decadally averaged heat content anomaly in the South Pacific and South

Atlantic sectors for four decades: 1960–69, 1970–79, 1980–89, and 1990–99. Anomalies

exceeding $\pm 3 \times 10^8$ J m^{-2} are shaded.
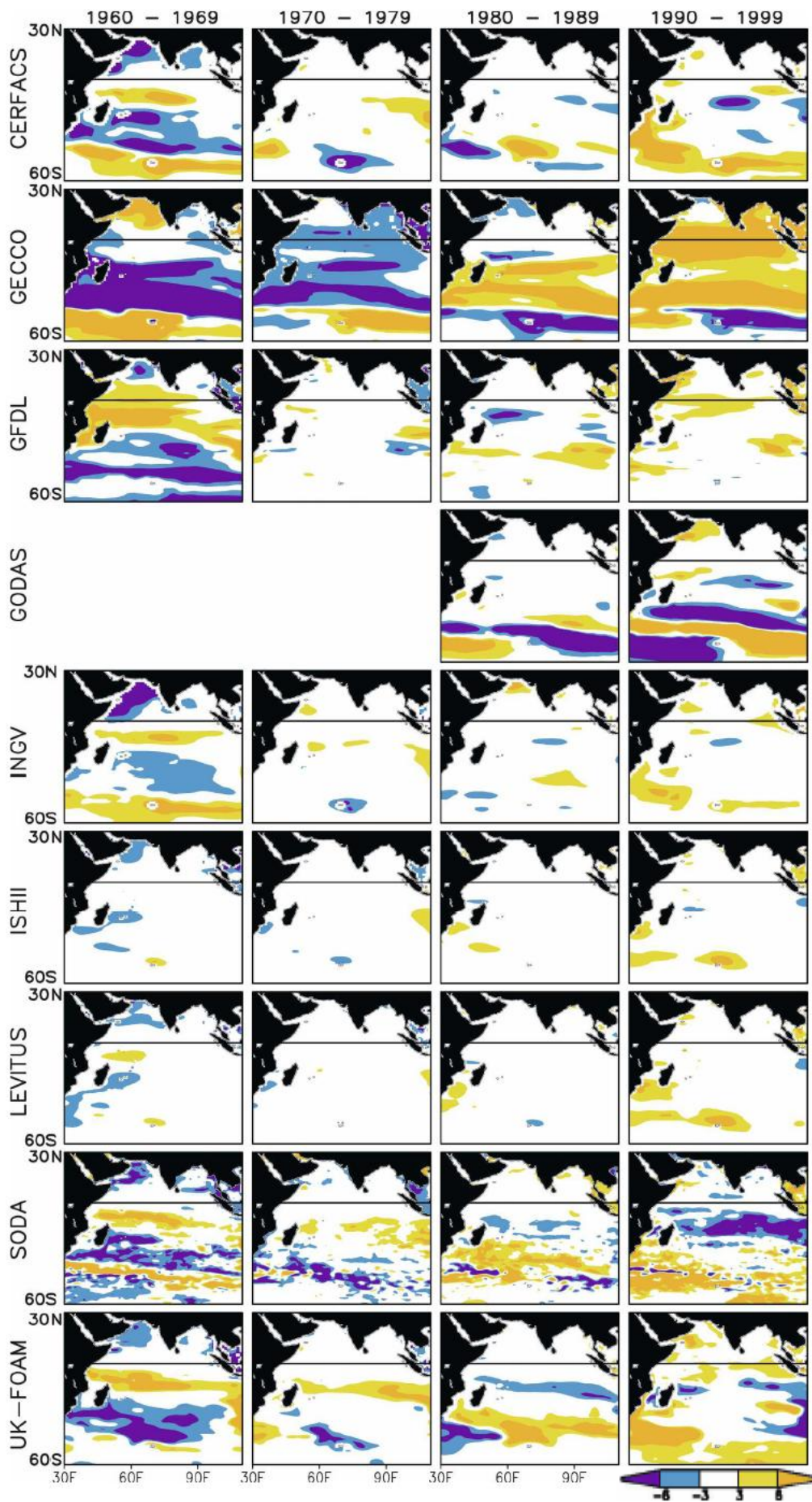
Figure 2.9.   Indian Ocean heat content anomalies relative to the 30-yr record means (60°S–30°N, 30°–110°E) averaged by decade: 1960–69, 1970–79, 1980–89, and 1990–99. Anomalies exceeding $\pm 3 \times 10^8$ J m^{-2} are shaded.
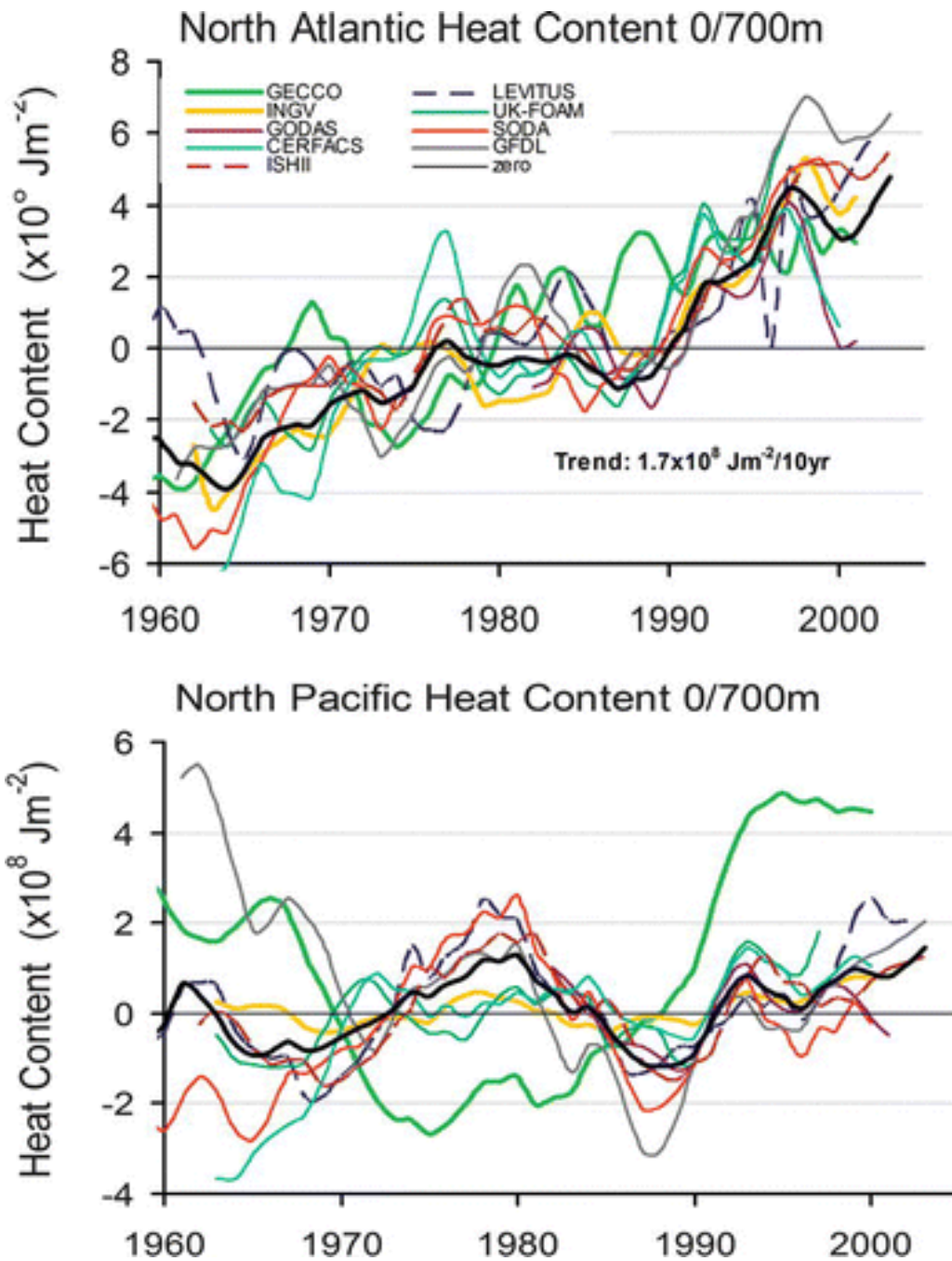
Figure 2.10. Basin-averaged heat content anomalies from the individual 30-yr record means (1966–95), integrated 0/700 m and temporally smoothed with a 3-yr running filter. Bold black curve shows the ensemble average of the nine no-model and sequential analyses: (a) North Atlantic and (b) North Pacific.
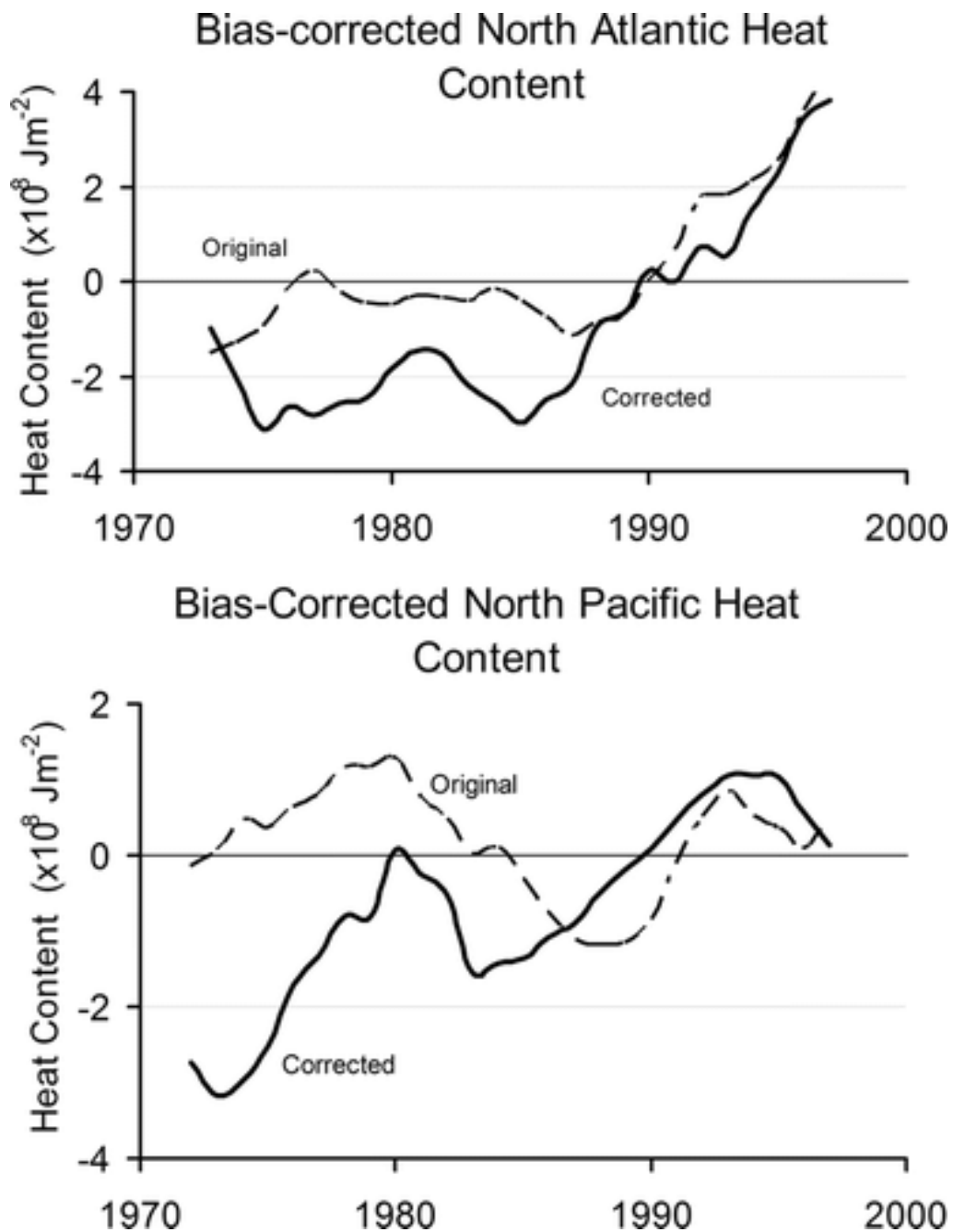
Figure 2.11.   Ensemble average of basin-averaged heat content anomalies for the (a)

North Atlantic and (b) North Pacific (from Fig. 2.10). Dashed black curves show the

original ensemble average analysis for six monthly analyses (CERFACS, GFDL, INGV,

ISHII, SODA, and U.K. FOAM). LEVITUS and GODAS are excluded from the latter

calculation because of their shorter duration or coarser time sampling. Solid curve shows

ensemble average when the analyses are corrected for the analysis minus CTD difference (corrected).

Chapter 3: Examinations of differences between two estimates of air-sea heat fluxes in the Atlantic Ocean

3.1 Abstract

Uncertainties in turbulent ocean-atmosphere heat flux estimates, both among the estimates and between them and ground truth, suggest that further comparisons are needed. Estimates from the French Research Institute for Exploitation of the Sea (IFREMER) and the Woods Hole Oceanographic Institution's Objectively Analyzed air-sea Fluxes (WHOI OAFlux) are analyzed.   The IFREMER products are based on satellite observations and the WHOI OAFlux ones on data from satellites, buoys, and ships assimilated into numerical analyses. The focus is on the Atlantic sector (70°W-30°E, 45°S-45°N) during 1996-2005, where the variables that enter the bulk formulae for computing fluxes (wind speed, sea surface and air temperature, and specific humidity) can be evaluated against buoys in the Prediction and Research Moored Array in the Atlantic (*PIRATA*). Since WHOI assimilates *PIRATA* observations, two independent buoy datasets have been added: *FETCH* and *ROMEO*. To examine how each variable contributes to the difference between estimated and buoy fluxes, the method of Bourras (2006) is applied. His so-called Q terms showed that specific air humidity and air temperature contributed the most to the biases of IFREMER latent and sensible heat fluxes, respectively at both independent buoys. For WHOI OAFlux products, deviations from *FETCH* values were mainly due to wind speed and sea surface temperature differences, while in comparison with *ROMEO* fluxes, WHOI OAFlux biases were primarily due to specific humidity and sea surface temperature estimates. Modified

estimates of turbulent fluxes with the IFREMER approach using the 10 m specific humidity and air temperature products of Jackson et al. (2009) show significant improvement in three test cases at *PIRATA* buoys.

3.2 Introduction

3.2.1 Background

Air-sea heat flux or the exchange of heat between the atmosphere and ocean, controls seasonal variations of sea surface temperature (SST), and, in turn, seasonal to interannual climate variability (Niiler and Kraus, 1977; Houghton, 1991; Cayan, 1992; Yu et al., 2006). There is also an intraseasonal response in SST to latent heat flux over the ocean interior with the exception of areas of equatorial upwelling, such as the eastern tropical Atlantic cold tongue region (Grodsky et al., 2009). The impact of air-sea heat flux on SST is also manifested in hurricane intensification, as ocean-to-atmosphere heat fluxes on the order of thousands of watts per meter squared are released when a hurricane moves over warm tropical waters, cooling the upper ocean but warming the atmosphere and producing enhanced convection (e.g. Shay et al., 2000; Cione and Uhlhorn, 2003). Two seasonal to interannual modes of SST variability in the tropical Atlantic that are controlled mainly by latent heat fluxes have impact on American and African climates (Servain et al., 1998): 1) an equatorial seasonal-interannual mode involving SST anomalies that is akin (but unrelated) to the El Niño-Southern Oscillation events (Wang et al., 2006), and 2) an Atlantic meridional SST gradient mode (5°-25°N, 5°N-20°S) associated with the location and intensity of the ITCZ (Mestas-Nuñez and Enfield, 1999).

Accuracy of air-sea heat flux estimates must be optimal for correct observation and modeling of these climatic phenomena.

This chapter focuses on the turbulent latent and sensible heat fluxes, at the air-sea interface, leaving the radiative terms for separate publications, but keeping in mind that all the energy flux terms contribute to net heating or cooling of the upper ocean. The radiative fluxes obtained by satellite measurements at the top of the atmosphere require very different methods of analysis, including radiative transfer modeling, and use a different set of satellite observations. The ultimate goal of our group is, however, to produce a complete data set where all the flux terms have been produced and are fully evaluated and therefore the net flux is well characterized.

Bulk parameterizations of the air-sea turbulent fluxes are used in numerical models as well as with satellite based observations to estimate surface fluxes. These are based on the Monin-Obukhov similarity theory (MOST) to formulate fluxes in terms of mean quantities (Fairall et al., 2003):

$$\overline{w'x'} = c_x^{\frac{1}{2}} c_d^{\frac{1}{2}} S \Delta X = C_x S \Delta X \qquad (3.1)$$

where w' represents vertical velocity, x can be the water vapor specific humidity, q or potential temperature, θ, and the prime represents deviations from the mean. Here, c_x is the bulk transfer coefficient for the variable x (d being used for the wind speed), and C_x is the total transfer coefficient. Here, ΔX is the air-sea difference in variable X; the mean value of x ($\Delta X = X_{sea} - X(z)$), and S is the mean wind speed (relative to the ocean surface). The transfer coefficients depend on surface stability prescribed by MOST

$$c_x^{\frac{1}{2}}(\zeta) = \frac{c_{xn}^{1/2}}{1 - \frac{c_{xn}^{1/2}}{\kappa} \psi_x(\zeta)} \tag{3.2}$$

$$c_{xn}^{1/2} = \frac{\kappa}{\ln(\frac{z}{z_{ox}})} \tag{3.3}$$

where n refers to neutral stability (when ζ=0), z is the height of measurement of the mean quantity $X(z)$, ψ_x is an empirical function describing the stability dependence of the mean profile, κ is von Karman's constant, and z_{ox} is the roughness length that characterizes the neutral transfer properties of the surface for x. The MOST stability parameter, ζ, is given as:

$$\zeta = \frac{-\kappa g z}{T} \frac{(\overline{w'\theta'} + 0.61\, T\overline{w'q'})}{-\overline{w'u'}^{3/2}} \tag{3.4}$$

where T is temperature, g is the acceleration due to gravity, and $-\overline{w'u'}$ is the stream-wise component of momentum flux with u representing horizontal velocity.

The bulk parameterizations of latent and sensible heat fluxes are given as

$$LHF = \rho L_V C_E U_A (Q_S - Q_A) \tag{3.5}$$

$$SHF = \rho c_p C_H U_A (T_S - T_A) \tag{3.6}$$

where ρ is air density, L_V is the latent heat of vaporization, c_p is the specific heat capacity of air at constant pressure, and Q_A, T_A and U_A are specific humidity, air temperature and wind speed at a specified height above the surface. Q_S and T_S are the specific humidity and temperature at the sea surface; Q_S is assumed to be 98% of the

saturation humidity at sea surface temperature; C_E and C_H are moisture and heat exchange coefficients.

3.2.2 Previous studies

In previous studies several datasets of turbulent air-sea heat fluxes as well as the variables used to calculate them (air temperature, specific humidity, wind speed, and sea surface temperature) have been evaluated to examine uncertainty of flux estimates.

Schulz et al. (1997) compared latent heat fluxes estimated using Special Sensor Microwave/Imager (SSM/I) wind speed and humidity and Advanced Very High Resolution Radiometer (AVHRR) SST data to those made using in situ observations from several field projects in the Atlantic and Pacific [weather-ship M in Atlantic, the Tropical Ocean Global Atmosphere Program's Coupled Ocean Atmosphere Response Experiment (TOGA-COARE) and the Central Equatorial Pacific Experiment (CEPEX) in the Pacific] as well as a dataset of ship/buoy measurements. Differences between satellite and ship/buoy data (instantaneous) are 30 W m^{-2} reduced to 15 W m^{-2} if averaged monthly.

Josey (2001) compared fluxes from the National Centers for Environmental Prediction-National Centers for Atmospheric Research-National Center for Atmospheric Research (NCEP-NCAR; Kalnay et al., 1996), and the European Centre for Medium-Range Weather Forecasting (ECMWF; Gibson et al., 1997) to those of WHOI research buoys during the Subduction experiment in the Northeast Atlantic (1991-93; 18°-33°N, 22°-34°W). Net ocean heat gain was underestimated by the re-analyses, due to overestimation of latent heat loss as well as underestimated shortwave radiation gain. Choice of bulk algorithms in the models seemed to be the cause of latent heat biases.

Southampton Oceanography Centre (SOC) ship-based fluxes were closer to the buoys' values but still showed some differences (<5 W m^{-2} for sensible, <20 W m^{-2} for latent) fluxes, respectively).

Smith et al. (2001) compared NCEP re-analyses to World Ocean Circulation Experiment (WOCE) research vessel observations, and found that NCEP latent and sensible heat fluxes were largely overestimated in the re-analyses. Kubota et al. (2003) compared LHF of version 1 of the Goddard Satellite-Based Surface Turbulent Fluxes (GSSTF-1;Chou et al., 1997), the Hamburg Ocean Atmosphere Parameters and Fluxes from Satellite Dataset (HOAPS) (Grassl et al., 2000), the Japanese Ocean Flux Datasets with Use of Remote Sensing Observations (J-OFURO; Kubota et al., 2002), NCEP and ECMWF re-analyses for 1992-94 and the daSilva (1994) dataset over global oceans. They found that large-scale patterns of latent heat flux are similar but that large quantitative differences among various products exist.

Chou et al. (2004) compared monthly latent heat flux estimates over the oceans during 1992-93 using: version 2 of the Goddard Satellite-Based Surface Turbulent Fluxes (GSSTF-2; Chou et al., 2003), HOAPS, the NCEP reanalysis and the daSilva dataset. Large-scale patterns of the 2-year mean 10 m wind speed, 10 m specific humidity and sea-air humidity differences were similar among the datasets, but there were significant quantitative differences. The daSilva dataset had large differences with GSSTF-2 for all variables in the southern extra-tropics. NCEP had low temporal correlation and large differences with GSSTF-2 for sea-air humidity differences in the Tropics (~0.5-1.5 g kg^{-1}). NCEP also exhibited larger latent heat fluxes than GSSTF-2 in the Tropics as well as in the Gulf Stream and Subtropics with a maximum difference of 40 W m^{-2}. In addition,

the HOAPS mean latent heat flux was significantly smaller than GSSTF-2 by ~31% (37 W m^{-2}) over the Tropics; HOAPS had systematically smaller latent heat fluxes than GSSTF-2 with a globally-averaged difference of 20 W m^{-2}. This difference can be attributed to HOAPS exhibiting smaller 10 m wind speeds than those of GSSTF-2 by up to 2 m s^{-1} as well as larger 10 m specific air humidity values. The other two datasets had large spatial variations of large positive and negative flux differences compared to GSSTF-2 that cancelled to produce smaller regional-mean differences.

Bourras (2006) compared five monthly satellite products of latent heat flux, including GSSTF-2, the second version of HOAPS (Fennig et al., 2006), J-OFURO, the Jones et al. (1999) dataset, which is limited to 30°S-30°N, and the Bourras-Eymard-Liu dataset (BEL; Bourras et al., 2002) to ground observations. These included Tropical Atmosphere-Ocean array (*TAO*) buoys, National Data Buoy Center (*NDBC*) buoys off the U.S. coasts, and Met Office/Meteo-France (*UK-MF*) moorings west of United Kingdom and France for the period of 1998-2000. Examination of the deviation between satellite and surface data using bulk variables was performed using an approach where the bulk formula for latent heat flux was differentiated to form "Q terms," or contributions to the deviation between satellite and surface data (in W m^{-2}) for each of the bulk variables (see Appendix for details).

It was found that all of the satellite datasets except those of Jones et al. (1999) had systematic errors ranging from -13 to -26 W m^{-2} and biases of 6-8 W m^{-2} at mid-latitudes. In the Tropical Pacific, the systematic deviation between latent heat fluxes from the *Jones et al.* dataset and *TAO* buoys was 49 W m^{-2}. In this region, it was found that the lack of accuracy in specific air humidity posed problems for satellite flux estimates. The Q term

63

corresponding to differences in specific air humidity was responsible for almost all of the total Q term averaged over all *TAO* buoys for HOAPS-2 (10 W m^{-2}), and the Q terms for specific surface and air humidity contributed 10-15 W m^{-2} each to the uncertainty of GSSTF-2 latent heat fluxes. Note that the Jones et al. dataset did not provide specific humidity estimates, so no comparison to ground truth was provided.

In addition to uncertainties in flux estimation due to differences in input variables uncertainties due to differences in the formulation of bulk algorithms are considered. Zeng at al. (1998) used TOGA COARE ship data and the multiyear hourly TOGA Tropical Atmosphere-Ocean moored buoy data to compare six different algorithms widely used in research, forecasting and data reanalysis. The study showed that algorithms differ significantly in heat and momentum fluxes under both weak and strong winds. Vapor pressure reduction of 2% over saline seawater (used in COARE3.0) has a significant impact on latent heat flux estimates under strong wind conditions. Chang and Grossman (1999) compared five bulk flux formulae using the same observations in the COARE region (RV Moana Wave; November 1992-February 1993), with a focus on light wind conditions. For most of the algorithms, the bulk flux differed from the covariance flux due to wind-speed dependent bias in the model surface flux parameterization. Further error analysis also showed that instrument uncertainties in the inputs to the formulae also contributed to bulk flux errors.

Brunke et al. (2002) performed an inter-comparison of eight bulk algorithms for the tropical Pacific and mid-latitude Atlantic, including the Coupled Ocean-Atmosphere Response Experiment (COARE; Fairall et al., 1996), the Smith (1988) algorithm used to produce the HOAPS dataset, as well as algorithms used in several models and re-

analyses. Hourly and monthly flux values were estimated by these eight algorithms using data from several buoy experiments, including the *TAO* array. The results showed significant differences in fluxes due to the handling of the wave spectrum, convective gustiness and salinity as well as roughness length and the parameterization of the turbulent exchange coefficients.

Some algorithms showed deviations from observations under certain conditions; for hourly fluxes, there were large differences in both latent and sensible heat fluxes at weak and strong winds. For wind speeds between 10.75 and 11.25 m s^{-1}, differences among algorithms were as large as ~57 W m^{-2} for latent heat flux and ~3 W m^{-2} for sensible heat flux. Differences in monthly mean latent heat fluxes occurred for very unstable conditions; at an SST of 28° ± 0.25°C, the maximum difference in latent heat flux was ~23 W m^{-2}. Over the Tropical Pacific, the maximum average difference in monthly heat flux among algorithms was ~18 W m^{-2}. Over the mid-latitude Pacific, algorithms calculated latent heat fluxes that were consistent with observations.

Furthermore, Brunke et al. (2003) evaluated twelve bulk aerodynamic algorithms (eight of which were used in the 2002 study) and ranked them by using direct turbulent flux measurements determined from covariance and inertial-dissipation methods from twelve ship cruises over the tropical and mid-latitude oceans. The top four algorithms were version 3 of the COARE algorithm (COARE3.0; Fairall et al., 2003), the University of Arizona scheme (Zeng et al., 1998), the ECMWF algorithm (Beljaars, 1995a,b) and the scheme used for version 1 of the Goddard Earth Observing System reanalysis (GEOS-1; Chou, 1993).

Smith et al. (2010) carried out a comparison between nine turbulent flux products including momentum as well as latent and sensible air-sea heat fluxes. They included several re-analysis products and two satellite ones, an early version of HOAPS and IFREMER's. They had two flux products based on in situ data, their own from Florida State (FSU) and the National Ocean Center one. This study has in part been super-ceded by recent improvements in several of these products, which they state in their conclusion, but their discussion may still be very helpful for researchers using one of the many re-analysis products. They state in their conclusion, that "no one product is ideally suited for every application," and they give some practical advice on how to make a choice.

3.2.3 Research and Study Objectives

In this study, the IFREMER and the WHOI OAFlux datasets are compared to each other as well as to ground truth from several field programs for the period of 1996-2005 to understand the reasons for their differences. The variables that enter the computations of the fluxes, such as sea surface and air temperature, wind speed, and specific humidity, are also compared. In the next section, the datasets included in the comparison are described. Then, the comparison methodology is discussed. In the *Results* section, the spatial and temporal differences in latent and sensible heat fluxes are presented, followed by a qualitative and quantitative discussion of the input variables. Each component is compared to independent "ground truth" from the field experiments. In this section test cases are also presented, where the Jackson et al. (2006, 2009) method for obtaining atmospheric specific humidity and air temperature have been used in the IFREMER computations. Finally, a summary of our findings is provided.

3.3 Data sets

The IFREMER data are available at http://cersat.ifremer.fr/layout/set/print/news/ products_informations/new_release_of_satellite_turbulent_fluxes_1992_2007 (Bentamy et al., 2008) as weekly and monthly estimates on a $1° \times 1°$ (latitude $\times$ longitude) spatial grid. The WHOI OAFlux data are available for years 1985-2010 as daily estimates on a $1° \times 1°$ spatial grid (Yu et al., 2008). Table 3.1 lists each variable used to calculate latent and sensible heat fluxes for IFREMER and WHOI OAFlux and the sources of the information. Each meteorological input variable and resulting flux term will be discussed separately.

Both IFREMER and WHOI use the most recent release of the Reynolds SST analysis (Reynolds et al., 2007). The data have a 0.25° horizontal resolution at daily time scale. WHOI utilized the Reynolds SST product based on the Advanced Very High Resolution Radiometer (AVHRR) infrared observations for January 1985-December 2005; IFREMER uses the same product through 2002 and AVHRR data merged with the Advanced Microwave Scanning Radiometer-Earth Observing System (AMSR-E) data from 2002 onward. Both versions of the Reynolds SST dataset are subjected to optimal interpolation (OI). In addition to the satellite SST retrievals from AVHRR and AMSR-E, the Reynolds products assimilate observations from ships and buoys from the International Comprehensive Ocean-Atmosphere Data Set (ICOADS). For the marginal ice zone, sea ice data from microwave satellite data by Grumbine (1996) with delayed sea ice concentrations by Cavaleri et al. (1999) are used to mask the ice edge. IFREMER and WHOI OAFlux interpolated the Reynolds dataset to 1° resolution.

In addition to the Reynolds SST dataset, WHOI also utilized SST values from re-analyses by the European Centre for Medium Range Forecasting 40-Year Reanalysis (ERA-40) project (Beljaars and Kallberg, 2001) and from NCEP (Kistler et al., 2001). The ECMWF system consists of a forecast model at T59 resolution (125 km horizontal resolution, with 60 vertical levels up to 64 km) and a three-dimensional variational data assimilation scheme with six-hour intervals. The observations used to derive the reanalysis includes in situ data from ICOADS, ship observations and radiosondes, as well as satellite radiances from TOVS (TIROS Operational Vertical Sounder) water vapor data from the Special Sensor Microwave/Imager (SSM/I) and wind data from scatterometers. Sea surface temperatures and sea-ice interface are prescribed from the United Kingdom Meteorological Organization Hadley Centre (HadISST1) monthly SST and ice limit analyses and the NCEP (2DVAR) weekly SST and ice limit analysis.

The SST data from the re-analyses are re-gridded by WHOI to 1° resolution for ease of synthesis with the Reynolds SST data through objective analysis (used for all surface meteorological variables and fluxes); this analysis is based on the Gauss-Markov theorem, which states that the linear least squares estimator is the most efficient estimator when combining data linearly, with the solution of minimum variance. Yu et al. (2008) performed error estimation between analysis and in situ observations using the National Oceanographic Centre (NOC) surface meteorology and air-sea heat flux ship measurement climatologies as well as buoy measurements from the WHOI Improved METeorological instruments (*IMET*; Moyer and Weller, 1997), the *TAO/TRITON* buoy array in the Tropical Pacific (McPhaden et al., 1998) and in the Indian Ocean (McPhaden et al., 2006), and the Pilot Research Moored Array in the Tropical Atlantic (*PIRATA*;

Servain et al., 1998). An assumption was made that NOC data errors were several times smaller than those of Numerical Weather Prediction, making the error covariance of NOC data negligible. This error information was used to determine weights that indicate how each dataset used in the WHOI OAFlux product (ERA40, NCEP1, NCEP2 and satellite) contributed to the final estimate of air-sea fluxes and flux parameters. ERA40 specific air humidity and air temperature had larger weights assigned to them than values from both NCEP re-analyses, and satellite SST and wind speed made greater contributions compared to those of re-analyses.

IFREMER uses an empirical model relating SSM/I brightness temperatures to the specific air humidity at 10 m (Bentamy et al., 2003; Schulz et al., 1993, 1997). Brightness temperatures were provided by the Marshall Space Flight Center. WHOI applied the Chou et al. (1995, 1997) algorithm to SSM/I precipitable water and field humidity soundings from the ocean at 10 m height, which is a second-order approximation of the EOF expansion for the specific humidity profile; this was deemed appropriate because the first EOF is related to total precipitable water, and the second EOF is related to the fraction of precipitable water in the PBL. The SSM/I humidity was first height-adjusted from 10 m to 2 m based on version 3.0 of the Coupled Ocean Atmosphere Research Experiment (COARE3.0; Fairall et al., 2003) algorithm. WHOI OAFlux estimation also used values for 2 m specific humidity from the NCEP and ECMWF re-analyses and applied advanced objective analysis to the inputs.

IFREMER winds are mainly derived from scatterometers onboard the European Remote Sensing satellites 1 and 2 (ERS-1 and ERS-2), the Advanced Earth Observing Satellite 1 (ADEOS-1) and QuikSCAT. To enhance the sampling of surface wind speed

69

at grid points where no scatterometer retrievals are available, winds were estimated with brightness temperatures from SSM/I onboard F11, F13, F14, and F15 as inputs into an algorithm published by Bentamy et al. (1999). Both radar and radiometer retrievals are used to estimate daily-averaged winds over the global ocean with spatial resolution of 1° in longitude and latitude. Similar to IFREMER, WHOI OAFlux uses QuikSCAT and version 6 of the Special Sensor Microwave/Imager (SSM/I) data. The algorithm used to derive the SSM/I data (Wentz, 1997) relates wind speed to brightness temperature computed from the 37 GHz horizontal and vertical polarized radiance measurements and to the radiative transfer and absorption between the sea surface and satellite. The data used were 12-hourly at a swath resolution of 25 km. Wind speeds were flagged if cloud/rain liquid water values exceeded 18 mg cm^{-1} because the accuracy of wind speed retrievals degrades if rain is present. Wind speed values were also flagged if measurements are within 50-100 km of the coast or within 200 km of the climatological monthly mean position of the ice edge. In addition to the sources cited, WHOI also utilizes AMSR-E data as well as data from NCEP and ECMWF re-analyses. A variational method is applied to the data, which is subjective due to the determination of weights. Wind measurements from both IFREMER and WHOI OAFlux are converted to the equivalent wind speed at 10 m height and to neutral stratification.

IFREMER uses specific humidity, surface wind speed and sea surface temperature as inputs to calculate air temperature following Konda et al. (1996):

$$q_s - q_a - (C_h/C_e)(T_s - T_a)(A + B) = 0 \qquad (3.7)$$

$$A = \frac{q_a}{Q_*(T_a)} \left(\frac{\partial Q_*(T)}{\partial T} \text{ at } T = T_a \right) \tag{3.8}$$

$$B = Q_*(T_a) \left(\frac{\partial \alpha}{\partial T} \text{ at } T = T_a \right) \tag{3.9}$$

where q_s and q_a are specific surface and air humidity, α is relative humidity, C_h and C_e are heat and moisture transfer coefficients, T_s and T_a are sea surface and air temperatures, and $Q_*(T)$ is the saturation specific humidity curve, which is determined by transformation of the saturation vapor pressure curve. This method utilized two definitions of the Bowen ratio using flux profile as well as bulk formulas to represent sensible and latent heat fluxes. IFREMER air temperature values are adjusted to 10 m height using COARE3.0.

The WHOI dataset utilized values for air temperature from NCEP and ECMWF re-analyses at 2 m height and applied advanced objective analysis to the data; the analysis of air temperature was processed from September 1, 2002 to December 31, 2006 using the ERA-interim reanalysis (Berrisford et al., 2009) to replace NCEP. This was done because it was found that NCEP caused Gibbs-like phenomena, or a spurious oscillation of over- and under-shooting that arises due to the use of an eigenfunction series at a simple discontinuity over the ocean near steep orography (Navarra et al., 1994); this phenomena has been found to affect surface flux estimation since Gibbs oscillations can interact and cause problems with physical parameterizations. The ERA-interim reanalysis uses cycle 31r2 of ECMWF's Integrated Forecast System (IFS), with 60 vertical levels, T255 spherical-harmonic representation for dynamical fields, and a reduced Gaussian grid with approximately uniform 79 km spacing for surface and other grid-point fields.

To obtain turbulent fluxes, both groups utilize the Coupled Ocean Atmosphere Research Experiment version 3.0 algorithm (COARE3.0; Fairall et al., 2003). Although COARE3.0 incorporates sub-models that represent the millimeter-scale cool skin near the interface, the IFREMER implementation does not include this feature. IFREMER used a constant value for surface pressure, while WHOI used a surface pressure field and applied an advanced objective analysis scheme to the data in Table 3.1 before it was used as input in COARE3.0, as discussed earlier. Fairall et al. (2003) stated that, for wind speeds greater than 5 ms^{-1}, surface waves are dominant in affecting surface roughness of the ocean. Two recent parameterizations (Taylor and Yelland, 2001; Oost et al., 2002) that allow the Charnock parameter or velocity roughness length to be calculated from wave parameters were incorporated into COARE3.0. The wave models in COARE3.0 were not used by IFREMER in the flux estimate formulation, while WHOI OAFlux utilized them.

3.4 Methods

To examine differences among datasets daily, monthly and seasonal estimates of each flux component are used for 1996-2005 in a sector of the Atlantic Ocean (70°W-30°E, 45°S-45°N). The comparisons of the gridded fields are done with each other as well as with independent in situ data from buoys (*PIRATA*/*FETCH* /*ROMEO*). Bias, root mean squared difference (RMSD), and correlation among datasets for each component are calculated. For the three buoy datasets, in order to examine the deviation between the air-sea flux estimates and the independent ground truth, the "Q term" approach of Bourras (2006) is applied to both latent and sensible heat fluxes.

Buoy measurements from the Prediction and Research Moored Array in the Atlantic (*PIRATA*; Servain et al., 1998) are used as ground truth. The *PIRATA* project began in 1997 utilizing Autonomous Temperature Line Acquisition System (ATLAS) moorings, with multivariate measurements, and a real-time data stream submission. Measurements below the surface are transmitted to a processor on the surface buoy from sensors inductively coupled to the mooring line, and all data are relayed to shore via the Service Argos satellite system. The placement of the buoys was chosen to provide coverage along the Equator for regions of strong wind forcing in the western part of the basin and significant seasonal-inter-annual variability in SST in the central and eastern parts of the basin. *PIRATA* buoys provide wind speed at 4 m and air temperature and specific air humidity at 3 m height.

Since the *PIRATA* data are assimilated into the WHOI OAFlux product via error estimation (see Section 2), evaluation of the WHOI OAFlux product against such in situ data is not independent. Therefore, independent buoy observations that have not been assimilated into the WHOI products will be also used. In particular, data from two deployments of the University of Miami ASIS (Air-Sea Interaction Spar) buoys (Graber et al., 2000) were utilized. An ASIS buoy was moored in the western Mediterranean (42° 58' 56" N, 4° 15' 11" E) during the "flux, etat de la mer, et télédétection en conditions de fetch variable" (*FETCH*) experiment (Hauser et al., 2003). The overall objective of the *FETCH* experiment was to develop and evaluate methods for estimating turbulent fluxes of heat and momentum at the air-sea interface, and to analyze the turbulent and radiative fluxes in coastal regions and their relation to the atmospheric boundary layer. Observations were collected between March 18 and April 10, 1998 every 28.5 minutes,

but averaged daily for the comparison with the satellite fields. The buoy provides surface wind speed at 7 m, sea surface temperature at 2 m below the surface, as well as air temperature and specific air humidity (calculated from relative humidity) at 5 m. See Drennan et al. (2003) for details. A second independent source of observations is the ASIS buoy *ROMEO* (Zhang et al., 2009). This buoy was deployed at 36° 28.4' N, 75°15.3' W as part of the Shoaling Waves Experiment (*SHOWEX*). The buoy is influenced by the Gulf Stream, a region of large discrepancy between IFREMER and WHOI flux estimates; thus, the *ROMEO* data are important for verification in this region. The objective for the deployment of *ROMEO*, as well as the two other ASIS buoys moored during *SHOWEX*, was to measure the evolution of surface waves as well as air-sea fluxes of buoyancy and momentum and mean shelf meteorology. The data set spans October 22-November 30, 1999 at 20-min intervals; the data were averaged at daily time scales to facilitate comparison with the IFREMER and WHOI fluxes. The buoy provides surface wind speed at 6 m, sea surface temperature at 5m depth, as well as air temperature and humidity at 4.5 m.

The measurement height of certain variables is different among datasets. IFREMER estimates variables at 10 m while WHOI uses air temperature and specific humidity data at 2 m and wind speed at 10 m; these data are in both cases from the advanced objective analysis as applied to the original data. Furthermore, as stated above, buoy values of air-sea flux variables are measured at different heights in each of the four cases. To ensure consistency, COARE3.0 was used to make the proper height adjustments to 10 m for specific air humidity, wind speed and air temperature.

3.5 Results

3.5.1 Comparison between IFREMER and WHOI

As evident from Figure 3.1a, within the Atlantic basin, the IFREMER-WHOI OAFlux 1996-2005 annual mean difference in latent heat flux is positive in the Tropics, with a maximum of 60 W m^{-2} off the Brazilian coast. In a region just off the western African coast (30°S-0°N, 15°W-15°E), there is a dipole of negative (between -20 and 0 W m^{-2}) and positive ($\geq$30 W m^{-2}) difference between the two latent heat flux products. There is a band of negative differences between 45° and 30°S with an area $\leq$ -40 W m^{-2} off the South African coast. In the Gulf Stream region (30°-45°N, 70°-40°W), there are also negative differences of up to -40 W m^{-2}. As seen from Figure 3.1b, the IFREMER-WHOI OAFlux 1996-2005 annual mean difference in sensible heat flux is positive in most of the Atlantic basin. Around 45-30°S, IFREMER sensible heat fluxes exhibit the largest difference from WHOI OAFlux ($\geq$ 30 W m^{-2}); there is also a small area of positive differences of 20-40 W m^{-2} just off the western shore of South Africa (30-15°S, 15°E). A region where IFREMER sensible heat fluxes were smaller than those of WHOI is in the Gulf Stream region ($\leq$ -20 W m^{-2}).

Sea surface temperature differences between IFREMER and WHOI OAFlux are mostly small, except in the Gulf Stream region where they exceed 2°C (Figure 3.1c); this could be due to gridding concerns in this area of a large SST gradient as well as the fact that WHOI OAFlux used SST from re-analyses in addition to satellite data. Differences in specific air humidity contribute to latent heat flux discrepancies in all regions (note the similarities between Figures 3.1a and 3.1d, keeping in mind that a negative bias in

specific humidity produces a positive bias in latent heat flux). These differences are negative in the Tropics, with a maximum of -1.5 g kg^{-1} off the Brazilian coast and positive within the 45-30°S belt (0-0.5 g kg^{-1}) and the Gulf Stream, where there is a maximum difference equal to or exceeding 1.5 g kg^{-1}. There is a clear dipole of positive and negative differences between IFREMER and WHOI OAFlux specific air humidity off the western African coast.

IFREMER wind speeds (Figure 3.1e) are higher than those of WHOI OAFlux in the Tropics but lower in the Gulf Stream and between 30 and 10°S, where differences are as high as -1 m s^{-1}. These wind speeds contribute to the differences in latent heat fluxes in these regions except for a larger IFREMER latent heat flux off the southern African coast. Differences in sensible heat flux are likely due to contrasts in air temperature between the two datasets (Figure 3.1f) which are between -1 and 0°C north of the Equator, and between -2 and -1°C south of the Equator. Along ~45°S, the differences are between -4 to -2°C. In the Gulf Stream region, IFREMER air temperature is larger by ≥2°C, but, since sea surface temperature differences are similar, the effect of air temperature may not be as strong as the effect of wind speed in this region.

At seasonal time scale, the strong negative difference in latent heat flux in the Gulf Stream vanishes in the summer months, and the area of negative difference off the West African coast appears to move northward into the Equator and narrows (not shown). However, both the area of negative differences off the South African coast and the area of positive differences along the Brazilian coast persist year-round. These correspond to seasonal differences of opposite sign for specific air humidity. In the Gulf Stream, it appears that the wind speed difference weakens to between -0.5 and 0 ms^{-1} during the

summertime; this coincides with a shift in differences in latent and sensible heat fluxes from very negative to slightly positive (0-20 W m^{-2}) during the same season. The alternation of negative and positive sensible heat flux differences along the West African coast during the summer and fall seasons coincide with air temperature differences of the opposite sign.

The root mean square difference of latent heat flux between the two datasets (Figure 3.2a), is highest in the Gulf Stream region, along the northern coast of South America and along the coast of South Africa; RMSD in these regions is ≥40 W m^{-2}. The RMSD of sensible heat flux between the two datasets (Figure 3.2b) is typically around 10 W m^{-2} but reaches up to 45 W m^{-2} in the Gulf Stream and in the 45°-40°S belt. Also, the RMSD of the bulk variables, including sea surface temperature (Figure 3.2c; reaching a maximum over 4°C in the Gulf Stream region), specific air humidity (Figure 3.2d; differences up to 1.8 g kg^{-1} in the Gulf Stream),wind speed (Figure 3.2e; 1-1.5 m s^{-1} in the 45-30°S region) and air temperature (Figure 3.2f ; up to 3.5°C in the Gulf Stream region, and up to 4.5°C at 45-30°S) are shown.

An analysis of the 1996-2005 IFREMER minus WHOI OAFlux temporal differences for the latent and sensible heat fluxes and their associated input variables was also performed. This is summarized in Figures 3.3, 3.4 and Table 3.2 which include the time series of differences for both the entire basin and zonal belts as well as the overall time-mean difference.

The monthly mean differences averaged over the basin for latent and sensible heat fluxes are 8.9 and 10.1 W m^{-2}, respectively (Table 3.2). For latent heat flux, the

difference is largest in the northern tropical Atlantic (0°N-15°N), while sensible heat flux differences are largest in the 15-30°N and 45-30°S belts. Note that there is an upward trend in the time-mean latent heat flux difference basin-wide (Figure 3.3a); the separate time series of basin-averaged IFREMER and WHOI fluxes show that IFREMER, not WHOI, had the upward trend in monthly-averaged latent heat flux (Figure 3.4a). Examination of the separate time series for each zonally averaged latitudinal belt showed that the basin-averaged time series for this variable were very similar to those of 0°N-15°N (Figure 3.4b).

To explore the causes of the differences between the two datasets, the variables that go into the calculation of the fluxes are evaluated. The time-mean difference in specific air humidity between the two datasets over the basin is -0.2 g kg^{-1} (Table 3.2); this corresponds to a larger IFREMER latent heat flux. The largest negative differences in specific air humidity lie in the southern Tropical Atlantic (15°S-0°N), close to the region where IFREMER latent heat fluxes show the highest values when compared to those of WHOI OAFlux. In Figure 3.3e, there is a noticeable jump in the time-mean difference in wind speed between the two datasets around 2002; looking at individual time series, IFREMER wind speeds show this jump, but those of WHOI do not (Figure 3.4g). The difference between IFREMER and WHOI OAFlux wind speeds averaged over the Atlantic basin for 1996-2005 is 0.2 m s^{-1}, and the largest differences occur in the 0°-15°N region (Table 3.2).

Similar to what is observed in latent heat flux difference, there is also an upward trend in the basin-averaged sensible heat flux difference between the two datasets (Figure 3.3b). Again, when looking at each dataset separately, IFREMER shows the upward trend

(Figure 3.4c), and the 0°N-15°N belt is where the trend is most prevalent. IFREMER's sensible heat fluxes exhibits a much larger seasonal cycle than do those of WHOI OAFlux (Figure 3.4d). For sensible heat flux, variables used in the calculation are sea surface temperature, wind speed and air temperature. Averaged over the Atlantic basin, the time-mean difference between IFREMER and WHOI OAFlux SST is negligible (Table 3.2), so SST cannot explain IFREMER's higher sensible heat fluxes. Note that there is a sudden increase in the basin-averaged time series of differences in SST between the two datasets around 2002 (Figure 3.3c); the datasets appear to differ more after this time, and it is particularly evident in the 0°N-15°N belt (Figures 3.4e and 3.4f). This likely reflects the fact that the WHOI OAFlux product used the AVHRR-only version of the Reynolds et al. (2007) satellite SST product for the entire time period, while IFREMER switched to the merged AVHRR/AMSR-E version of the product starting in 2002. Similarly, the negative differences between IFREMER and WHOI wind speed that exist in belts pole-ward of 15°S would not explain the higher sensible heat flux from the IFREMER data. The time-mean basin-averaged difference in air temperature between the two datasets, -0.9°C, would correspond to a higher sensible heat flux for IFREMER (Table 3.2).

3.5.2 Comparison of IFREMER and WHOI products to ground truth

3.5.2.1 Comparison to PIRATA buoys

Each of the input variables used in computations with both datasets were compared to ground truth, first against *PIRATA* buoys. In Table 3.3, daily values of latent and sensible heat fluxes as well as the variables that enter the bulk formulae were

compared to daily-averaged estimates from 13 *PIRATA* buoys during 1996-2005. For all variables and fluxes, WHOI OAFlux data had a smaller mean bias and stronger correlation when compared with *PIRATA* data. This is expected since the WHOI dataset used *PIRATA* buoys as well as buoys from *IMET* and *TAO* to tune the amplitude of error variances that were constructed based on the use of the NOC air-sea flux and surface meteorology analysis, as mentioned in Section 3.3 (Yu et al., 2008). Hence this is not a true validation of the WHOI products. Also, some scatter found in daily IFREMER and buoy data comparisons are related to the ability to determine the specific air humidity and from that the air temperature from one or two microwave brightness temperature measurements per day. This limited sampling and the indirect evaluation of air temperature are the main reasons why IFREMER flux data are only made available as weekly and monthly averaged products.

The IFREMER and WHOI OAFlux products showed mean latent heat flux biases of +9.2 and -7.1 W m^{-2} respectably when compared with the *PIRATA* data. That the two biases are so close is remarkable given that the WHOI product assimilate the data while the IFREMER one does not. The mean biases in sensible heat flux are +10.1 and +1.7 W m^{-2}, respectively. IFREMER and WHOI SST data both exhibited low biases and correlations near +1 when compared to *PIRATA* data; IFREMER air-sea fluxes and WHOI OAFlux products both use the Reynolds et al. (2007) satellite SST dataset but in different ways as discussed in the *Datasets* section. In addition, WHOI assimilated SST values from *PIRATA* buoys into their estimates. IFREMER air temperature also had a strong correlation with those of *PIRATA* buoys, but one must note that sensible heat fluxes from each dataset correlate poorly due to the difference between SST and air

temperature. It is not necessarily realistic, even though each of those two variables show good statistical small errors compared to buoy data, since their deviations from the true values are not generally correlated with each other.

3.5.2.2 Comparison to the FETCH buoy

Since WHOI uses the *PIRATA* data as part of its assimilation process, it is of interest to evaluate the performance of the two products against observations that were not used by WHOI. Such independent observations are available from the *FETCH* buoy. As seen in Figure 3.5 and Table 3.4, IFREMER latent heat fluxes exhibit a negative bias compared to *FETCH* fluxes of -9.1 W m^{-2}, but sensible heat fluxes are positively biased by 9.7 W m^{-2}; the WHOI OAFlux latent heat flux bias was -3.5 W m^{-2}, while the sensible heat flux bias was only -0.5 W m^{-2}.

The analysis of the Q terms for the IFREMER-*FETCH* comparison shows that the observation-averaged Q_{Q_A} (-15.9 W m^{-2}) contributes the most to the total uncertainty term for IFREMER latent heat fluxes, and Q_{T_A} (7.7 W m^{-2}) contributes the most to the total uncertainty term for IFREMER sensible heat fluxes (Table 3.5). These results correspond to the positive bias in specific air humidity and negative bias in air temperature from the IFREMER data. For the Q term analysis for WHOI-*FETCH*, Q_{U_A} contributes the most to the negative latent heat flux bias (-9.7 W m^{-2}). Any uncertainties in wind speed measurements could be due to difficulties in measuring by satellite the strong Mistral and Tramontane winds, which are northerly-northwesterly winds produced by the synoptic regime and topography of the south of France, north of Italy, and northwest of Spain, found in the experiment area during that time (Hauser et al., 2003).

Also, Drennan et al. (2003) mentioned the importance of swell conditions on the behavior of the wave boundary layer and that the presence of swell waves cannot be scaled based on the Monin-Obukhov theory. Swells can modify and increase the scatter of the drag coefficient relations compared to the pure wind sea regime. Negatively biased WHOI OAFlux sea surface temperature values compared to those from the *FETCH* buoy (-0.3° C) could explain their sensible heat flux bias; this is confirmed by Q_{T_s} contributing the most to the total of the Q terms for WHOI-*FETCH* sensible heat flux (-1.9 W m^{-2}).

3.5.2.3 Comparison to the ROMEO buoy

The independent *ROMEO* buoy is located near the Gulf Stream, an area of large differences between the two data sets as indicated earlier in this section; comparison of flux estimates to the values from experiment is important for the examination of uncertainties. Also note that this area is close to a very strong SST gradient. The RMSD of latent heat flux between IFREMER and *ROMEO* is over 80 W m^{-2}, which is not surprising since specific surface humidity is a function of SST, which satellites may not be able to measure as accurately in areas of high SST gradient (Reynolds et al., 2007). According to Figure 3.5 and Table 3.4, IFREMER latent heat fluxes exhibit a positive bias compared to *ROMEO* latent heat fluxes of 33.1 Wm^{-2}, but sensible heat fluxes are biased by -19.4 W m^{-2}; the WHOI OAFlux latent and sensible heat flux biases were both positive and greater in magnitude than those of IFREMER, 59.0 and 27.9 W m^{-2} respectively.

Using the Q term analysis for IFREMER-*ROMEO* data, a positive observationally-averaged Q_{Q_S} is nearly balanced by a negative Q_{Q_A}, but Q_{U_A} is 26.8

W m^{-2}, which contributes to a positive total Q term for latent heat flux (Table 3.5); this makes sense based on the positive bias exhibited by IFREMER wind speed compared to *ROMEO* data. The major contributor to the total Q term for IFREMER-*ROMEO* sensible heat flux is Q_{T_A}, which corresponds to a large positive bias in IFREMER air temperature of 4.2°C. Also, Q_{T_S} also contributed significantly to IFREMER sensible heat flux uncertainty (31.7 W m^{-2}). This large difference in air humidity and temperature over the Gulf Stream are due in part to the periodic presence of cold, dry continental air over the region. Grodsky et al. (2009) performed a regression analysis that suggested correspondence between the strengthening of intraseasonal latent heat flux in the Gulf Stream region and mid-latitude storm systems in the Atlantic. Increases in latent heat flux in this region correspond to an area of low sea level pressure and cyclonic anomalous winds center east of the region; this anomalous wind decelerates the northern flank of the northeasterly trade winds, and accelerates off-shore flow over the Gulf Stream. The atmospheric boundary layer adjustment (Beal et al., 1997) adds to the acceleration over the warm sector of the Gulf Stream. In addition to wind intensification, the northwesterly wind outbreaks bring cold and dry continental air over the sea as mentioned before, lowering air humidity, and increasing the air-sea moisture gradient. Also, note that satellite algorithms for humidity and air temperature over the ocean are tuned to maritime air masses, and clearly have problems in these regions. This is discussed further below.

For WHOI-*ROMEO*, Q_{Q_S} contributed the most to the total Q term for latent heat flux, since WHOI OAFlux sea surface temperature was positively biased compared to

ground truth; for WHOI OAFlux sensible heat fluxes, Q_{T_S} (29.5 W m^{-2}) contributed most to the total of the Q terms for WHOI-*ROMEO* sensible heat flux.

3.5.2.4 Test of an alternate method for near surface specific humidity and air temperature

When comparing to data from *FETCH* and *ROMEO*, the Q term analysis showed that specific air humidity contributed the most to the bias of IFREMER latent heat fluxes, and air temperature contributed the most to the IFREMER sensible heat flux bias. For estimates of specific air humidity, both datasets used algorithms that were a function of other variables. Satellite brightness temperature from SSM/I were used for the IFREMER estimate, and precipitable water measurements from SSM/I were used for the WHOI OAFlux estimate. However, WHOI also used values for specific air humidity from ERA-40 and NCEP re-analyses. IFREMER calculated air temperature indirectly using the Bowen Ratio method of Konda et al. (1996) that depends on sea surface temperature, surface wind speed and specific air humidity. Any biases in input variables are inherently included in calculating air temperature.

Use of other methods to calculate specific air humidity and air temperature from satellites could aid in more accurate estimates of these variables, and, in turn, in estimates of heat fluxes. For example, Jackson et al. (2006, 2009) derived satellite-based estimates of specific air humidity and air temperature by combining ship, buoy and satellite microwave observations from the Advanced Microwave Sounding Unit (AMSU-A), Special Sensor Microwave Temperature Sounder (SSM/T-2) and SSM/I based on

multiple linear regressions. A multi-sensor approach using microwave sounders can improve the retrieval of these two variables by incorporating additional information about the tropospheric humidity and temperature profiles.

As an initial test, the SST and 10 m wind speed provided by IFREMER and the 10 m specific humidity and temperature from Jackson et al. (2009) [courtesy of G. Wick] are used as input variables into the COARE3.0 algorithm and estimate latent and sensible heat fluxes at three *PIRATA* buoy locations, 15°N, 38°W, 0°N, 10°W and 0°N, 23°W, and at the *ROMEO* buoy location, 36°N, 75° W; these buoys are in areas where fluxes showed the largest discrepancies. The new turbulent flux estimates at these locations (known as IFREMER_2) were compared to ground truth at these locations. As seen in Figures 3.6a-d and Table 3.6, when compared to the *PIRATA* fluxes, at the 15°N, 38°W and 0°N, 10°W buoys, the IFREMER_2 latent and sensible heat flux estimates are significantly improved over that of IFREMER_1 (the original IFREMER estimate) in terms of weekly-averaged bias. As for 0°N, 23°W, the IFREMER_2 latent heat flux estimate are an improvement over WHOI OAFlux, and the IFREMER_2 sensible heat flux bias is lower than that of IFREMER_1 (Figures 3.6e-f, Table 3.6). At the *ROMEO* buoy location, IFREMER_1 actually gives the best latent heat flux estimate, but IFREMER_2 sensible heat flux is superior to those of IFREMER_1 and WHOI OAFlux (Figure 3.7, Table 3.6). Thus, use of the Jackson et al. data and methods can further improve latent and sensible heat flux estimates that are satellite-based, but other modifications in choice of sea surface temperature and wind speed products as well as different implementation of the COARE algorithm need to be considered.

3.6 Summary

Examination of two estimates of annual means of latent and sensible heat fluxes during 1996-2005, from IFREMER and from WHOI OAFlux over the Atlantic basin (70°W-30°E, 45°S-45°N) showed that IFREMER fluxes were larger in most regions with the exception of some small areas off the West African coast, the Gulf Stream region and south of 30°S; this coincides with IFREMER's lower specific air humidity and air temperature values in almost all regions of the Atlantic with the same exceptions as stated above. When compared to the *FETCH* and *ROMEO* buoys, the Q term analysis showed that specific air humidity contributed the most to the total difference between IFREMER and buoy latent heat fluxes, and that the Q term corresponding to air temperature was the largest of the Q terms for IFREMER-buoy sensible heat fluxes.

Another possible explanation is the inability of satellites to account for certain meteorological and oceanographic conditions, such as low level stratus clouds over cold water (Smith et al., 2010). There were high wind speeds as well as a dramatic drop in air temperatures during the period of the deployment of *ROMEO* due to the passage of a cold front (Zhang et al, 2009). It is known that satellites have difficulty capturing effects of atmospheric stratification, when there are cold air outbreaks over the ocean as well as high wind speeds (Bentamy et al., 2003). Thus, in both experiments, uncertainty in satellite estimates compared to ground truth could be attributed to these impacts by the weather regimes, showing a need to improve interpolation in time and space in order for satellite estimates to better reflect conditions during synoptic-scale storms and fronts.

In addition, coastal upwelling present off the West African coast could affect satellite estimates of fluxes, as was seen in the spatial analysis of the differences between IFREMER and WHOI OAFlux in the *Results* section. In cold tongue regions, the mixed layer temperature balance is dominated by not only upwelling but also tropical instability waves that horizontally transport heat (Grodsky et al., 2009). Again, due to the impact of upwelling on stratification, satellites may not be able to identify effects on near surface humidity, air temperature and air-sea fluxes in such areas. The effect of limited input data to numerical analyses in the Southern Hemisphere may also affect the underlying model fluxes in case of WHOI OAFlux estimates. There is no way to know without good in situ comparison data which estimate is better when they differ in systematic ways. Strong storm systems that propagate over the Agulhas Current region off the South African coast produce strong latent heat flux; depending on the location of the storm center, this heat flux is sometimes amplified by anomalous southerly winds that bring dry and cold sub-Antarctic air northward (Grodsky et al., 2009). The satellite observations may be unable to handle this phenomenon properly, which could cause a discrepancy between IFREMER and WHOI OAFlux products in this region. Model fluxes may also suffer here where there is little in situ data to assimilate into the WHOI OAFlux product.

Finally, conditions in the Gulf Stream region present similar challenges in satellite flux estimation, including strong surface currents and SST gradients as well as how the stratified atmospheric boundary layer amplifies air-sea interactions on an intraseasonal timescale (Grodsky et al., 2009). The fact that IFREMER used the Reynolds et al. (2007) product that included AMSR-E data merged with AVHRR data from 2002 on compared to WHOI's use of the AVHRR-only data may have been part of the reason for larger

discrepancies in their SST estimates. It may well be that there are systematic differences between the two products due to the sampling, which leads to three conclusions: i) the merged product (i.e. IFREMER) is better post-2002 due to AMSR and AVHRR merged SST data improving spatial resolution of SST gradient features (Reynolds et al., 2007), ii) the discontinuity in 2002 is an artifact and iii) both AVHRR-only products have larger total error (random plus sampling plus bias; see Reynolds et al., 2007). Some consideration of the limitations of each method in the Gulf Stream and other areas of variable SST and cold air outbreaks may be possible with modern statistical methods. In the past, regionally-varied empirical formulas have been avoided due to artificial boundaries in the resulting products, but the time may now be right for including existing knowledge of regional and seasonal patterns when generating these types of products, especially since the supporting information for making the algorithm choices may be available from NWP models or supplemental satellite observations.

Variable	Source for IFREMER	Source for WHOI OAFlux
Air temperature	Estimated using the *Konda et al.* [1996] model	NCEP, ECMWF re-analyses
Sea surface temperature	*Reynolds et al.* [2007]	NCEP, ECMWF re-analyses, *Reynolds et al.* [2007]
Surface wind speed	ERS-1, ERS-2, QuickSCAT scatterometers SSM/I wind speed	NCEP, ECMWF re-analyses, SSM/I and AMSR-E radiometers, QuickSCAT scatterometer
Specific air humidity	Estimated from SSM/I brightness temperature using the *Schulz* [1993, 1997] model	NCEP, ECMWF re-analyses, product from *Chou et al.*[1997] using SSM/I column water vapor retrievals

Table 3.1.   Variables used to derive IFREMER and WHOI OAFlux turbulent heat

fluxes (latent and sensible) and their origin.

Region	LHF (W m^{-2})	SHF (W m^{-2})	SST (°C)	Q_a (g kg^{-1})	U (m s^{-1})	T_a (°C)
Basin-wide	8.9	10.1	0.0	-0.2	0.2	-0.9
30°-45°N	4.2	6.1	0.6	0.4	0.4	0.0
15°-30°N	13.8	12.3	0.3	-0.1	0.2	-0.9
0°N-15°N	19.0	8.2	0.1	-0.4	0.6	-0.7
15°S-0°N	13.5	8.8	-0.2	-0.6	0.2	-1.0
30°-15°S	8.8	11.5	-0.1	-0.4	-0.1	-1.2
45°-30°S	-1.8	13.4	-0.7	-0.4	0.2	-1.7

Table 3.2.   Monthly-averaged difference between IFREMER and WHOI OAFlux latent heat and sensible heat fluxes (LHF, SHF), sea surface temperature (SST), specific air humidity (Q_a), surface wind speed (U) and air temperature (T_a) for 1996-2005 averaged over the basin (70°W-30°E, 45°S-45°N) and over zonal belts between 70°W and 30°E.

Variable (units)	IFREMER Bias	WHOI Bias	IFREMER RMSD	WHOI RMSD	IFREMER r	WHOI r
LHF ($W\ m^{-2}$)	9.2	-7.1	31.7	23.0	0.7	0.8
SHF ($W\ m^{-2}$)	10.1	1.7	12.3	4.2	0.2	0.6
SST (°C)	-0.1	-0.0	0.4	0.4	1.0	1.0
Q_a ($g\ kg^{-1}$)	-0.3	-0.1	0.8	0.6	0.9	1.0
U ($m\ s^{-1}$)	0.3	0.2	1.4	0.7	0.6	0.9
T_a (°C)	-1.0	-0.1	1.1	0.5	0.9	1.0

Table 3.3.   Bias, root mean square difference (RMSD) and correlation coefficient (r)

between daily *PIRATA* buoy data and IFREMER, WHOI OAFlux data during 1996-2005.

PIRATA buoys included in these comparisons are located at 0°N, 0°E; 0°N, 10°W; 0°N,

23°W; 0°N, 35°W; 10°S, 10°W; 4°N, 38°W; 8°N, 38°W; 12°N, 38°N; 15°N, 38°W; 6°S,

10°W; 19°S, 34°W; 2°N, 10°W and 8°S, 30°W. There were a total of 1,777 observations

available for comparisons among these buoys for each variable (except for SST, which

had 2,591) during 1996-2005.

	FETCH						ROMEO					
Variable (units)	IF B	W B	IF R	W R	IF r	W r	IF B	W B	IF R	W R	IF r	W r
LHF (W m^{-2})	-9.1	-3.5	34.8	21.6	0.8	0.9	33.1	59.0	81.7	10.0	0.8	0.9
SHF (W m^{-2})	9.7	-0.5	20.4	9.6	0.7	0.8	-19.4	27.9	47.2	36.9	0.2	0.9
SST (°C)	-0.1	-0.3	0.4	0.4	0.7	0.6	3.3	3.1	3.6	3.3	0.5	0.7
Q_a (g kg^{-1})	0.5	-0.6	1.0	0.8	0.8	1.0	-1.9	0.0	2.7	0.8	0.9	1.0
U (m s^{-1})	0.8	-0.7	2.5	1.4	0.7	0.9	1.9	0.2	2.6	1.7	0.9	0.9
T_a (°C)	-0.4	-0.1	1.3	0.7	0.7	0.9	4.2	0.4	5.1	1.0	0.1	1.0

Table 3.4.   Bias (B), RMSD (R) and r for LHF, SHF and pertinent

variables calculated in comparisons between daily buoy data from *FETCH*

and *ROMEO* and IFREMER (IF), WHOI OAFlux (W).

	FETCH					ROMEO					
Q Term	IF	W	Q Term	IF	W	Q Term	IF	W	Q Term	IF	W
Q_{C_E}	0.6	-0.4	Q_{C_H}	0.1	-0.0	Q_{C_E}	1.7	-0.3	Q_{C_H}	0.4	-0.1
Q_{U_A}	6.6	-9.7	Q_{U_A}	1.9	-1.0	Q_{U_A}	26.8	-8.7	Q_{U_A}	3.0	-3.7
Q_{Q_S}	-1.4	6.6	Q_{T_S}	-0.6	-1.9	Q_{Q_S}	55.6	81.1	Q_{T_S}	31.7	29.5
Q_{Q_A}	-15.9	0.9	Q_{T_A}	7.7	1.5	Q_{Q_A}	-55.2	-14.8	Q_{T_A}	-48.5	-4.6
Q_{Total}	-10.1	-2.6	Q_{Total}	9.1	-1.4	Q_{Total}	28.9	57.3	Q_{Total}	-13.4	21.1
dL_E	-9.1	-3.5	dL_H	9.7	-0.5	dL_E	33.1	59.0	dL_H	-19.4	27.9

Table 3.5.   The average of the Q terms for FETCH and ROMEO observations vs.

IFREMER (IF) and WHOI OAFlux (W). Units W m^{-2}.

	15°N, 38°W						0°N,10°W					
Data	LH B	LH R	LH r	SH B	SH R	SH r	LH B	LH R	LH r	SH B	SH R	SH r
IF_1	24.3	34.0	0.9	18.6	24.9	0.4	11.8	21.4	0.7	-3.2	6.0	0.3
W	-3.2	20.4	0.9	5.0	6.4	0.5	7.2	15.2	0.8	0.9	2.2	0.7
IF_2	-4.1	26.8	0.8	6.0	7.4	0.2	-7.8	22.3	0.6	-1.1	4.0	-0.2

	0°N,23°W						*ROMEO* (36°N, 75°W)					
Data	LH B	LH R	LH r	SH B	SH R	SH r	LH B	LH R	LH r	SH B	SH R	SH r
IF_1	20.4	28.2	0.5	-0.1	4.0	0.4	21.9	89.8	0.8	-38.3	65.1	0.0
W	2.0	14.6	0.8	0.6	2.1	0.7	61.0	83.8	0.9	34.0	44.6	0.9
IF_2	0.2	20.7	0.4	0.2	3.6	-0.2	61.2	98.6	0.8	-20.1	44.7	0.8

Table 3.6.   Bias (B), RMSD (R) and r for comparison of weekly-averaged latent (LH) and sensible heat flux (SH) to IFREMER_1 (IF_1), WHOI OAFlux (W) and IFREMER_2 (IF_2; IFREMER_1 SST and 10 m wind speed and *Jackson et al.* 10 m specific air humidity and air temperature) estimates at three *PIRATA* buoy locations, 15°N, 38°W (1/26/98-12/26/05, 136 values), 0°N,10°W (9/15/97-12/26/05, 63 values) and 0°N, 23°W (3/1/99-12/26/05, 148 values) , and at the *ROMEO* buoy location (36°N, 75°W, 10/22/99-11/30/99, 14 values). Units W m^{-2}.
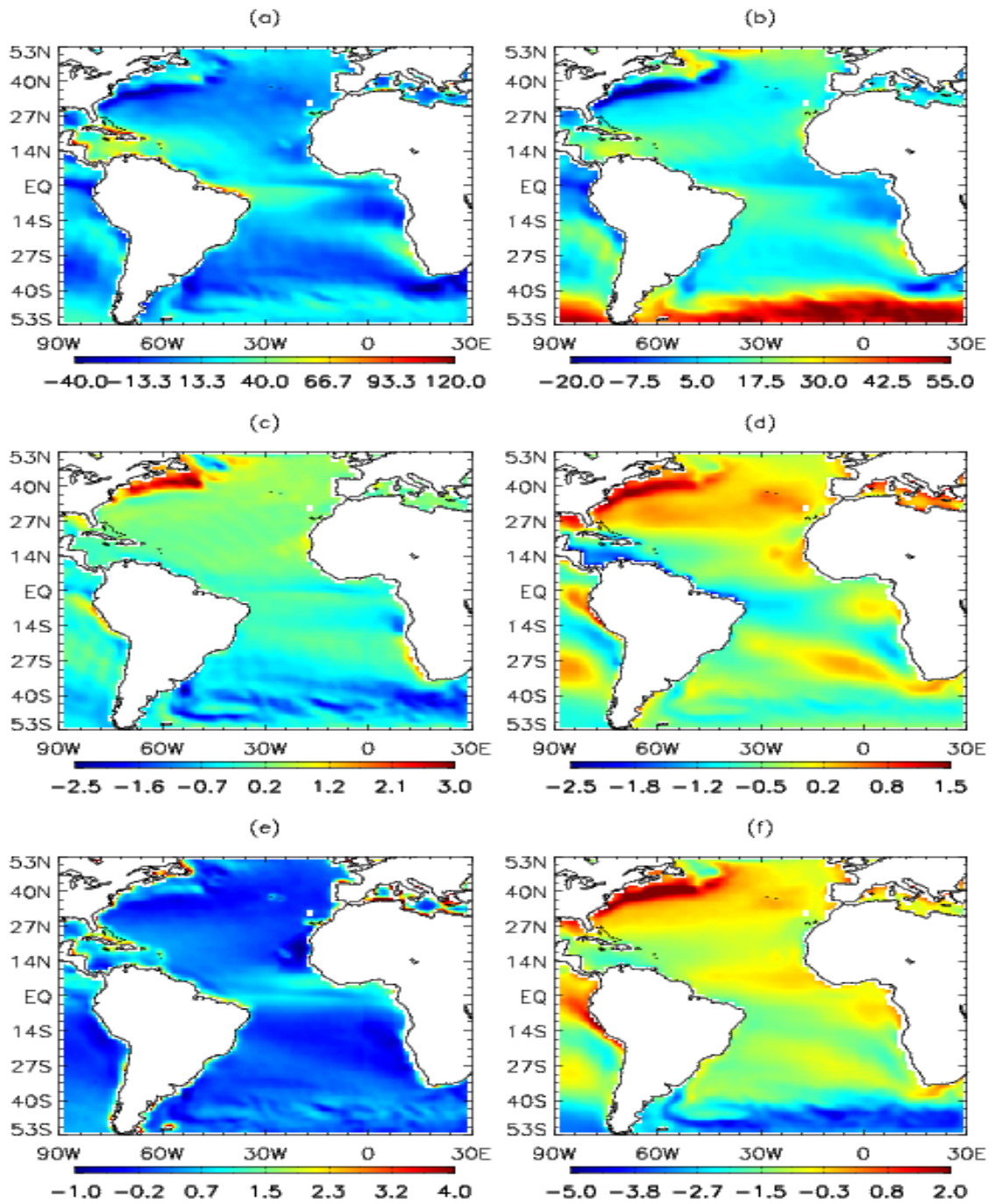
Figure 3.1.   The 1996-2005 annual-mean difference IFREMER minus WHOI OAFlux

for (a) latent heat flux, (b) sensible heat flux, (c) SST, (d) specific air humidity, (e)

surface wind speed and (f) air temperature. Units are W m^{-2} for latent and sensible heat

flux, °C for sea surface and air temperature, g kg^{-1} for specific air humidity and m s^{-1} for
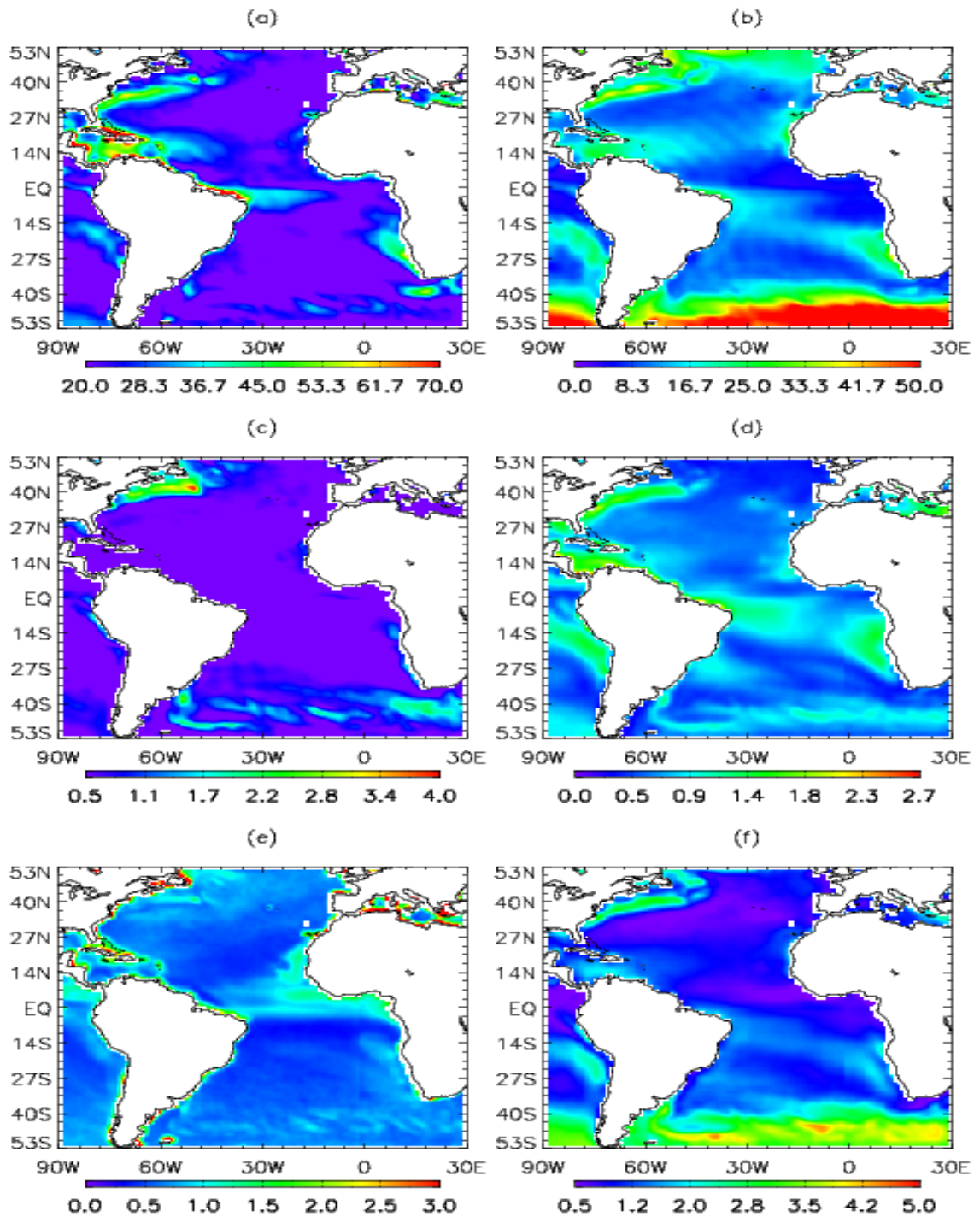
surface wind speed.

Figure 3.2.   The 1996-2005 annual RMSD between IFREMER and WHOI OAFlux for

(a) latent heat flux, (b) sensible heat flux, (c) SST, (d) specific air humidity, (e) surface

wind speed and (f) air temperature. Units W m^{-2} for fluxes, °C for sea surface and air

temperature, g kg^{-1} for specific air humidity and m s^{-1} for surface wind speed.
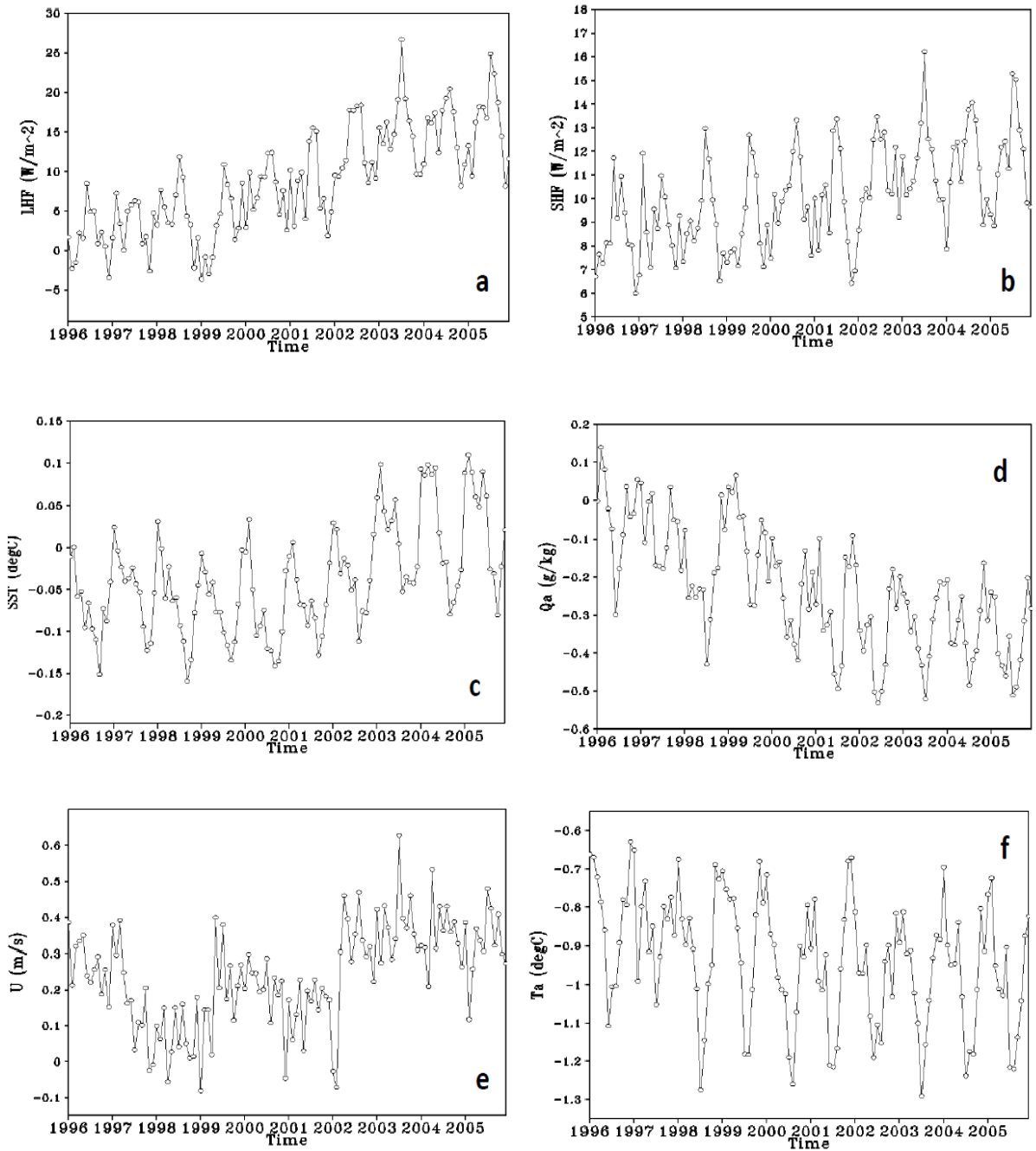
Figure 3.3.   Time series of IFREMER minus WHOI OAFlux monthly data averaged over the Atlantic basin (70°W-30°E, 45°S-45°N) for (a) latent heat flux, (b) sensible heat flux, (c) sea surface temperature, (d) specific air humidity, (e) surface wind speed and (f) air temperature during 1996-2005.
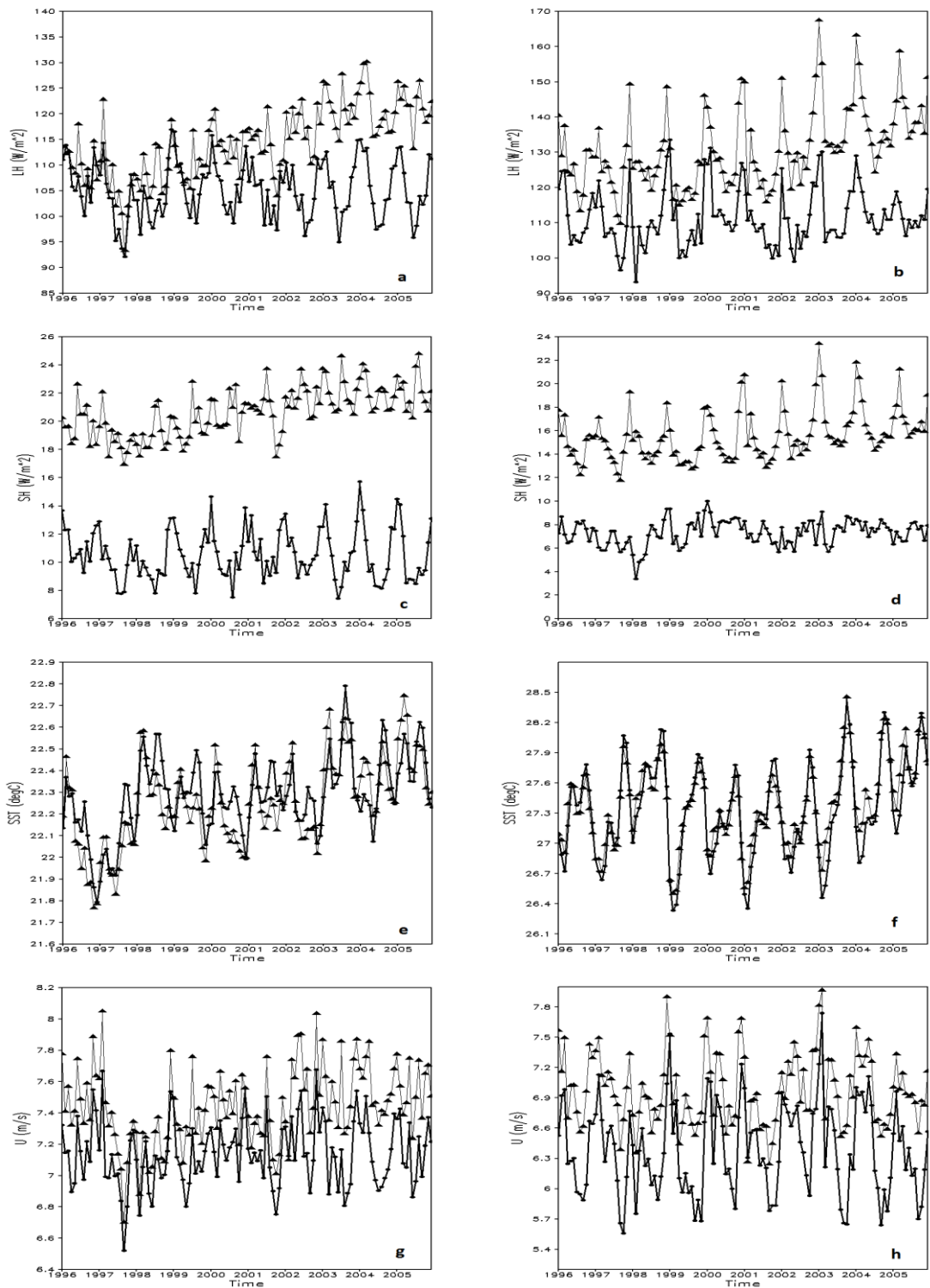
Figure 3.4. Time series of 1996-2005 monthly values for IFREMER (closed triangles) and WHOI OAFlux (closed circles, bolded line) averaged over the Atlantic basin (a, c, e, g) and over the 0°N-15°N zonal belt (b, d, f, h) for (a, b) latent heat flux (LH), (c, d) sensible heat flux (SH), (e, f) SST and (g, h) surface wind speed (U).
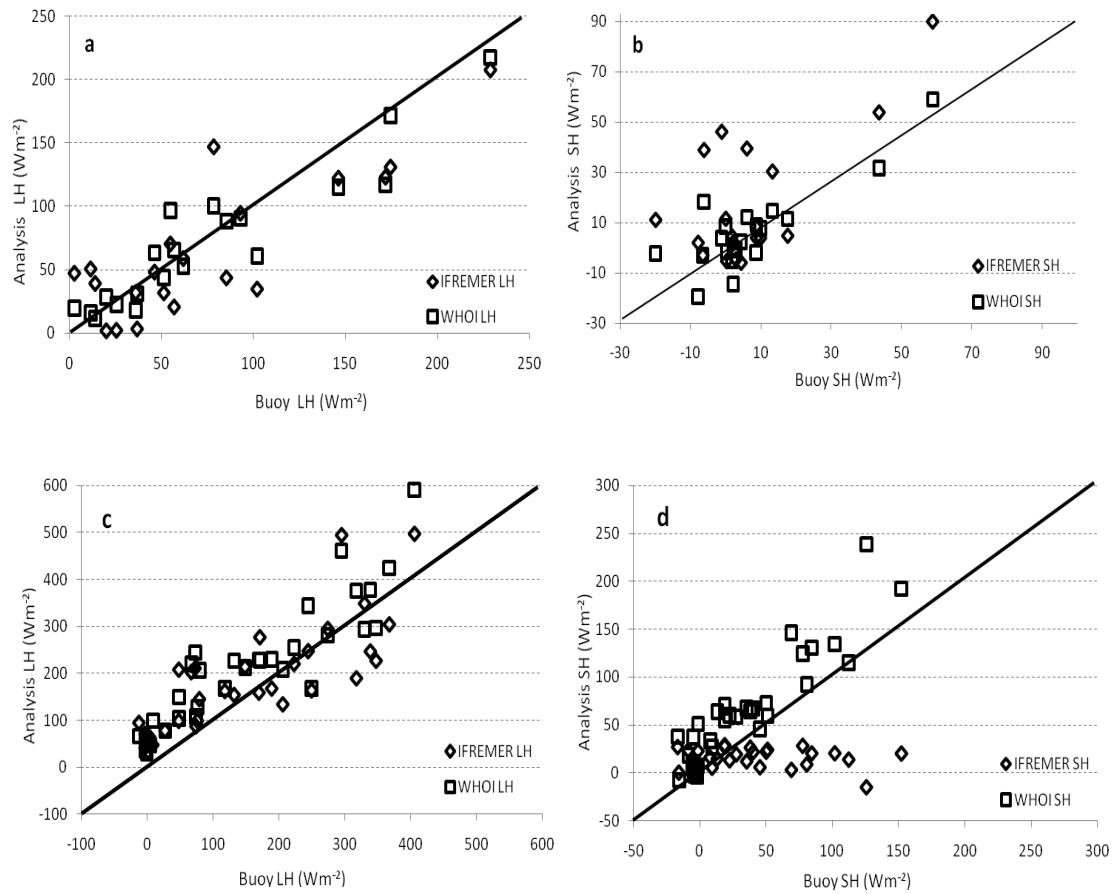
Figure 3.5.   Scatterplots of daily WHOI OAFlux and IFREMER latent heat (LH) and

sensible heat (SH) flux values vs. (a, b) *FETCH* buoy (42° 58' 56''N, 4°15' 11''E,

3/12/98-4/16/98, 20 values) and (c, d) *ROMEO* buoy (36°N, 75°W, 10/22/99-11/30/99,

35 values).
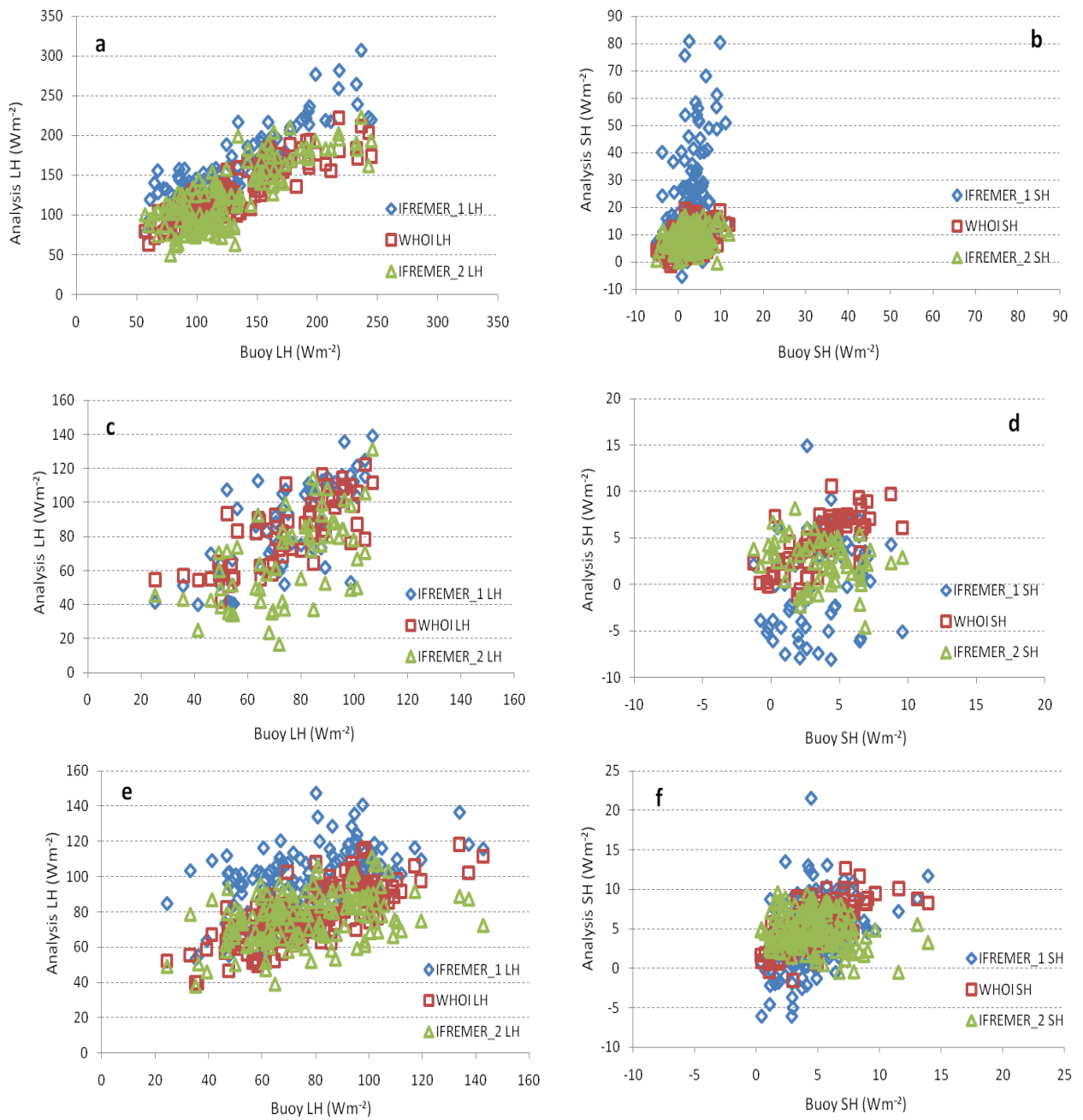
Figure 3.6.   Comparison of weekly-averaged buoy latent (LH) and sensible heat flux

(SH) to IFREMER_1, WHOI OAFlux and IFREMER_2 (IFREMER_1 SST and 10 m

wind speed and *Jackson et al.* 10 m specific air humidity and air temperature) estimates

at three *PIRATA* buoy locations: (a, b) 15°N, 38°W (1/26/98-12/26/05, 136 values), (c, d)

0°N,10°W (9/15/97-12/26/05, 63 values) and (e, f) 0°N, 23°W (3/1/99-12/26/05, 148 values).
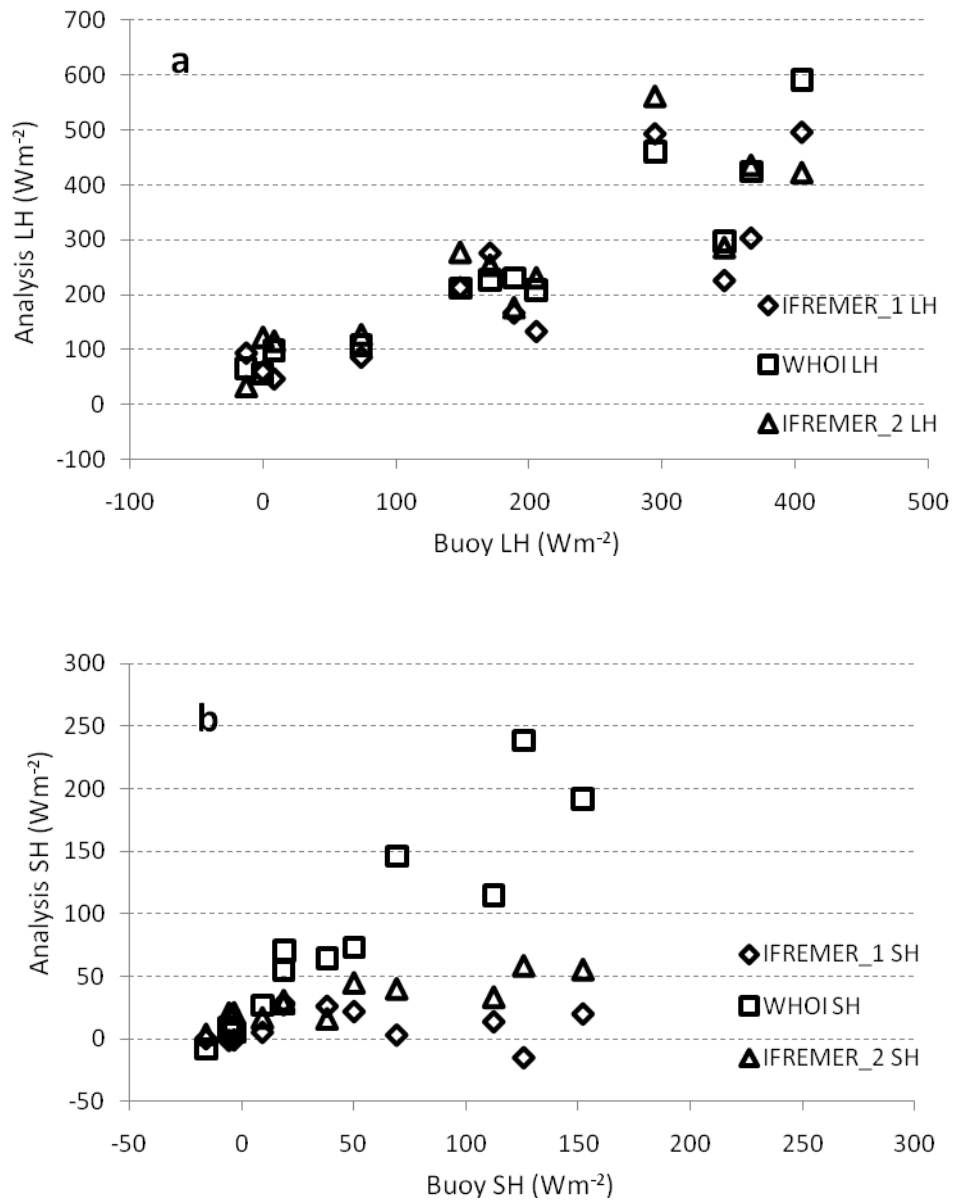
Figure 3.7.   Comparison of daily-averaged (a) buoy latent (LH) and (b) sensible heat

flux (SH) to IFREMER_1, WHOI OAFlux and IFREMER_2 (IFREMER_1 SST and 10

m wind speed and *Jackson et al.* 10 m specific air humidity and air temperature)

estimates at the *ROMEO* buoy location (36°N, 75°W, 10/22/99-11/30/99, 14 values).

Chapter 4: Processes maintaining subtropical salty pools

4.1 Introduction

As discussed in Chapters 1 and 3, latent heat flux from the ocean to the atmosphere affects climate variations on different spatial and temporal scales impacts the global water cycle. Surface freshwater flux, which is the difference between evaporation (recall that this is proportional to latent heat flux) and precipitation, is the key metric in the global moisture balance. We focus on subtropical ocean basins, which generally have desert-like conditions where evaporation is high, and rainfall and biological productivity are low, resulting in high surface salinity (SSS) (Gordon and Giulivi, 2008). Previous studies in these regions suggest that water lost through evaporation is replaced by poleward near-surface transport of fresher water from the tropics and equatorward transport of saltier water at the depth of the subsurface salinity maximum (e.g. Bryan and Oort, 1984; Levitus, 1986; Delcroix and Henin, 1991; Mignot et al., 2007, and Nyadjro et al., 2010). This explains why the high salinity surface salty pools which characterize the subtropics (Figure 4.1a) are ~10° poleward of the zones of high net evaporation.

The modern history of research on the ocean's hydrologic cycle begins with Wust (1938), whose work was summarized in <u>The Oceans</u> (Sverdrup et al., 1942). Among his observations was the striking similarity between the latitudinal distribution of time mean surface freshwater flux and surface salinity. Wust also went on to consider time-dependent changes in surface salinity, and in particular the seasonal cycle. He explored how annual variations in surface freshwater flux due to annual variations in evaporation associated with shifts in the atmospheric high sea level pressure systems lead to annual

variations in sea surface salinity. The subject attracted little attention for many years following this early work due to the absence of ocean salinity measurements and errors in surface flux estimates. However, by the 1980s enough information had been collected to allow the study of the seasonal hydrologic budget. These studies emphasized the importance of time mean and seasonal changes in lateral advection in balancing surface flux (e.g., Levitus, 1986; Foltz et al., 2004; Foltz and McPhaden, 2008). Interestingly, though, some of these observational studies suggest that wind-driven transport is too weak to fully balance observed surface freshwater export (Johnson et al., 2002; Rao and Sivakumar, 2003).

Interest is expected to grow in the ocean's role in hydrologic processes as the amount of ocean surface and subsurface salinity data grows (for example, through new satellite measurements) and the accuracy of coupled climate models improves. This chapter revisits another aspect of surface latent heat loss through examination of which processes regulate the salinity of the subtropical salty pools. It is addressed through analysis of the salt budget of a high resolution global ocean simulation driven by climatological surface forcing.

4.2 Background and motivation

Averaged over time, SSS shows spatial variations span a range of 3-4 practical salinity units (psu). Low values of <34 psu are found in the eastern North Pacific, the islands of Austral-Asia and Bay of Bengal, and polar latitudes. The northern tropical Pacific and Atlantic both have reduced values of SSS due to excess precipitation and, in the case of the Atlantic, river discharge. In contrast, local maxima in SSS occur in the

subtropics of most ocean basins with values of SSS 1-2psu higher than their minimum

values in the tropics, ranging from a relatively low maximum of 35psu in the North

Pacific to in excess of 37psu in the salty subtropical North and South Atlantic and

Arabian Sea. Superimposed on this time mean pattern is a weak 0.1psu annual cycle

driven by weak seasonal precipitation (Levitus, 1986; Boyer and Levitus, 2002;

Bingham, 2010; Yu, 2011).

The spatial patterns of SSS partly reflect the spatial patterns of atmospheric

convection, latent heat loss, and thus net surface freshwater flux. Highly convective

zones of the tropics are characterized by high rates of freshwater input approaching 1 mm

dy^{-1} in the western tropical Pacific and eastern Indian Oceans. These zonally oriented

convective zones undergo seasonal shifts in latitude and intensity following seasonal

changes in solar declination. In contrast, the clear, hot and dry subsidence regions of the

subtropics are characterized by rates of net freshwater export in excess of 0.13 mm dy^{-1}.

Studies of the salt balance in the upper layers of the tropics and subtropics have

suggested that the contribution of horizontal transports of freshwater exceed vertical

transports, and have identified wind-driven meridional transport from the relatively fresh

tropics as a likely term balancing net surface freshwater export in areas of subtropical

salinity maxima (Bryan and Oort, 1984; Levitus, 1986; Delcroix and Henin, 1991;

Mignot et al., 2007, Schmitt et al., 2009; Nyadjro et al., 2010). A recent observational

attempt to evaluate this mechanism by Yu (2011) suggests that other factors may be

important as well. A factor not included in these studies is the possible contribution of

horizontal eddy transport, as evident from mooring time series (Foltz et al., 2004). Qu et

al. (2011) performed a study focused on North Atlantic SSS max in mixed layer using a

1°x1° global climate model. Ocean dynamics and surface forcing were considered equally important, and eddy and small-scale contributions weak but not negligible.

The development of satellite SSS monitoring technology opens up the possibility of using the oceans to track aspects of the atmospheric freshwater cycle, and in particular monitoring the salty pools of the subtropics to track surface latent heat loss (Lagerloef et al., 2008). In addition to this revolutionary observational study, high-resolution ocean modeling studies are important in exploring this issue, and this chapter of the dissertation is focused on one such study. In section 4.2, the data, model and methods used in the study are discussed. Section 4.3 includes selected results of an eddy-resolving numerical simulation to quantify the possible contribution of advective and diffusive processes to the salt balance in the upper 100m of the subtropical oceans on different spatial and temporal scales. Section 4.4 has a summary of the study.

4.3 Data and methods

Applying the methodology of Stevenson and Niiler (1983) and Moisan and Niiler (1998), the budget for salinity for an ocean layer of fixed depth H can be expressed as

$$\int_{-H}^{0} \frac{\partial S}{\partial t} dz = - \int_{-H}^{0} \nabla \cdot \overrightarrow{US} \, dz + (E-P) \, S_o - K \left. \frac{\partial S}{\partial z} \right|_{z=-H} + \int_{-H}^{0} (HDiff) dz \qquad (4.1)$$

    A   B   C   D   E

where S represents salinity averaged over a given time interval, $\overrightarrow{US}$ is the three-dimensional transport of salt $[(US)\vec{\iota} + (VS)\vec{\jmath} + (WS)\vec{k}]$ where U, V and W are zonal,

106

meridional and vertical velocities, and K represents the vertical turbulent exchange coefficient. The lettered terms in (4.1) indicate: (A) tendency, or the rate of storage of salt over time, (B) salt advection expressed as salt transport convergence (under the assumption that the ocean is an incompressible fluid and that mass divergence is zero, or, mass is conserved; also note that the product of velocity and salt is averaged over time in this term) integrated over a depth of -H, (C) surface forcing, where E is evaporation, P is precipitation, and S_o is a reference surface salinity, (D) vertical salt diffusion at z=-H and (E) horizontal salt diffusion.

The general circulation ocean model that calculates these terms in the salinity budget uses Parallel Ocean Program V2 (POP V2) numerics in a fully global domain (Maltrud et al., 2010) at an eddy-resolving average 0.1^{o}x0.1^{o} horizontal. The horizontal grid is oriented along meridians in the Southern Hemisphere, but has a displaced tripole grid in the Northern Hemisphere with poles in Canada and Russia to resolve the Arctic Ocean. Thus, the grid differs increasingly from a Mercator coordinate system with increasing latitude. The model has 42 fixed vertical levels with ~10m resolution in the upper 250m, and partial bottom cells (for smoother resolution of bottom slopes). The model is volume-conserving and includes a nonlinear free surface in which the thickness of the topmost box responds to freshwater inputs such as precipitation and evaporation. Salinity changes solely as a consequence of dilution, and so the total globally integrated salt mass remains constant. Horizontal viscosity and diffusivity of tracers is biharmonic with a cubic dependence on local grid size. Along the equator the coefficients to viscosity and diffusivity reduce to $v_0 = 90$ m^4 s^{-1} and $\kappa_0 = 30$ m^4 s^{-1}. Vertical mixing uses a version of K-profile parameterization (KPP), where separate models for turbulence within the

ocean surface boundary layer and ocean interior are assumed, and the two models are coupled through continuity of turbulence diffusivities and their derivatives at the base of the boundary layer. Fairly large diffusion coefficients ($0.1 m^2 s^{-1}$) were chosen following Maltrud et al. (2010) to resolve gravitational instabilities.

Typical year surface fluxes are provided by the Large and Yeager (2009) surface flux climatology. Thermodynamic and long-wave heat fluxes, is calculated at each time step from bulk formulas, using interpolated 6-hourly atmospheric fields from National Centers for Environmental Prediction/National Center for Atmospheric Research reanalysis (Kalnay et al., 1996) and simulated SST. Monthly averaged insolation is derived from the International Satellite Cloud Climatology Project daily data (Bishop et al., 1997). A constant oceanic albedo of 7% is assumed. Precipitation is derived from a blend of microwave climatological values (Spencer, 1993) and merged observations (Xie and Arkin, 1998). There is no explicit runoff field. Instead, freshwater input is applied so as to relax surface salinity back to monthly climatological values from the World Ocean Atlas (Conkright et al., 1998) with a piston velocity such that the upper 20 m would relax back to the climatological values on a time scale of 30 days. An additional globally uniform freshwater input is applied to prevent large variations in the total ocean volume. This freshwater input is calculated so as to return the globally averaged ocean height back to zero, with a relaxation time of 30 days.

The model is integrated for a spin-up period of 63 years from zero motion initial conditions in which temperature and salinity are provided by the annual mean World Ocean Circulation Experiment Special Analysis Center climatological values (Gouretski and Jancke, 1996). A year of simulation requires 12,000 IBM Power6 PE hours. All key

terms in the salt budget (not normally saved) are accumulated every time-step and saved at 5-day intervals during the 64th, 65th and 66th years.

To illustrate the results we may expect from our model experiments we present results from a salt budget calculation using the POP model run for the tropical-subtropical Atlantic vertically averaged from the surface to H=100 m depth (Equation 4.1) averaged in time for the three sample years of the POP model run. We focus on 6 boxed regions where the model exhibits SSS maxima (Figure 4.2), including boxes in the North Atlantic (50°W-30°W, 19°N-29°N), South Atlantic (30°W-10°W, 20°S-10°S), North Pacific (178°E-162°E,20°N-30°N), South Pacific (135°W-115°W, 25°S-15°S) and South Indian Oceans (70°E-90°E, 32°S-22°S).

To evaluate the model results, we use daily observational data from 2008-2010 (three complete years) that is available at two buoys from the Prediction and Research Moored Array in the Atlantic (*PIRATA*) (Servain et al., 1998; see Chapter 3 for more details) located in the SSS maximum in the North Atlantic (20°N, 38°W and 21°N, 23°W). Salinity values are available at 1, 10, 20, 40, 60 and 120 m depth. In order to obtain 0-100 m vertically integrated salinity, there must be a complete record of the vertical profile of salinity at each time; to fill data gaps in the *PIRATA* time series, an average offset was calculated between each pair of successive vertical levels for all daily observations, and the offset was added or subtracted accordingly.

Similar to latent heat flux, evaporation is a function of several meteorological parameters, such as SST as well as air temperature, wind speed and humidity just above the ocean surface; buoy 3 m air temperature and specific air humidity, 4 m wind speed,

and sea surface temperature were inputs into the Coupled Ocean Atmosphere Research Experiment version 3.0 algorithm (COARE3.0) (Fairall et al., 2003) to obtain evaporation. For evaporation, gaps existed because of the lack of meteorological observations after June 2010; these were filled using an evaporation dataset provided by the Woods Hole Oceanographic Institution (WHOI; Yu et al., 2008). which has horizontal resolution of 1° x 1° and is available in daily time scale. Since rainfall observations by the *PIRATA* buoys were not of high quality (including negative values), observed precipitation was used from the Tropical Rainfall Measuring Mission (Huffman et al., 2007); this data has a horizontal resolution of 0.25°x0.25° and 3-hour temporal resolution. Surface freshwater forcing using observations was calculated by taking the difference between evaporation and precipitation, then multiplied by the same reference salinity (34.7 g kg^{-1}) as was used in the POP model.

4.4   Results

To evaluate model for balance of the salinity budget, three-dimensional advection, diffusion and total salt tendency (i.e. storage) must be calculated and then added together; this sum must be equal to surface freshwater forcing for balance to be achieved. Figure 4.3 displays the sum of those terms as well as surface forcing, and both are exactly equal.

In addition to checks within the model itself, model verification with observations must also be conducted. On a global scale, the three-year average of the model's surface freshwater flux (E-P) and SSS exhibits similar displacement of E-P off of SSS maxima as observations shown in Section 4.1 (Figure 4.1b). Note that, although the model and observations agree on displacement of SSS vs. E-P as well as the patterns of SSS, the

110

Atlantic appears to have lower modeled salinity compared to observations, with a much smaller area of ≥37 g kg^{-1} in the South Atlantic and no area with that much salinity in the North Atlantic. However, the South Pacific is saltier in the model, with a larger area between 36.5 and 37 g kg^{-1}.

As discussed in the previous section, correspondence between the model and observations was also tested at the *PIRATA* locations mentioned (Figure 4.4 and 4.5). For forcing, both the model and the observations show values over time with similar magnitudes of 1-2x10^{-7} cm g g^{-1} s^{-1} as well as greater seasonal variation in the model, with local minima in forcing during early spring and fall and maxima during winter and summer at 20°N, 38°W (Figures 4.4a-b). At 21°N, 23°W, the minima occur in spring and summer with maximum from October to January. At both buoy locations, 0-100 m vertically integrated salinity is within acceptable ranges when comparing the model to the observations, and both show significant intraseasonal variability, which can be attributed to eddies since timescales for eddies are mainly between 1-2 months.

The role of all model terms in the salinity budget is examined at each of the selected boxes shown in Figure 4.2, and the results of this analysis are plotted in Figure 4.6 (seasonal cycle) with area and time-mean averages of each term presented in Table 4.1. In all boxes, time and area-mean total advection (zonal plus meridional plus vertical) contributes the most to the surface forcing, while contributions by area and time-mean storage are three orders of magnitude smaller except in the North Pacific, where it is marginally larger (Table 4.1). However, storage has a distinct seasonal cycle and does contribute more to forcing during specific seasons (Figure 4.6). In the Atlantic and Pacific boxes, storage is positive in the summer months and negative in the winter

months in each respective hemisphere, which makes sense since changes in evaporation would follow these variations. While the amplitude of the maxima during the summer is $\sim 1 \times 10^{-7}$ cm g g^{-1} s^{-1}, winter maxima are much weaker. The South Indian Ocean box has weak local storage maxima in the summer and winter months. Time-mean diffusive processes, while still a very small contributor to time-mean forcing, are two orders of magnitude larger than storage in all regions except the South Indian Ocean box, where time-mean diffusion is -5×10^{-9} cm g g^{-1} s^{-1} (Table 4.1). The South Atlantic and Pacific boxes have larger magnitudes of time-mean diffusion than their northern counterparts ($\sim$-3 vs. $\sim$-1 $\times 10^{-8}$ cm g g^{-1} s^{-1}). In both the Atlantic and Pacific boxes in both hemispheres, maximum diffusion occurs in the winter months and is close to zero during the rest of the year. The South Indian Ocean box exhibits no distinct seasonal cycle of diffusion.

Since advection appears to be the most important term in the salinity budget in these regions, each individual component (zonal, meridional, and vertical) was estimated and calculated in the boxed regions (seasonal cycle in Figure 4.7, time and area mean in Table 4.1). In every boxed region, time-mean vertical advection is small and positive while horizontal advection (the sum of zonal and meridional components) is larger and negative (Table 4.1). Except for the South Pacific, both zonal and meridional advection terms are negative. Zonal advection is larger in magnitude in the North Atlantic and South Pacific boxed regions, while meridional advection is larger at the South Atlantic, North Pacific and South Indian SSS maxima.

Examining the seasonal cycle of advective components in each boxed region (Figure 4.7), negative zonal advection is dominant in the North Atlantic SSS maxima region during Spring (March-May). In the North Pacific Ocean box, horizontal

advection peaks during Summer (May-July). For February-October, zonal advection has the largest magnitude in the South Pacific. Overall, these results show that, in a time-mean sense, salt is upwelling in these regions and diverging away from the center of the maxima towards fresher waters to the north and south of the maxima, and there is some seasonality observed. This can help explain the poleward displacement of the subtropical SSS maxima, but eddy processes also need to be considered for further understanding of the displacement.

4.5 *Summary*

In this chapter, the roles of different processes that comprise the salinity budget in the subtropical salty pools were addressed through an examination of the POP V2 model output. It was found that the model compares reasonably well to observations at the regions of maximum sea surface salinity and surface freshwater flux, and the model maintains salinity balance globally. An examination of the salinity budget at six selected regions of maximum SSS revealed that time and area-mean total advection (zonal plus meridional plus vertical) is the dominant term, while diffusion and storage are much smaller but can be seasonally important in some of the regions analyzed. Finally, looking at advection by component in the regions, horizontal advection was largest and negative in all regions. Upwelling and divergence of salt can help explain the poleward displacement of SSS maxima from E-P maxima, but does not account for the possible influence of eddy processes.

	Surface Forcing	-dS/dt (Storage)	Total Diffusion	Total Advection	Zonal Advection	Meridional Advection	Vertical Advection
NA	-1.310	-0.009	-0.137	-1.164	-1.066	-0.406	0.308
SA	-1.829	-0.004	-0.316	-1.509	-0.702	-0.848	0.041
NP	-0.919	-0.033	-0.132	-0.754	-0.334	-0.792	0.372
SP	-1.352	0.004	-0.335	-1.021	-1.227	0.151	0.055
SI	-1.221	-0.013	-0.051	-1.157	-0.295	-0.975	0.113

Table 4.1.   Time mean budget terms in the upper 100m averaged over the five boxes:

North Atlantic (NA; 50°W-30°W, 19°N-29°N), South Atlantic (SA; 30°W-10°W, 20°S-

10°S), North Pacific (NP; 178°E-162°E,20°N-30°N), South Pacific (SP; 135°W-115°W,

25°S-15°S) and South Indian (SI; 70°E-90°E, 32°S-22°S) (units are 10^{-7} cm g g^{-1} s^{-1}).
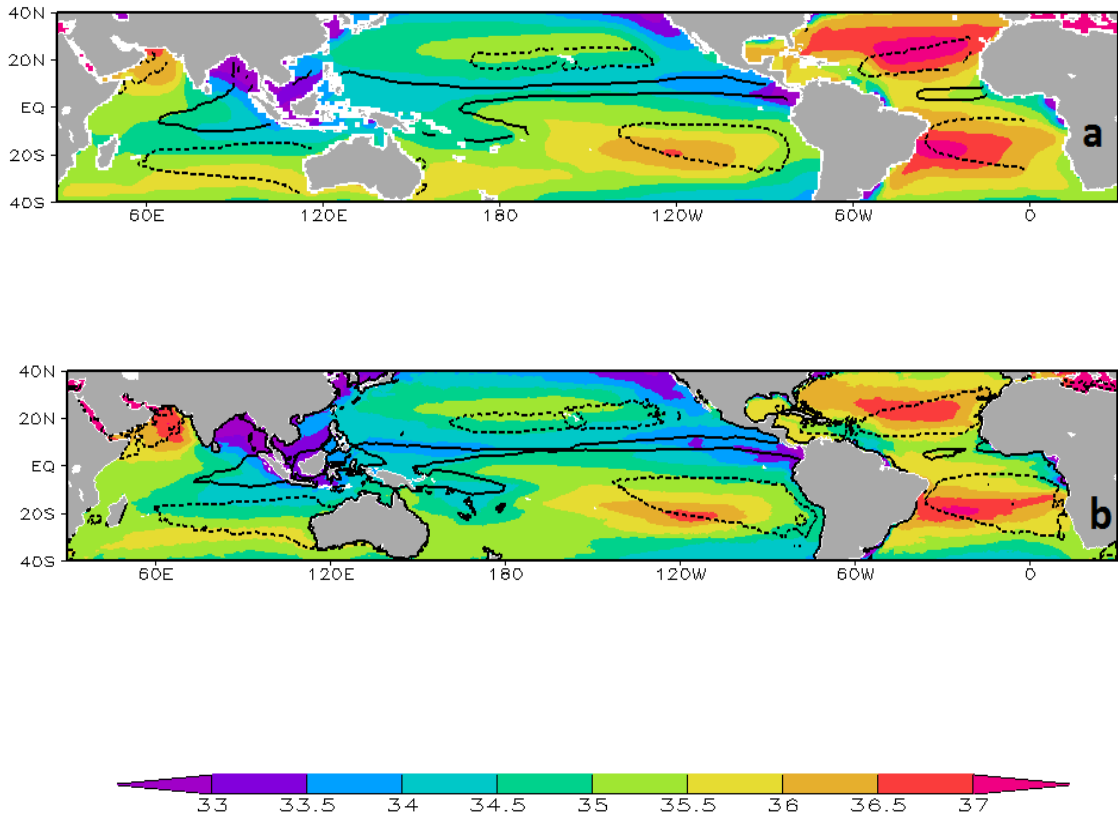
Figure 4.1.   (a) World Ocean Atlas 2009 (WOA09) climatological mean sea surface salinity. Contours of 1979-2009 climatological mean net surface freshwater flux (evaporation from the Woods Hole Oceanographic Institution minus precipitation from the Climate Prediction Center Merged Analysis of Precipitation (CMAP) are superimposed. (b) Three-year average SSS from a run of the Parallel Ocean Program Version 2 (POP V2) model. Contours of model net surface freshwater flux are superimposed. Units for SSS are g kg^{-1}, and, for freshwater flux, mm dy^{-1}. Contour intervals in both panels are ± 3 mm dy^{-1}, and a solid contour indicates flux into the ocean, but a dotted contour indicates flux out of the ocean.
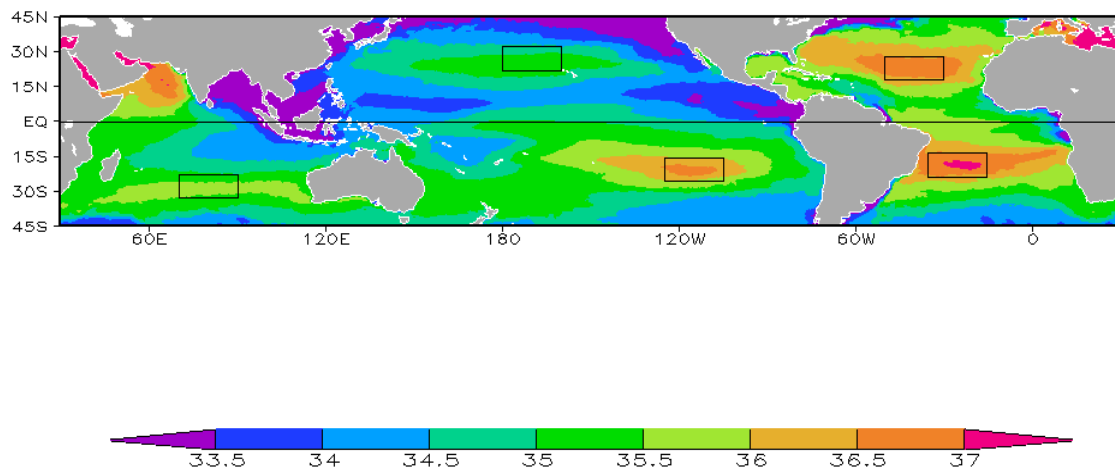
Figure 4.2.   Three-year average SSS from a run of the Parallel Ocean Program Version 2 (POP V2) model (units are g kg^{-1}). The rectangles indicate the selected regions used for the examination of salinity balance: North Atlantic (50°W-30°W, 19°N-29°N), South Atlantic (30°W-10°W, 20°S-10°S), North Pacific (178°E-162°E,20°N-30°N), South Pacific (135°W-115°W, 25°S-15°S) and South Indian (70°E-90°E, 32°S-22°S).
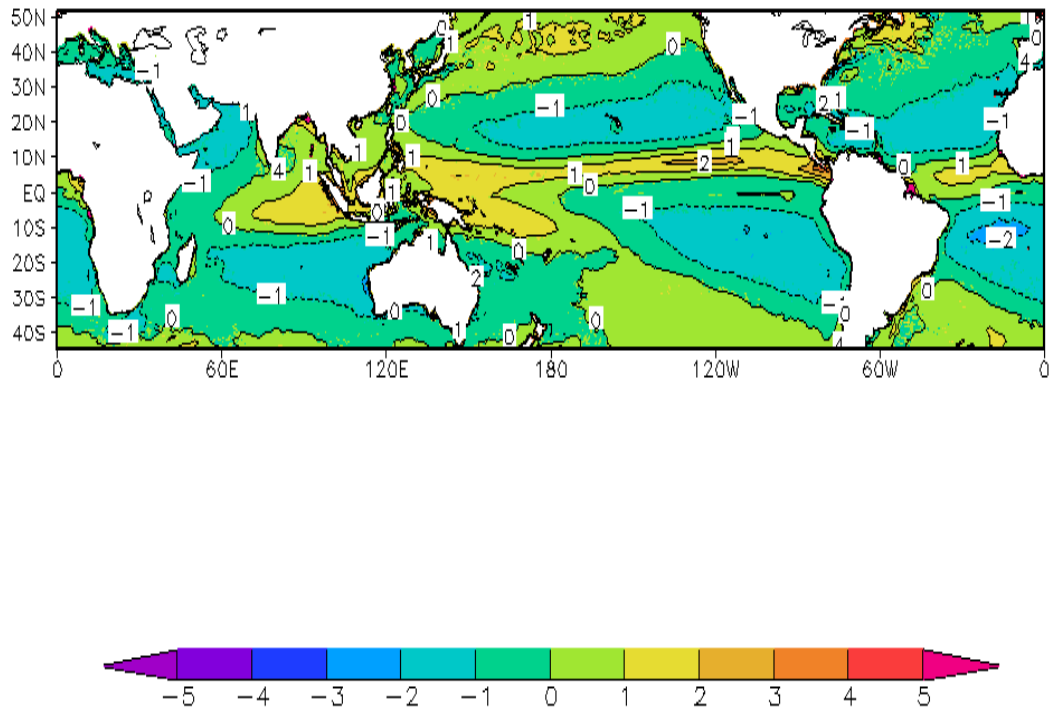
Figure 4.3.   Three-year average of the sum of advection, diffusion and salt storage in the 0-100m layer of the global ocean from the 0064-0066 run of the POP model (shaded) and surface freshwater forcing (E-P multiplied by a reference salinity of 34.7 g kg^{-1}, contoured) (units are 10^{-7} cm g g^{-1} s^{-1}).
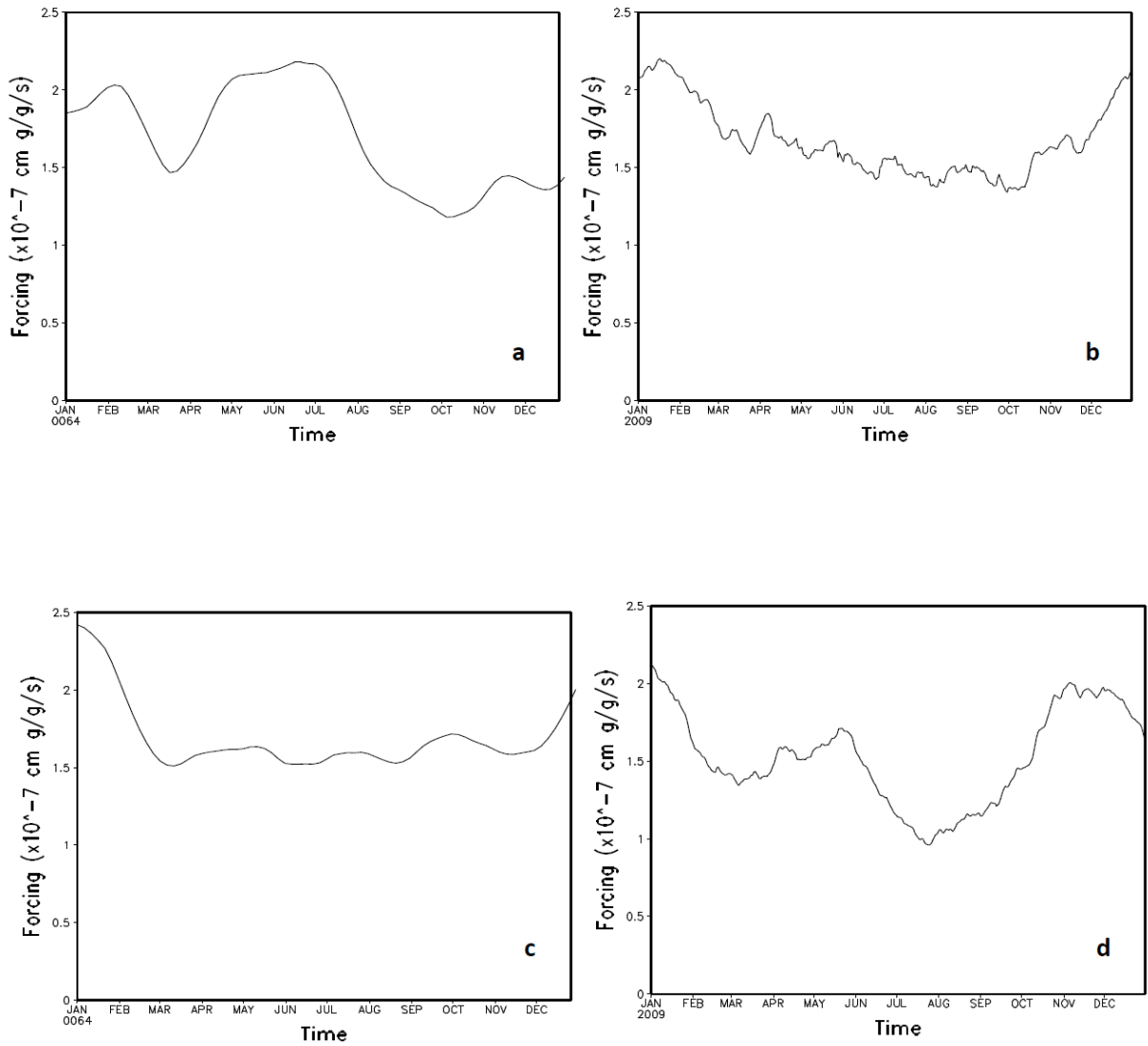
Figure 4.4. Seasonal cycle of surface freshwater forcing at (a,b) 20°N, 38°W and (c,d) 21°N, 23°W using (a,c) years 0064-0066 of the POP model run and (b,d) PIRATA/WHOI evaporation and TRMM precipitation for 2008-2010 (units are 10^{-7} cm g g^{-1} s^{-1}).
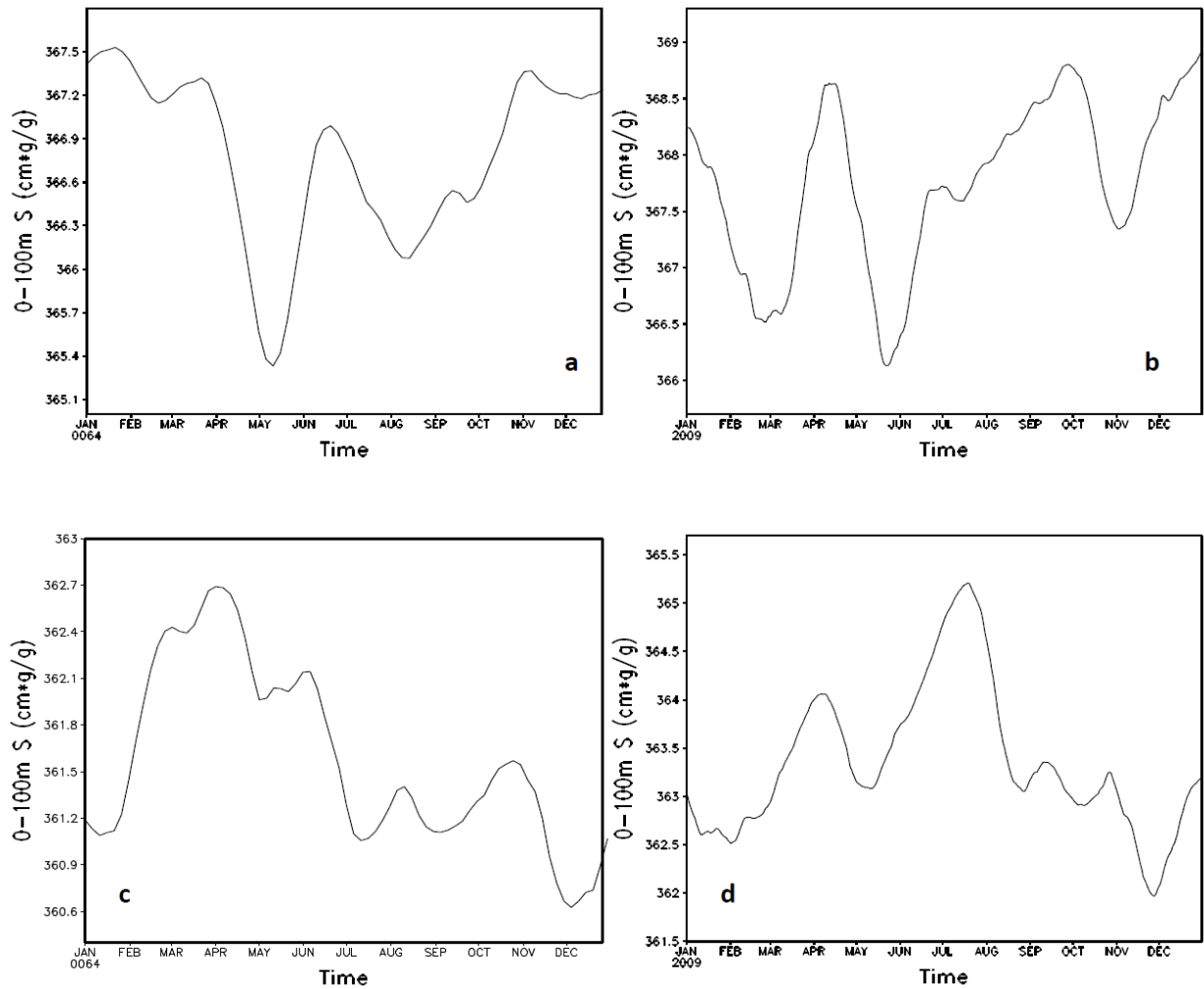
Figure 4.5. Seasonal cycle of 0-100m vertically integrated salinity at (a,b) 20°N, 38°W and (c,d) 21°N, 23°W using (a,c) years 0064-0066 of the POP model run and (b,d) PIRATA salinity for 2008-2010 (units are cm g g^{-1}).

BOX-AVERAGE BUDGETS (0-100m)

SURFACE FORCING (10^-7 CM*G/G/S)
— STORAGE
TOTAL ADVECTION
TOTAL DIFFUSION

120
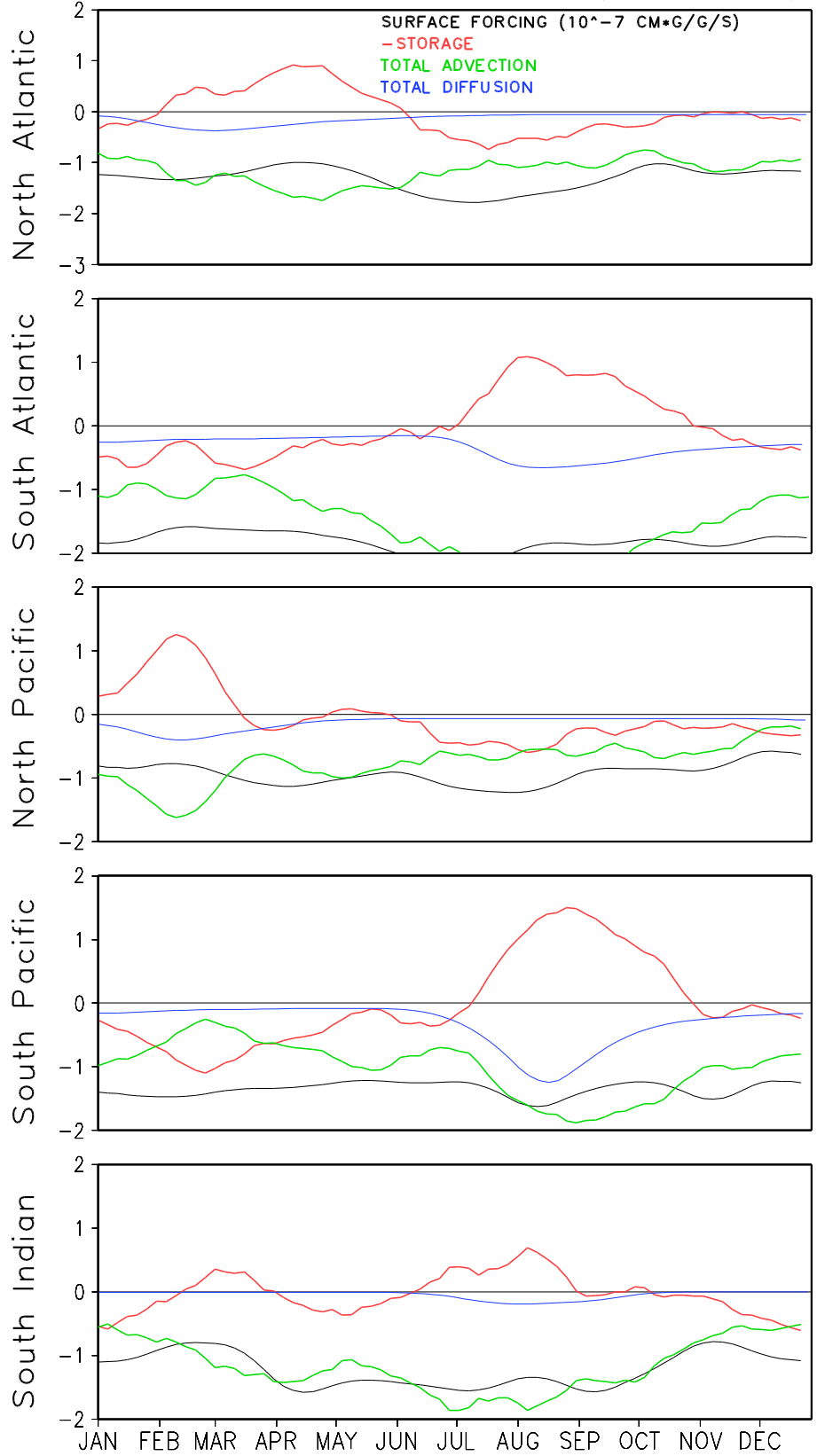
Figure 4.6.   Seasonal cycle of 0-100m salinity budget terms over the three years of the POP model run for each of the boxed regions cited in Figure 4.2: North Atlantic (50°W-30°W, 19°N-29°N), South Atlantic (30°W-10°W, 20°S-10°S), North Pacific (178°E-162°E,20°N-30°N), South Pacific (135°W-115°W, 25°S-15°S) and South Indian (70°E-90°E, 32°S-22°S) (units are 10^{-7} cm g g^{-1} s^{-1}).
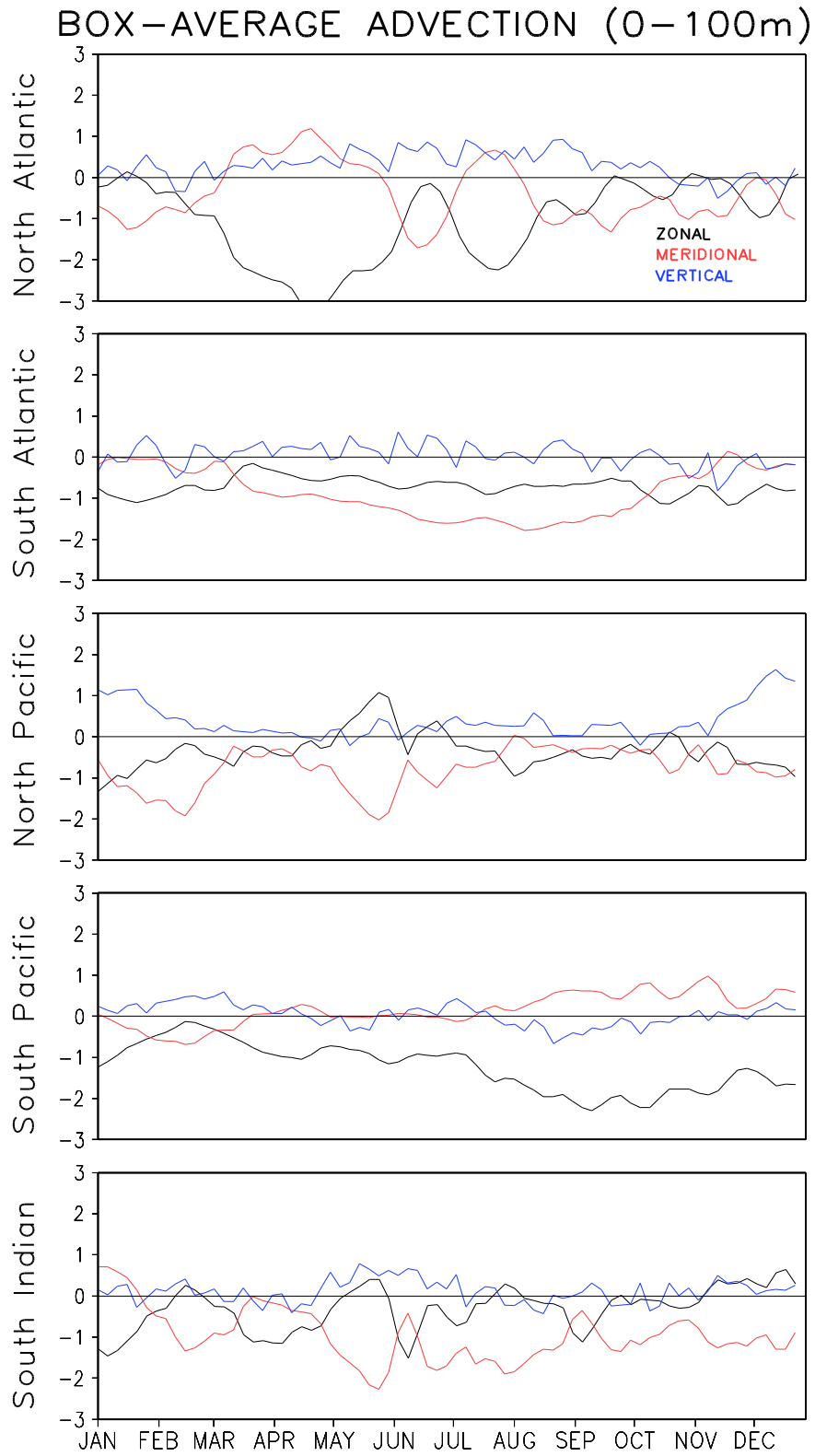
Figure 4.7.   Seasonal cycle of 0-100m total salt advection terms (divergence of salt fluxes in the zonal, meridional and vertical directions) over the three years of the POP model run for each of the boxed regions cited (units are 10^{-7} cm g g^{-1} s^{-1}).

Chapter 5: Conclusions

This dissertation contributes to the understanding of some mechanisms of surface heat and freshwater budgets over the global ocean. Chapter 2 focused on decadal trends as well as spatial and temporal variability of ocean heat content, which is used to determine heat storage by applying a time derivative, through an intercomparison of nine analyses. In Chapter 3, uncertainties of turbulent heat fluxes along with their respective parameters (sea surface and air temperature, wind speed, and specific humidity were determined through the comparison of two flux datasets, and improvement of one of the flux estimates was attempted by using new satellite atmospheric specific humidity and air temperature data. In Chapter 4, processes regulating the seasonal and intraseasonal contribution of different processes to the salinity budget in the upper 100m of the subtropical oceans were examined using an eddy-resolving general circulation ocean-only model.

In Chapter 2, nine analyses of heat content (two non-model, seven derived from data assimilation) were compared to examine decadal trends and variability both spatially and temporally, and three explanations for global heat content variations were tested: (i) changing observation bias resulting from the evolution of the observing system, (ii) the contribution of heat content variations by individual ocean basins, and (iii) the result of volcanic aerosols injected into the stratosphere.

Although there were many similarities shown among analyses, many uncertainties surround these individual estimates because of inadequacies in the historical observation network and the instruments, the techniques used to construct gridded analyses, and even

the applicability of estimating a linear trend from the global data. By comparing the analyses to each other and to the historical observation set this study shed light on these uncertainties and the presence of natural climate variability and improved understanding of the utility of the analyses for decadal climate research. The results presented in Chapter 2 indicate that the sequential analyses of ocean heat content have scientifically interesting sub-seasonal variability in both hemispheres despite problems resulting from measurement bias, a problem that afflicts all current ocean analyses and has been further explored by Giese et al. (2011) using three correction models of temperature bias in the historical bathythermograph dataset combined with the SODA analysis procedure of Carton and Giese (2008).

However, in Chapter 2, continuing differences in representation of climate anomalies were found, particularly in regions of poor historical observation coverage like the Southern Hemisphere. Addressing the causes of these differences ultimately may require reconsideration of both surface meteorology and assimilation strategies in these areas. Work that have been done since this study was undertaken have used comparison of ocean heat content as a diagnostic tool to examine weaknesses in analyses based on data assimilation, such as the Climate Forecasting System Reanalysis (CFSR; Xue et al., 2010). Further improvements to the analysis of ocean temperature likely will also require consideration of salinity because of its contribution to the stability of the water column and thus future studies will need to consider both variables; Xue et al. (2010) stated that the subsurface temperature (below 500 m) in the Indian Ocean in the CFSR increased significantly around 2003 when Argo salinity data became available, showing how the two variables are related.

In Chapter 3, an examination of two estimates of annual means of latent and sensible heat fluxes during 1996-2005, from IFREMER and from WHOI OAFlux over the Atlantic basin (70°W-30°E, 45°S-45°N), showed that IFREMER fluxes were larger in most regions with the exception of some small areas off the West African coast, the Gulf Stream region and south of 30°S; this coincides with IFREMER's lower specific air humidity and air temperature values in almost all regions of the Atlantic with the same exceptions as stated above. When compared to the *FETCH* and *ROMEO* buoys, the Q term analysis showed that specific air humidity contributed the most to the total difference between IFREMER and buoy latent heat fluxes, and that the Q term corresponding to air temperature was the largest of the Q terms for IFREMER-buoy sensible heat fluxes. Other possible explanations include (i) the inability of satellites to account for certain meteorological and oceanographic conditions, (ii) coastal upwelling present off the West African coast and its impacts on stratificiation, and (iii) conditions in areas of strong surface currents and SST gradients.

Curry et al. (2004) state that a combination of satellite and reanalysis data currently yields the most accurate representation of air-sea fluxes, but WHOI OAFlux being dependent on numerical models to a larger extent may have limitations in certain specialized circumstances. For example, humidity data from radiosondes are known to exhibit dry and wet biases, which depend on the radiosondes' type and age as well as the conditions of the environment (Wang et al., 2002). Since radiosonde data are assimilated into numerical models, their biases can impact NWP model analyses and subsequent forecasts; Bock et al. (2007) showed that, for measurements of precipitable water vapor (PWV), which can be used to estimate humidity, over Africa (35°N-10°S), there were dry

biases of 12-14% in radiosonde data compared to Global Positioning System (GPS) data, which partially explain biases of up to 9% for ERA-40 PWV data and up to 14% for NCEP2 PWV data.

Use of satellite data to estimate turbulent air-sea heat fluxes could be considered optimal due to the global coverage and high resolution provided by satellites. Satellite-derived fluxes have been shown to be an improvement over NWP fluxes, especially in tropical regions (Yu et al., 2004; Mestas-Nuñez et al., 2006). In addition, Ayina et al. (2006) reported that the forcing of an ocean circulation model with satellite fluxes instead of NWP fluxes improves calculations of currents and SST compared to tropical buoy data. In the future, the inconsistency of calibration of certain SSM/I products as well as the change in how QuikSCAT winds were estimated after the implementation of a new geophysical model from the Jet Propulsion Laboratory in 2006 relating wind to backscatter will be considered. A careful and rigorous effort to address these concerns and comprehensively test new approaches and data sources is required in order to achieve the goal of an accuracy of 5 W m^{-2} set by the Global Energy and Water Cycle Experiment Radiation Panel and the United States Climate Variability and Predictability Committee (Curry et al., 2004). Continued effort will eventually ensure that such a dataset is produced which allows examination of climate phenomena and realistic studies on the net air-sea heat fluxes and the budgets of heat as well as salinity in the upper ocean.

In Chapter 4 of the dissertation, an analysis of a run of the POP V2 model allowed for the examination of the role of different processes that comprise the salinity budget in the subtropical areas of maximum SSS. It was found that the model compares reasonably well to observations at the regions of maximum sea surface salinity and surface

freshwater flux, and the model maintains salinity balance globally. An examination of the salinity budget at six selected regions of maximum SSS revealed that time and area-mean total advection (zonal plus meridional plus vertical) is the dominant term, while diffusion and storage are much smaller but can be seasonally important in some of the regions analyzed. Finally, looking at advection by component in the regions, horizontal advection was largest and positive in most regions, and upwelling and divergence of salt is important in the subtropical salinity pools.

These initial conclusions of advection playing a key role in regions of high SSS are similar to the findings of several previous studies (Levitus, 1986; Foltz et al., 2004; Foltz and McPhaden, 2008). There is still more work needed to further explore the contribution of eddies to subtropical ocean salinity. Since the POP model has eddy-resolving resolution, it should be feasible to address this, particularly with a focus on breaking down the advection term (B) in equation (4.1) into time-mean and eddy components through Reynolds averaging.

Although it was shown that the output from the model run did compare well to observations, both the model run and the observations have three years of data, so a longer time period would make an analysis of this nature more robust. Also, as noted, the model appears to give salinity values that are lower than observations in the Atlantic basin and is biased salty in the South Pacific. These differences need to be examined to determine any issues with the model physics or parameterizations selected for a given run.

Appendices

Bourras' (2006) Q Term Method

The bulk parameterizations of latent and sensible heat fluxes, L_E and L_H, (written as LHF and SHF in the main text)are given as

$$L_E = \rho L_V C_E U_A (Q_S - Q_A) \qquad (A1)$$

$$L_H = \rho C_p C_H U_A (T_S - T_A) \qquad (A2)$$

where ρ is air density, L_V is the latent heat of vaporization, C_p is the specific heat capacity of air at constant pressure, and Q_A, T_A and U_A are specific humidity, air temperature and wind speed at a specified height above the surface. Q_S and T_S are the specific humidity and temperature at the sea surface; Q_S is assumed to be 98% of the saturation humidity at the sea surface temperature. C_E and C_H are moisture and heat exchange coefficients. Differentiating (A1) and (A2) result in

$$dL_E = (\frac{\partial L_E}{\partial C_E})dC_E + (\frac{\partial L_E}{\partial U_A})dU_A + (\frac{\partial L_E}{\partial Q_A})dQ_A + (\frac{\partial L_E}{\partial Q_S})dQ_S \qquad (A3)$$

$$dL_H = (\frac{\partial L_H}{\partial C_H})dC_H + (\frac{\partial L_H}{\partial U_A})dU_A + (\frac{\partial L_H}{\partial T_A})dT_A + (\frac{\partial L_H}{\partial T_S})dT_S \qquad (A4)$$

where

$$\frac{\partial L_E}{\partial C_E} = \rho L_V U_A (Q_S - Q_A)$$

$$\frac{\partial L_E}{\partial U_A} = \rho L_V C_E (Q_S - Q_A)$$

$$\frac{\partial L_E}{\partial Q_S} = \rho L_V C_E U_A$$

$$\frac{\partial L_E}{\partial Q_A} = -\rho L_V C_E U_A$$

$$\frac{\partial L_H}{\partial C_H} = \rho C_p U_A (T_S - T_A) \qquad \text{(A5)}$$

$$\frac{\partial L_H}{\partial U_A} = \rho C_p C_H (T_S - T_A)$$

$$\frac{\partial L_H}{\partial T_S} = \rho C_p C_H U_A$$

$$\frac{\partial L_H}{\partial T_A} = -\rho C_p C_H U_A$$

and

$$dL_E = L_E(estimated) - L_E(buoy)$$
$$dC_E = C_E(estimated) - C_E(buoy)$$
$$dU_A = U_A(estimated) - U_A(buoy)$$
$$dQ_A = Q_A(estimated) - Q_A(buoy)$$
$$dQ_S = Q_S(estimated) - Q_S(buoy) \qquad \text{(A6)}$$

$$dL_H = L_H(estimated) - L_H(buoy)$$
$$dC_H = C_H(estimated) - C_H(buoy)$$
$$dT_A = T_A(estimated) - T_A(buoy)$$
$$dT_S = T_S(estimated) - T_S(buoy)$$

Combining (A2), (A3) and (A4), dL_E and dL_H can be rewritten as

$$dL_E = Q_{C_E} + Q_{U_A} + Q_{Q_A} + Q_{Q_S} = Q_{tot}$$

$$dL_H = Q_{C_H} + Q_{U_A} + Q_{T_A} + Q_{T_S} = Q_{tot}$$

(A7)

where the "Q terms" are the contributions to the deviation between estimated and buoy fluxes.

Bibliography

AchutaRao, K. M., and Coauthors, 2006: Simulated and observed variability in ocean temperature and heat content. *Proc. Natl. Acad. Sci. USA*, **104,** 10768–10773.

Alory, G., S. Wijffels, and G. Meyers, 2007: Observed temperature trends in the Indian Ocean over 1960–1999 and associated mechanisms. *Geophys. Res. Lett.*, **34**, L02606, doi:10.1029/2006GL028044.

Antonov, J. L., S. Levitus, and T. P. Boyer, 2005: Thermosteric sea level rise, 1955-2003. *Geophys. Res. Lett.*, **32**, L12602, doi: 10.1029/2005GL023112.

Ayina, L.-H., A. Bentamy, A. M. Mestas-Nuñez, and G. Madec, 2006: The impact of satellite winds and latent heat fluxes in a numerical simulation of the Tropical Pacific Ocean. *J. Climate*, **19**, 5889-5902.

Barnes, S. L., 1964: A technique for maximizing details in numerical weather map analysis. *J. Appl. Meteor.*, **3**, 396–409.

Beal, R. C., V. N. Kudryavtsev, D. R. Thompson, S. A. Grodsky, D. G. Tilley, V. A. Dulov, and H. C. Graber, 1997: The influence of the marine atmospheric boundary layer on ERS 1 synthetic aperture radar imagery of the Gulf Stream. *J. Geophys. Res*., **102**, 5799-5814.

Behringer, D. W., 2005: The global ocean data assimilation system (GODAS) at NCEP. Preprints, *11th Symp. on Integrated Observing and Assimilation Systems for the Atmosphere, Oceans, and Land Surface (IOAS-AOLS),* San Antonio, TX,

Amer. Meteor. Soc., 3.3. [Available online at http://ams.confex.com/ams/pdfp apers/119541.pdf]

Beljaars, A. C. M., 1995a: The impact of some aspects of the boundary layer scheme in the ECMWF model. *Proc. Seminar on Parameterization of Sub-Grid Scale Physical Processes*, Reading, United Kingdom, ECMWF.

Beljaars, A. C. M., 1995b: The parameterization of surface fluxes in large scale models under free convection. *Q. J. R. Meteorol. Soc.*, **121**, 255-270.

Beljaars, A., and P. Kallberg, 2001: Ocean fluxes in the ECMWF 40-year re-analysis (ERA40). Paper presented at the WCRP/SCOR Workshop on Intercomparison and Validation of Ocean-Atmosphere Flux Fields, Washington, D.C.

Bell, M. J., 2000: Assessment of the FOAM global data assimilation system for real-time operational ocean forecasting. *J. Mar. Syst.*, **25,** 1–22.

Bell, M. J., M. J. Martin, and N. K. Nichols, 2004: Assimilation of data into an ocean model with systematic errors near the equator. *Quart. J. Roy. Meteor. Soc.*, **130,** 853–871.

Bellucci, A., S. Masina, P. Di Pietro, and A. Navarra, 2007: Using temperature–salinity relations in a global ocean implementation of a multivariate data assimilation scheme. *Mon. Wea. Rev.*, **135,** 3785–3807.

Bentamy, A., P. Queffeulou, Y. Quilfen, and K. Katsaros, 1999: Ocean surface wind fields estimated from satellite active and passive microwave instruments. *IEEE Trans. Geosci. Remote Sens.*, **37**, 2469-2486.

Bentamy, A., K. B. Katsaros, A. M. Mestas-Nuñez, W. M. Drennan, E. B. Forde and H. Roquet, 2003: Satellite estimates of wind speed and latent heat flux over the global oceans. *J. Climate*, **16**, 637-656.

Bentamy, A., L-H. Ayina, W. Drennan, K. Katsaros, A. M. Mestas-Nuñez, and R. T. Pinker, 2008: 15 years of ocean surface momentum and heat fluxes from remotely sensed observations. *FLUXNEWS, 5*, World Climate Research Programme, Geneva, Switzerland, 14–16. (Available online at http://sail.msk.ru/newsletter/ fluxnews_5_final.pdf).

Berrisford, P., D. Dee, K. Fielding, M. Fuentes, P. Källberg, S. Kobayashi and S. Uppala 2009: The ERA-Interim archive, Version 1.0. *ERA Report Series,* European Centre for Medium Range Weather Forecasts, Shinfield Park, Reading, Berkshire RG2 9AX, United Kingdom.

Berry, D. I., and E. C. Kent, 2009: A new air-sea interaction gridded dataset from ICOADS with uncertainty estimates. *Bull. Am. Meteorol. Soc.*, **90**, 645-656.

Bingham, F. M., G. R. Foltz, and M. J. McPhaden, 2010: Seasonal cycles of surface layer salinity in the Pacific Ocean. *Ocean Sci.*, **6**, 775-787.

Bishop, J.K.B., W.B. Rossow, and E.G. Dutton, 1997: Surface solar irradiance from the International Satellite Cloud Climatology Project 1983-1991. *J. Geophys. Res.,* **102**(D6), 6883-6910.

Bock, O., M.-N. Bouin, A. Walpersdorf, J.-P. Lafore, S. Janicot, F. Guichard, and A. Agusti-Panareda, 2007: Comparison of ground-based GPS precipitable water

vapour to independent observations and numerical weather prediction model reanalyses over Africa. *Q. J. R. Meteorol. Soc.,* **133**, 2011-2027.

Bourras, D., L. Eymard, and W. T. Liu, 2002: A neural network to estimate the latent heat flux over oceans from satellite observations. *Int. J. Remote Sens.,* **23***,* 2405-2423.

Bourras, D., 2006: Comparison of five satellite-derived latent heat flux products to moored buoy data. *J. Climate*, **19**, 6291-6313.

Boyer, T.P., and S. Levitus, 2002: Harmonic analysis of climatological sea surface salinity. *J. Geophys. Res.*, **107**(C12), 8006, doi: 10.1029/2001JC000829.

Boyer, T. P., S. Levitus, J. I. Antonov, R. A. Locarnini, and H. E. Garcia, 2006: *World Ocean Database 2005*. NOAA Atlas NESDIS 60, 190 pp. and DVDs.

Bretherton, F. P., D. M. Burridge, J. Crease, F. W. Dobson, E. B. Kraus, and T. H. Vonder Haar, 1982: The CAGE Experiment: A Feasibility Study. WCP 22, WMO, 95 pp.

Brunke, M. A., X. Zeng, and S. Anderson, 2002: Uncertainties in sea surface turbulent flux algorithms and data sets. *J. Geophys. Res.*, **107**(C10), 3141, doi:10.1029/2001JC000992.

Brunke, M. A., C. W. Fairall, X. Zeng, L. Eymard, and J. A. Curry, 2003: Which bulk aerodynamic algorithms are least problematic in computing ocean surface turbulent fluxes? *J. Climate*, **12**, 619-635.

Bryan, F., and A. Oort, 1984: Seasonal variation of the global water balance based on aerological data. *J. Geophys. Res.*, **89**(D7), 11,717-11,730.

Carton, J. A., B. S. Giese, and S. A. Grodsky, 2005: Sea level rise and the warming of the oceans in the SODA ocean reanalysis. *J. Geophys. Res.*, **110**, C09006, doi:10.1029/2004JC002817.

Carton, J. A., and B. S. Giese, 2008: A reanalysis of ocean climate using Simple Ocean Data Assimilation (SODA). *Mon. Wea. Rev.*, **136,** 2999–3017.

Cavalieri, D. J., C. L. Parkinson, P. Gloersen, J. C. Comiso, and H. J. Zwally, 1999: Deriving long-term time series of sea ice cover from satellite passive-microwave multisensor data sets. *J. Geophys. Res.*, **104**(C7), 15,803–15,814, doi:10.1029/1999JC900081.

Cayan, D. R., 1992: Latent and sensible heat flux anomalies over the northern oceans: driving the sea surface temperature. *J. Phys. Oceanogr.*, **22**, 859-881.

Chang, H.-R., and R. L. Grossman, 1999: Evaluation of bulk surface flux algorithms for light wind conditions using data from the Coupled Ocean-Atmosphere Response Experiment (COARE). *Q. J. R. Meteorol. Soc.*, **125**, 1551-1588.

Chepurin, G. A., and J. A. Carton, 1999: Comparison of retrospective analyses of the global ocean heat content. *Dyn. Atmos. Ocean*, **29,** 119–145.

Chou, S.-H., 1993: A comparison of airborne eddy correlation and bulk aerodynamic methods for ocean-air turbulent fluxes during cold-air outbreaks. *Bound.-Layer Meteor.*, **64**, 75-100.

Chou, S.-H., R. Atlas, C.-L. Shie, and J. Ardizzone, 1995: Estimates of surface humidity and latent heat fluxes over oceans from SSMI data. *Mon. Weather Rev.,* **123***, 2405-2425.

Chou, S.-H., C.-L. Shie, R. M. Atlas, and J. Ardizzone, 1997: Air-sea fluxes retrieved from Special Sensor Microwave Imager data. *J. Geophys. Res,* **102**, 12,705-12,726.

Chou, S.-H., E. Nelkin, J. Ardizzone, R. M. Atlas, and C.-L. Shie, 2003: Surface turbulent heat and momentum fluxes over global oceans based on the Goddard Satellite Retrievals, Version 2 (GSSTF2). *J. Climate*, **16**, 3256-3273.

Chou, S.-H., E. Nelkin, J. Ardizzone, and R. M. Atlas, 2004: A comparison of latent heat fluxes over global oceans for four flux products. *J. Climate*, **17**, 3973-3989.

Church, J. A., N. J. White, and J. M. Arblaster, 2005: Significant decadal-scale impact of volcanic eruptions on sea level and ocean heat content. *Nature*, **438,** 74–77.

Cione, J. J., and E. W. Uhlhorn, 2003: Sea surface temperature variability in hurricanes: implications with respect to intensity change. *Mon. Weather Rev.*, **131**, 1783-1795.

Conkright, M., S. Levitus, T. O'Brien, T. Boyer, J. Antonov, and C. Stephens, 1998: World Ocean Atlas 1998 CD-ROM Data Set Documentation, Technical Report 15, NODC Internal Report, Silver Spring, MD, 16 pp.

Conkright, M. E., and Coauthors, 2002: *Introduction*. Vol. 1, *World Ocean Database 2001,* NOAA Atlas NESDIS 42, 160 pp.

Cooper, M., and K. Haines, 1996: Altimetric assimilation with water property conservation. *J. Geophys. Res.*, **101,** 1059–1077.

Cox, M. D., 1984: A primitive equation, 3-dimensional model of the ocean. Geophysical Fluid Dynamics Laboratory Ocean Group Tech. Rep. 1, 141 pp.

Cressman, G. P., 1959: An operational objective analysis system. *Mon. Wea. Rev.*, **87,** 367–374.

Curry, J. A., and Coauthors, 2004: SEAFLUX. *Bull. Am. Meteorol. Soc.*, **85**, 409-424.

da Silva, A., A. C. Young, S. Levitus, 1994: *Algorithms and Procedures,* Vol. 1, *Atlas of Surface Marine Data 1994.* NOAA Atlas NESDIS 6, U.S. Dep. Of Commer., Washington, D.C.

Davey, M., 2005: Enhanced ocean data assimilation and climate prediction. European Commission Framework 5 Project Final Rep., 79 pp.

Delcroix, T., and C. Henin, 1991: Seasonal and interannual variations of sea surface salinity in the tropical Pacific Ocean, *J. Geophys. Res.*, **96**, 22,135-22,150.

Delworth, T. L., V. Ramaswamy, and G. L. Stenchikov, 2005: The impact of aerosols on simulated ocean temperature and heat content in the 20th century. *Geophys. Res. Lett.*, **32**, L24709, doi:10.1029/2005GL024457.

Dickson, R. R., and Coauthors, 2000: The Arctic Ocean response to the North Atlantic oscillation. *J. Climate*, **13,** 2671–2696.

Douglas, B., 2001: Sea level change in the era of the recording tide gauge. *Sea Level Rise: History and Consequences*, *Int. Geophys. Ser.*, vol. 75, edited by B. Douglas, M. Kearney, and S. Leatherman, pp. 37-64, Elsevier, New York.

Drennan, W. M., H. C. Graber, D. Hauser, and C. Quentin, 2003: On the wave age dependence of wind stress over pure wind seas. *J. Geophys. Res.,* **108**(C3), 8062, doi:10.1029/2000JC000715.

Fairall, C. W., E. F. Bradley, D. P. Rogers, J. B. Edson, and G. S. Young, 1996: Bulk parameterization of air-sea fluxes for Tropical Ocean-Global Atmosphere Coupled-Ocean Atmosphere Response Experiment. *J. Geophys. Res.,* **101***, 3747-3764.

Fairall, C. W., E. F Bradley, J. E. Hare, A. A. Grachev, and J. B. Edson, 2003: Bulk parameterization of air-sea fluxes: updates and verification for the COARE3.0 algorithm. *J. Climate,* **16**, 571-591.

Fennig, K., S. Bakan, H. Grassl, C.-P. Klepp, and J. Schulz, 2006: Hamburg Ocean Atmosphere Parameters and Fluxes from Satellite Data–HOAPS II-monthly

mean. *Electronic publication,* World Data Center for Climate, doi:10.1594/WDCC/ HOAPS2_MONTHLY.

Foltz, G.R., S.A.Grodsky, J.A.Carton, and M.J.McPhaden, 2004: Seasonal salt budget of the northwestern tropical Atlantic Ocean along 38°W. *J. Geophys. Res*., **109**, C03052, doi:10.129/2003JC0021112004.

Foltz, G.R., and M.J. McPhaden, 2008: Seasonal mixed layer salinity balance of the tropical North Atlantic Ocean. *J. Geophys. Res.*, **113**, C02013, doi: 10.1029/2007JC004178.

Gebbie, G., 2007: Does eddy subduction matter in the northeast Atlantic Ocean? *J. Geophys. Res*., **112**, C06007, doi:1029/2006JC03568.

Gibson, J. K., P. Kallberg, S. Uppala, A. Hernandez, A. Nomura, and E. Serrano, 1997: ERA description: Part I. ECMWF Reanalysis Project Report Series, ECMWF, 72 pp.

Giese, B. S., G. A. Chepurin, J. A. Carton, T. P. Boyer, and H. F. Seidel, 2011: Impact of bathythermograph temperature bias models on an ocean reanalysis. *J. Climate*, **24**, 84-93.

Gordon, A.L. and C.F. Giulivi, 2008: Sea surface salinity trends over fifty years within the subtropical North Atlantic. *Oceanography*, **21**, 20-29.

Gouretski, V., and K. Jancke, 1996: A new hydrographic data set for the South Pacific: synthesis of WOCE and historical data, WHP SAC Technical Report No. 2, WOCE Report No. 143/96 [unpublished manuscript].

Gouretski, V., and K. P. Koltermann, 2007: How much is the ocean really warming? *Geophys. Res. Lett.*, **34.**L01610, doi:10.1029/2006GL027834.

Graber, H. C., E. A. Terray, M. A. Donelan, W. M. Drennan, J. C. Van Leer, and D. B. Peters, 2000: ASIS—A new air–sea interaction spar buoy: design and performance at sea. *J. Atmos. Oceanic Technol.*, **17**, 708-720.

Grassl, H., V. Jost, R. Kumar, J. Schulz, P. Bauer, and P. Schussel, 2000: The Hamburg Ocean-Atmosphere Parameters and Fluxes from Satellite Data (HOAPS): A climatological atlas of satellite-derived air-sea interaction parameters over the oceans, *Rep. 312*, Max-Planck Institute for Meteorology, Hamburg, Germany.

Gregory, J. M., H. T. Banks, P. A. Stott, J. A. Lowe, and M. D. Palmer, 2004: Simulated and observed decadal variability in ocean heat content. *Geophys. Res. Lett.*, **31**, L15312, doi:10.1029/2004GL020258.

Griffies, S. M., M. J. Harrison, R. C. Pacanowski, and A. Rosati, 2003: A technical guide to MOM4. GFDL Ocean Group Tech. Rep. 5, 265 pp.

Grodsky, S. A., and J. A. Carton, 2001: Intense surface currents in the Tropical Pacific during 1996-1998. *J. Geophys. Res.*, **106**, 16,673-16,684.

Grodsky, S. A., J. A. Carton, and R. Murtugudde, 2001: Anomalous surface currents in the tropical Indian Ocean. *Geophys. Res. Lett.*, **28**, 4207–4210.

Grodsky, S. A., A. Bentamy, J. A. Carton, and R. T. Pinker, 2009: Intraseasonal latent heat flux based on satellite observations. *J. Climate,* **22***,* 4539-4556.

Grotefendt, K., K. Logemann, D. Quadfasel, and S. Ronski, 1998: Is the Arctic Ocean warming? *J. Geophys. Res.*, **103,** 27679–27687.

Grumbine, R. W., 1996: Automated passive microwave sea ice concentration analysis at NCEP (Unpublished manuscript available from NCEP/NWS/NOAA, 5200 Auth Road, Camp Springs, MD, 20746, USA).

Gunn, J. T., and R. D. Muench, 2001: Observed changes in Arctic Ocean temperature structure over the past decade. *Geophys. Res. Lett.*, **28**, 1035–1038.

Hanawa, K., P. Rual, R. Bailey, A. Syc, and M. Szabados, 1995: A new depth-time equation for Sippican or TSK T-7, T-6 and T-4 expendable bathythermographs (XBT). *Deep Sea Res. I*, **42,** 1423–1451.

Hansen, J., and Coauthors, 2005: Efficacy of climate forcings. *J. Geophys. Res.*, **110**, D18104, doi:10.1029/2005JD005776.

Hauser, D., et al., 2003: The FETCH experiment: An overview. *J. Geophys. Res.,* **108**(C3), 8053, doi: 10.1029/2001JC001202.

Hines, K. M., D. H. Bromwich, and G. J. Marshall, 2000: Artificial surface pressure trends in the NCEP–NCAR reanalysis over the Southern Ocean and Antarctica. *J. Climate*, **13,** 3940–3952.

Hollingsworth, A., and P. Lonnberg, 1989: The verification of objective analyses—Diagnostics of analysis system performance. *Meteor. Atmos. Phys.*, **40,** 3–27.

Houghton, R. W., 1991: The relationship of sea surface temperature to thermocline

    depth at annual and interannual time scales in the tropical Atlantic ocean. *J.*

    Geophys. Res., **96**(C8), 15,173–15,185, doi:10.1029/91JC01442.

Ingleby, B., and M. Huddleston, 2007: Quality control of ocean temperature and

    salinity profiles—Historical and real-time data. *J. Mar. Syst.*, **65**, 158–175.

Ishii, M., M. Kimoto, K. Sakamoto, and S. I. Iwasaki, 2006: Steric sea level changes

    estimated from historical ocean subsurface temperature and salinity analyses. *J.*

    Oceanogr., **62**, 155–170.

Jackson, D. L., G. A. Wick, and J. J. Bates, 2006: Near-surface retrieval of air

    temperature and specific humidity using multisensory microwave satellite

    observations. *J. Geophys. Res.*, **111***, D10306, doi:10.1029/2005JD006431.

Jackson, D. L., G. A. Wick, and F. R. Robertson, 2009: Improved multisensor

    approach to satellite-retrieved near-surface specific humidity observations. *J.*

    Geophys. Res., **114**, D16303, doi:10.1029/2008JD011341.

Johnson, E. S., G. S. E. Lagerloef, J. T. Gunn, and F. Bonjean, 2002: Surface salinity

    advection in the tropical oceans compared with atmospheric freshwater forcing:

    A trial balance. *J. Geophys. Res.*, **107**, 8014, doi:10.1029/2001JC001122.

Jones, C., P. Peterson, and C. Gautier, 1999: A new method for deriving ocean surface

    specific humidity and air temperature: an artificial neural network approach. *J.*

    Applied Meteorol., **38**, 1229-1246.

Josey, S. A., 2001: A comparison of ECMWF, NCEP-NCAR AND SOC surface heat fluxes with moored buoy measurements in the subduction region of the Northeast Atlantic. *J. Climate*, **14**, 1780-1789.

Kalnay, E., and coauthors, 1996: The NCEP/NCAR 40-Year Reanalysis Project. *Bull. Am. Meteorol. Soc.,* **77**, 437-471.

Kalnay, E., 2003: *Atmospheric Modeling, Data Assimilation and Predictability*. Cambridge University Press, 341 pp. Kalnay, E., and Coauthors, 1996: The NCEP/NCAR 40-Year Reanalysis Project. *Bull. Amer. Meteor. Soc.*, **77,** 437–471.

Kanamitsu, M., W. Ebisuzaki, J. Woollen, S-K. Yang, J. J. Hnilo, M. Fiorino, and G. L. Potter, 2002: NCEP–DOE AMIP-II Reanalysis (R-2). *Bull. Amer. Meteor. Soc.*, **83,** 1631–1643.

Karl, D. and R. Lukas, 1996: The Hawaii Ocean Time-series program: Background, rationale and field implementation. *Deep-Sea Research II,* **43***,* 129-156.

Kistler, R., E. Kalnay, W. Collins, et al., 2001: The NCEP-NCAR 50-year reanalysis: Monthly means CD-ROM and documentation. *Bull. Am. Meteorol. Soc.*, **82**(2), 247-267.

Köhl, A., and D. Stammer, 2008: Decadal sea level changes in the 50-year GECCO ocean synthesis. *J. Climate*, **21,** 1876–1890.

Konda, M., N. Imasato, and A. Shibata: 1996: A new method to determine near-sea surface air temperature by using satellite data. *J. Geophys. Res.,* **101***,* 14,349-14,360.

Kubota, M., N. Iwasaka, S. Kizu, M. Kondo, and K. Kutsuwada: 2002: Japanese ocean flux data sets with use of remote sensing observations (J-OFURO). *J. Oceanogr.*, **58***,* 213-225.

Kubota, M., A. Kano, H. Muramatsu, and H. Tomita, 2003: Intercomparison of various surface latent heat flux fields. *J. Climate*, **16**, 670-678.

Lagerloef, G., F.R. Colomb, D. Le Vine, F. Wentz, S. Yueh, C. Ruf, J. Lilly, J. Gunn, Y. Chao, A. deCharon, G. Feldman, and C. Swift, 2008: The Aquarius/SAC-D Mission: Designed to Meet the Salinity Remote-Sensing Challenge. *Oceanography*, **21**, 68-81.

Large, W.G. and S.G. Yeager, 2009: The global climatology of an interannually varying air–sea flux data set. *Clim. Dyn,.* **33**,341–364, DOI 10.1007/s00382-008-0441-3.

Levitus, S., 1986: Annual cycle of salinity and salt storage in the world ocean. *J. Phys. Oceanogr.*, **16**, 322-343.

Levitus, S., J. I. Antonov, T. P. Boyer, and C. Stephens, 2000: Warming of the world ocean. *Science*, **287,** 2225–2229.

Levitus, S., J.L. Antonov, J. Wang, T.L. Delworth, K.W. Dixon, and A.J. Broccoli, 2001: Anthropogenic warming of Earth's climate system. *Science*, **292**, 267-270.

Levitus, S., J. Antonov, and T. Boyer, 2005: Warming of the world ocean, 1955–2003. *Geophys. Res. Lett.*, **32**, L02604, doi:10.1029/2004GL021592.

Levitus, S., J. I. Antonov, T. P. Boyer, R. A. Locarnini, H. E. Garcia, and A. V. Michonov, 2009: Global ocean heat content 1955-2008 in light of recently revealed instrumentation problems. *Geophys. Res. Lett*, **36**, L07608, doi: 10.1029/2008GL037155.

Lozier, M. S., S. Leadbetter, R. G. Williams, V. Roussenov, M. S. C. Reed, and N. J. Moore, 2008: The spatial pattern and mechanisms of heat content change in the North Atlantic. *Science*, **319,** 800–803.

Luo, J-J., and T. Yamagata, 2001: Long-term El Niño–Southern Oscillation (ENSO)-like variation with special emphasis on the South Pacific. *J. Geophys. Res.*, **106**, 22211–22228.

Madec, G., P. Delecluse, M. Imbard, and C. Levy, 1998: OPA8.1 ocean general circulation model reference manual. Institut Pierre Simon Laplace, Note 11, 91 pp.

Maltrud, M., F. Bryan, S. Peacock, 2010: Boundary impulse response functions in a century long eddying global ocean simulation. *Environ. Fluid. Mech*., 275-295.

Mantua, N. J., S. R. Hare, Y. Zhang, J. M. Wallace, and R. C. Francis, 1997: A Pacific interdecadal climate oscillation with impacts on salmon production. *Bull. Amer. Meteor. Soc.*, **78**, 1069–1079.

Marshall, J., A. Adcroft, C. Hill, L. Perelman, and C. Heisey, 1997: A finite volume, incompressible Navier-Stokes model for studies of the ocean on parallel computers. *J. Geophys. Res.*, **102,** 5753–5766.

McPhaden, M. J., A. J. Busalacchi, R. Cheney, J. R. Donguy, K. S. Gage, D. Halpern, M. Ji, P. Julian, G. Meyers, G. T. Mitchum, P. P. Niiler, J. Picaut, R. W. Reynolds, N. Smith, K. Takeuchi, 1998: The Tropical Ocean-Global Atmosphere (TOGA) observing system: A decade of progress. *J. Geophys. Res.,* **103**, 14,169-14,240.

McPhaden, M. J., Y. Kuroda, and V. S. N. Murty, 2006: Development of an Indian Ocean moored buoy array for climate studies. *CLIVAR Exchanges*, **11***(4)*, 3-5, International CLIVAR Office, Southampton, UK.

Mestas-Nuñez, A. M., and D. B. Enfield, 1999: Rotated global modes of non-ENSO sea surface temperature variability. *J. Climate,* **12***,* 2734-2746.

Mestas-Nuñez, A. M., A. Bentamy, and K. B. Katsaros, 2006: Seasonal and El Niño variability in weekly satellite evaporation over the global ocean during 1996-98. *J. Climate*, **19**, 2025-2035.

Mignot, J., C. de Boyer Montègut, A. Lazar, and S. Cravatte, 2007: Control of salinity on the mixed layer depth in the world ocean: 2. Tropical areas. *J. Geophys. Res.,* **112,** C10010, doi: 10.1029/2006JC003954.

Miller, A. J., and N. Schneider, 2000: Interdecadal climate regime dynamics in the North Pacific Ocean: Theories, observations and ecosystem impacts. *Prog. Oceanogr.*, **47,** 355–379.

Miller, A. J., D. R. Cayan, and W. B. White, 1998: A westward-intensified decadal change in the North Pacific thermocline and gyre-scale circulation. *J. Climate*, **11,** 3112–3127.

Moisan, J. R., and P. P. Niiler, 1998: The seasonal heat budget of the North Pacific: Net heat flux and heat storage rates (1950-1990), *J. Phys. Oceanogr.,* **28**, 401-421.

Moyer, K. A. and R. A. Weller, 1997: Observations of surface forcing from the subduction experiment: a comparison with global model products and climatological data sets. *J. Climate.*, **10**, 2725-2742.

Navarra, A., W. F. Stern, and K. Miyakoda, 1994: Reduction of the Gibbs oscillation in spectral model simulations. *J. Climate,* **7**, 1169-1183.

Niiler, P. P., and E. B. Kraus, 1977: One-dimensional models of the upper ocean. *Modelling and Prediction of the Upper Layers of the Ocean,* edited by E.B. Kraus, pp.143-172, Pergamon, Oxford, England, UK.

Nyadjro, E.S., B. Subrahmanyam, V.S.N. Murty, and J.F. Shriver, 2010: Salt transport in the near-surface layer in the monsoon-influenced Indian Ocean using HYCOM. *Geophys. Res. Lett., 37,* L15603, doi: 10.1029/2010GL044127.

Oost, W. A., G. J. Komen, C. M. J. Jacobsm, and C. van Oort, 2002: New evidence for a relation between wind stress and wave age from measurements during ASGAMAGE. *Bound.-Layer Meteorol.*, **103**, 409-438.

Peltier, W., 2001: Global glacial isostatic adjustment and modern instrumental records of relative sea level history. *Sea Level Rise: History and Consequences*, *Int. Geophys. Ser.*, vol. 75, edited by B. Douglas, M. Kearney, and S. Leatherman, pp. 37-64, Elsevier, New York.

Qu, T., S. Gao, and I. Fukumori, 2011: What governs the North Atlantic salinity maximum in a global GCM? *Geophys. Res. Lett.*, **38**, doi: 10.1029/2011GL046757.

Ramaswamy, V., and Coauthors, 2001: Radiative forcing of climate change. *Climate Change 2001: The Scientific Basis,* J. T. Houghton et al., Eds., Cambridge University Press, 347–416.

Rao, R. R., and R. Sivakumar, 2003: Seasonal variability of sea surface salinity and salt budget of the mixed layer of the north Indian Ocean, *J. Geophys. Res*., **108**, 3009, doi:10.1029/2001JC000907.

Read, J. F., and W. J. Gould, 1992: Cooling and freshening of the subpolar North Atlantic Ocean since the 1960s. *Nature*, **360,** 55–57. doi:10.1038/360055a0.

Reynolds, R. W., T. M. Smith, C. Liu, D. B. Chelton, K.S. Casey, M. G. Schlax, 2007: Daily high-resolution-blended analyses for sea surface temperature. *J. Climate*, **20**, 5473-5496.

Rossby, C., 1959: Current problems in meteorology. *The Atmosphere and Sea in Motion*, pp. 9-50, Rockefeller Inst. Press, New York.

Schlosser, C. A., and P. R. Houser, 2007: Assessing a satellite-era perspective of the global water cycle. *J. Climate*, **20**, 1316-1338.

Schmitt, R. W., 1995: The ocean component of the global water cycle: U.S. National Report to International Union of Geodesy and Geophysics, 1991-1994. *Reviews of Geophysics*, **33**(Supplement), 1395-1409.

Schmitt, R. W., T. Boyer, G. Lagerloef, J. Schanze, S. Wijffels, and L. Yu, 2008: Salinity and the Global Water Cycle, *Oceanography*, **21**, 12-19.

Schulz, J., P. Schlussel, and H. Grassl, 1993: Water vapor in the atmospheric boundary layer over oceans from SSM/I measurements. *Int. J. Remote Sens.,* **14***,* 2773-2789.

Schulz, J., J. Meywerk, S. Ewald, and P. Schlüssel, 1997: Evaluation of satellite-derived latent heat fluxes. *J. Climate,* **10***,* 2782-2795.

Servain, J., A. J. Busalacchi, M. J. McPhaden, A. D. Moura, G. Reverdin, M. Vianna, and S.E. Zebiak, 1998: A pilot research moored array in the tropical Atlantic (PIRATA). *Bull. Am. Meteorol. Soc.*, **79**(10), 2019-2031.

Shay, L. K., G. J. Goni, and P. G. Black, 2000: Effects of a warm oceanic feature on Hurricane Opal. *Mon. Weather Rev.*, **128**, 1366-1383.

Smith, S. D., 1988: Coefficients for sea surface wind stress, heat flux, and wind profiles as a function of wind speed and temperature. *J. Geophys. Res.*, **93**(C12), 15,467–15,472.

Smith, S. R., D. M. Legler, and K. V. Verzone, 2001: Quantifying uncertainties in NCEP reanalyses using high-quality research vessel observations. *J. Climate*, **14**, 4062-4072.

Smith, S. R., P. J. Hughes and M. A. Bourassa, 2010: A comparison of nine monthly air-sea flux products. *Int. J. Climatol*, published online in Wiley Online Library (wileyonlinelibrary.com) DOI: 10.1002/joc.2225.

Spencer, R.W., 1993: Global oceanic precipitation from the MSU during 1979-91 and comparisons to other climatologies. *J. Climate,* **6**, 1301-1326.

Stammer, D., K. Ueyoshi, A. Köhl, W. G. Large, S. A. Josey, and C. Wunsch, 2004: Estimating air-sea fluxes of heat, freshwater, and momentum through global ocean data assimilation. *J. Geophys. Res.*, **109.**C05023, doi:10.1029/2003JC002082.

Stevenson, J.W., and P.P. Niiler,1983: Upper ocean heat budget during the Hawaii-to-Tahiti shuttle experiment. *J. Phys. Oceanogr.*, **13**, 1894-1907, 1983.

Sun, C., M. M. Rienecker, A. Rosati, M. Harrison, A. Wittenberg, C. L. Keppenne, J. P. Jacob, and R. M. Kovach, 2007: Comparison and sensitivity of ODASI ocean analyses in the tropical Pacific. *Mon. Wea. Rev.*, **135,** 2242–2264.

Sverdrup, H., M.W. Fleming, and R.H. Johnson, 1942: <u>The Oceans Their Physics, Chemistry, and General Biology</u>, Prentice-Hall, Inc., New York.

Taylor, P. K., and M. A. Yelland, 2000: On the apparent "imbalance" term in the turbulent kinetic energy budget. *J. Atmos. Oceanic Technol.*, **17**, 82-89.

Thadathil, P., A. K. Saran, V. V. Gopalakrishna, P. Vethamony, N. Araligidad, and R. Bailey, 2002: XBT fall rate in waters of extreme temperature: A case study in the Antarctic Ocean. *J. Atmos. Oceanic Technol.*, **19**, 391–396.

Trenberth, K. E., L. Smith, T. Qian, A. Dai, and J. Fasullo, 2007: Estimates of the global water budget and its annual cycle using observational and model data. *J. Hydrometeorol.*, **8**, 758-769.

Uppala, S. M., and Coauthors, 2005: The ERA-40 re-analysis. *Quart. J. Roy. Meteor. Soc.*, **131,** 2961–3012. doi:10.1256/qj.04.176.

Vonder Haar, T. H., and A. H. Oort, 1973: New estimate of annual poleward energy transport by Northern Hemisphere oceans. *J. Phys. Oceanog.*, **3**, 169-172.

Wang, C., D. B. Enfield, S.-K. Lee, and C. W. Landsea, 2006: Influences of the Atlantic Warm Pool on Western Hemisphere summer rainfall and Atlantic hurricanes. *J. Climate,* **19***,* 3011-3028.

Wang, J., H. L. Cole, D. J. Carlson, E.R. Miller, K. Beierle, A. Paukkunen, and T.K. Laine, 2002: Corrections of humidity measurement errors from the Vaisala RS80 radiosonde-Application to TOGA COARE data. *J. Atmos. Oceanic Technol.,* **19***,* 981-1002.

Wentz, F. J., 1997: A well-calibrated ocean algorithm for SSM/I. *J. Geophys. Res*., **102**, 8703-8718.

White, W. B., M. D. Dettinger, and D. R. Cayan, 2003: Sources of global warming of the upper ocean on decadal period scales. *J. Geophys. Res.*, **108**, 3248, doi:10.1029/2002JC001396.

Wijffels, S. E., C. M. Domingues, P. Barker, N. J. White, A. Gronell, K. Ridgway, and J. A. Church, 2008: Changing expendable bathythermograph fall rates and their impact on estimates of thermosteric sea level rise. *J. Climate*, **21,** 5657–5672.

Willis, J. K., D. Roemmich, and B. Cornuelle, 2004: Interannual variability in upper ocean heat content, temperature, and thermosteric expansion on global scales. *J. Geophys. Res.*, **109**, C12036, doi:10.1029/2003JC002260.

Wilson, J. R., 1998: Global Temperature–Salinity Profile Programme (GTSPP)— Overview and future. IOC Tech. Series 49, 33 pp.

Woodruff, S. D., H. F. Diaz, J. D. Elms, and S. J. Worley, 1998: COADS release 2 data and metadata enhancements for improvements of marine surface flux fields. *Phys. Chem. Earth*, **23**, 517-526.

Worley, S. J., S. D. Woodruff, R. W. Reynolds, S. J. Lubker, and N. Lott, 2005: ICOADS release 2.1 data and products. *Int. J. Climatol.*, **25**, 823-842.

Wüst, G. ,1936: Surface salinity, evaporation and precipitation in the oceans. Festschrift Norbert Krebs (Länderkundliche Research), p. 347-59. Stuttgart.

Xie, P., and P. A. Arkin, 1996: Global monthly precipitation estimates from satellite-observed outgoing longwave radiation. *J. Climate,* **11**, 137-164.

Xue, Y., B. Huang , Z-Z. Hu, A. Kumar, C. Wen. D. Behringer, and S. Nadiga, 2010: An assessment of oceanic variability in the NCEP climate forecast reanalysis. *Clim. Dyn.*, doi: 10.1007/s00382-010-0954-4.

Yu, L., R. A. Weller, and B. Sun, 2004: Improving latent and sensible heat estimates for the Atlantic Ocean (1988-99) by a synthesis approach. *J. Climate*, **17**, 373-393.

Yu, L., X. Jin, and R. A. Weller, 2006: Role of net surface heat flux in seasonal variations of sea surface temperature in the tropical Atlantic Ocean. *J. Climate,* **19**, 6153-6169.

Yu, L., X. Jin, and R. A. Weller, 2008: Multidecade Global Flux Datasets from the Objectively Analyzed Air-sea Fluxes (OAFlux) Project: Latent and Sensible Heat Fluxes, Ocean Evaporation, and Related Surface Meteorological Variables. *OAFlux Project Technical Report (OA-2008-01)*, Woods Hole Oceanographic Institution, Woods Hole, MA.

Yu, L., 2011: A global relationship between the ocean water cycle and near-surface salinity. *J. Geophys. Res. Oceans*, accepted.

Zeng, X., M. Zhao, and R. E. Dickinson, 1998: Intercomparison of bulk aerodynamic algorithms for the computation of sea surface fluxes using TOGA COARE and TAO data. *J. Climate*, **11**, 2628-2644.

Zhang, F. W., W. M. Drennan, B. K. Haus, and H. C. Graber, 2009: On wind-wave-current interactions during the Shoaling Waves Experiment. *J. Geophys. Res.,* **114***, C01018, doi: 10.1029/2008JC004998.

Zhang, R.-H., L. M. Rothstein, and A. J. Busalacchi, 1999: Interannual and decadal variability of the subsurface thermal structure in the Pacific Ocean: 1961–90. *Climate Dyn.*, **15,** 703–717.

Zhang, T. Y., J. M. Wallace, and D. S. Battisti, 1997: ENSO-like interdecadal variability: 1900–93. *J. Climate*, **10,** 1004–1020.